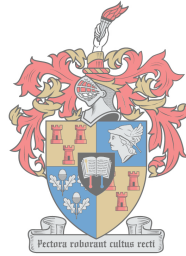# Design of a Wideband Sinuous Antenna for Radio Telescope Applications

by

Nicol Steenkamp

Thesis presented in partial fulfilment of the requirements for the degree of Master of Engineering (Electrical and Electronic) in the Faculty of Engineering at Stellenbosch University

Supervisor: Prof. D.I.L. De Villiers

March 2018

Declaration

By submitting this thesis electronically, I declare that the entirety of the work contained therein is my own, original work, that I am the sole author thereof (save to the extent explicitly otherwise stated), that reproduction and publication thereof by Stellenbosch University will not infringe any third party rights and that I have not previously in its entirety or in part submitted it for obtaining any qualification.

Date: ....March 2018.................

Abstract

Design of a Wideband Sinuous Antenna for Radio Telescope Applications

N. Steenkamp

Department of Electrical and Electronic Engineering,
University of Stellenbosch,
Private Bag X1, Matieland 7602, South Africa.

Thesis: MEng (EE)

December 2017

This thesis investigates a pyramidal sinuous antenna. It was suggested in a previous study that the pyramidal shape would be easier to manufacture than a conical shape. To test this, a model was simulated and manufactured to operate over $2 - 6$ GHz. It proved to be more robust with a differential reflection coefficient around -10 dB compared to its conical counterpart which is around -5 dB.

The wideband capabilities were also investigated. A new modelling approach was required for the wide bandwidth. Though a 10:1 version was simulated, the manufactured model only performed decently over a 5:1 bandwidth.

A parameter study was also conducted on the antenna to estimate its performance in Band 1 of the Square Kilometre Array. The best performance results were determined with the best mean sensitivity possible, while maintaining a differential reflection coefficient less than -10 dB, being 4.6 m^2/K.

Uittreksel

Ontwerp van 'n Wyeband Siniese Antenna vir Radioteleskoop Toepassings

("Design of a Wideband Sinuous Antenna for Radio Telescope Applications")

N. Steenkamp

Departement Elektriese en Elektroniese Ingenieurswese,
Universiteit van Stellenbosch,
Privaatsak X1, Matieland 7602, Suid Afrika.

Tesis: MIng (EE)

Desember 2017

Hierdie tesis ondersoek 'n piramiediese siniese antenna. Dit was voorgestel in 'n vorige studie dat 'n piramiediese vorm makliker sou wees om te vervaardig as 'n koniese vorm. 'n Model was gesimuleer en vervaardig om oor $2-6$ GHz te werk om hierdie te toets. Dit is bewys as meer robuust met 'n differensiele weerkaatskoeffisient rondom -10 dB in vergelyking met sy koniese ewęknie wat rondom -5 dB is.

Die wyeband vermoens was ook ondersoek. 'n Nuwe benadering tot modellering was nodig vir die wye bandwydte. Alhoewel 'n 10:1 weergawe gesimuleerd is, het die vervaardige model slegs billik oor 'n 5:1 bandwydte gewerk.

'n Parametriese studie was ook gedoen op die antenna om sy vermoens in Band 1 van die Square Kilomtre Array te bepaal. The beste resultate was bepaal met die beste gemiddelde sensitiwiteit moontlik, terwyl 'n differensiele weerkaatskoeffisient minder as -10 dB gehandhaaf word, as 4.6 m^2/K ontdek is.

Acknowledgements

I would like to express my sincere gratitude to the following people and organisations ...

First and foremost, I want to truly thank my supervisor Prof. Dirk de Villiers whose patience, support and motivation cannot be understated.

Next, I would like to acknowledge and apologise to my parents who had to stress too much at the end.

There are various people to thank who assisted me with important tasks. Thank you to Mr. Wessel Croukamp and Mr. Wynand van Eeden who helped to manufacture the antennas, Anneke Bester who assisted in their measurements, and to Dr. Danie Ludick who showed me how to use the High Performance Cluster.

Thank you to all the people in E205 who made the office life more entertaining.

Lastly, thank you to the National Research Foundation of South Africa and Prof David Davidson who were responsible for funding this thesis.

Contents

List of Figures

List of Tables

Chapter 1

Introduction

1.1   About the Square Kilometre Array

The Square Kilometre Array (SKA) is a massive scientific and engineering project. It aims to be the world's largest radio interferometer. When completed, it will see farther and clearer into the universe than ever before and, hopefully, shed light on its biggest mysteries. While its purpose is for scientific research, the SKA's design creates opportunities for engineering research.

A diverse assortment of topics are being investigated. These include the antennas, electromagnetic interference detection, and data manipulation to name but a few examples. To understand this thesis' contribution to the grand project, it is convenient to first provide an overview of the SKA.

The construction of the SKA is divided into phases. A baseline design of the first phase is available online [1], detailing its desired performance and configuration. In Fig. 1.1 a schematic diagram of the first phase is shown. It can be seen that the project is divided geographically between Australia and South Africa with the former housing the low frequency range site (SKA1-low) and the latter housing the mid frequency range site (SKA1-mid). SKA1-mid is planned to expand upon the precursor project MeerKAT [2]. Eventually the site will contain 64 MeerKAT dishes, each with 13.5 m equivalent diameters, and 133 SKA1-mid dishes, each with 15 m equivalent diameters, in offset Gregorian configurations.

These dishes will operate in the $0.35 - 13.8$ GHz frequency range with possible future endeavours up to 24 GHz. In order to cover the entire bandwidth, the proposed strategy is to split it up into 5 different bands with each band having its own feed antenna. When required, the relevant antenna receiver can be mechanically moved to a dish's focal point. The currently planned frequency bands for SKA1-mid are the ones listed in Table 1.1. Their lowest and highest bands have 3:1 bandwidths and those in between have 1.85:1 bandwidths.

To cover the narrower bands, it has been decided to use corrugated horn antennas. To cover the wider bands, a wideband antenna is required. The relevant wideband antenna has yet to be finalised since there are various candidates being developed. Research is also being conducted in tandem to this to find an ultra wideband dish feed. Such a feed could potentially cover multiple frequency bands which would severely reduce the number of required feeds for the entire SKA1-mid site. This would lead to significant cost savings as well as a simpler mechanical setup for the dishes. In addition, it would allow for a more continuous coverage over the frequency range.
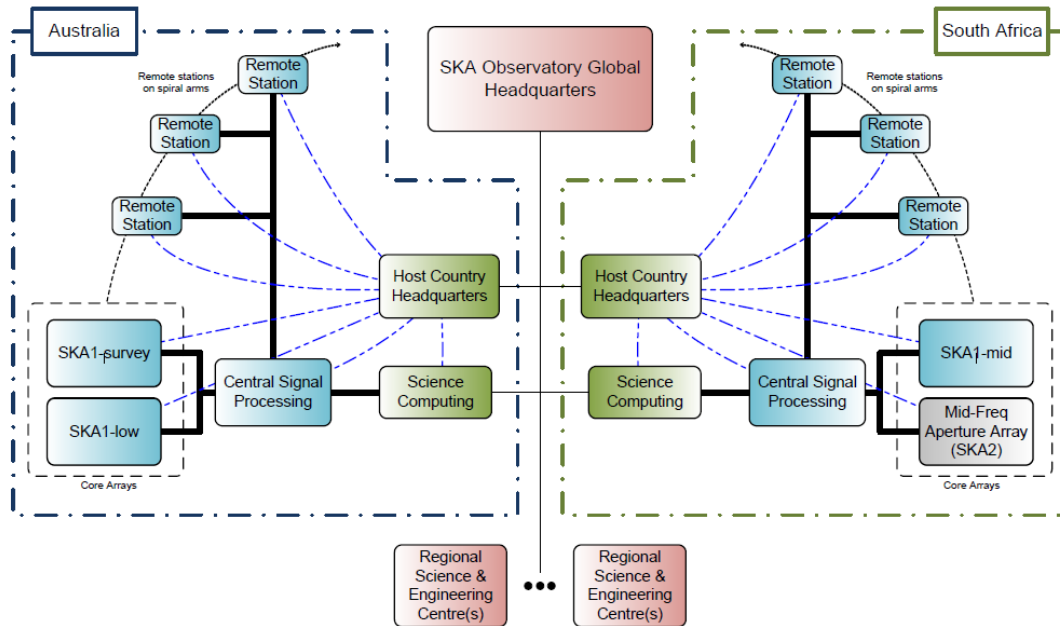
Figure 1.1: Diagram of the SKA's first phase [1]

Table 1.1: Frequency bands of SKA1-mid

Band	Frequency range (MHz)
1	$350 - 1050$
2	$950 - 1760$
3	$1650 - 3050$
4	$2800 - 5180$
5	$4600 - 13800$

The wideband antennas being investigated include the quasi self-complimentary feed (QSC) [3], the log periodic dipole array feed [4], the quad-ridge flared horn antenna [5], the eleven feed [6] and the conical sinuous antenna [7]. They are shown in Fig. 1.2. It is interesting to observe that attributes common (but not universal) between them include the use of log periodic structures for wideband performance, and ground planes for unidirectional radiation. As research continues on these candidates, their performances keep on improving.

This thesis also contributes to the research on wideband antennas for SKA1-mid. It is about a modified conical sinuous antenna aptly referred to as a pyramidal sinuous antenna.

1.2   About the Pyramidal Sinuous Antenna

In [10] various versions of a conical sinuous antenna were successfully fabricated and then characterized over a $0.3 - 4$ GHz frequency range. As part of a larger study, a $3 : 1$ bandwidth version was also designed and manufactured in [11]. However, in that thesis the manufactured antenna performed notably worse than its predicted simulations. Etching on and assembling the curved petals of the conical sinuous antenna proved to be a challenge. This caused crucial physical differences between the desired simulation

(a) QSC feed [8]   (b) Log periodic dipole array   (c) Quad-ridge flared horn an-
                          feed [4]   tenna [5]

(d) Eleven feed [9]   (e) Conical sinuous antenna [10]
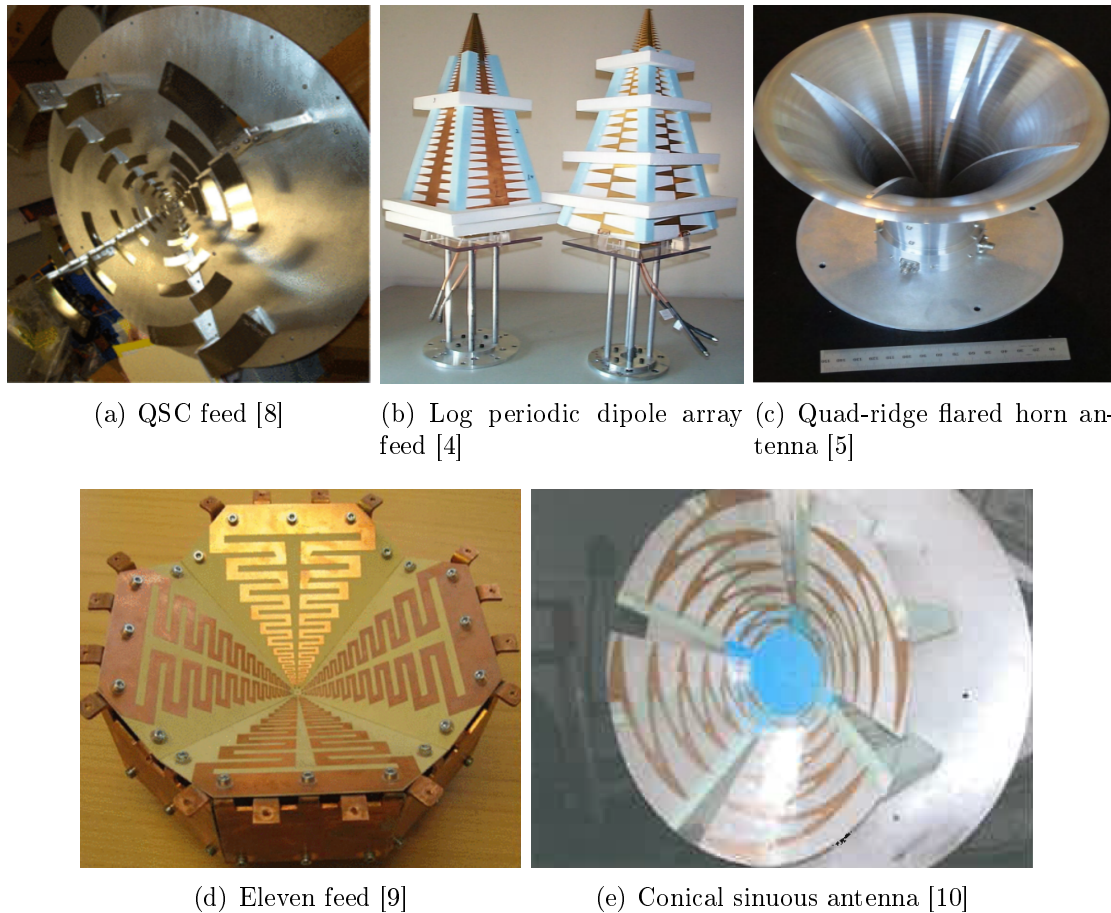
Figure 1.2: Vaious reflector feeds being researched for the SKA

model and the realised manufactured model. These differences were the reason for the discrepancy in performance.

As a continuation of the work done in [11], the idea of a pyramidal sinuous antenna was formed. Like its name states, it uses a pyramidal instead of a conical shape for the antenna petals. In theory, this should allow for a much simpler construction process which avoids the pitfalls encountered in the previous study. In practice, this still had to be confirmed.

Since it is a novel antenna, there are various aspects about it worth researching. In this thesis the main topics of interest include the pyramidal sinuous antenna's feasibility, its ultra wideband capabilities, and its performance as a reflector feed. Regarding its feasibility, it is prudent to establish whether a model could be easily manufactured that would perform as its simulation predicted. This would warrant its existence as a potential alternative to the conical sinuous antenna. As was mentioned, an ultra wideband antenna could be hugely beneficial for SKA1-mid. Therefore, the pyramidal sinuous antenna's performance over a large frequency spectrum was also explored. In all cases, the antenna is intended to serve as a feed for a reflector. However, its potential performance as a feed for a SKA dish over one of the frequency bands is the eventual goal. Consequently, this was also investigated.

1.3   About this thesis

The work contained in this document is intended to stand on its own. It covers the theory surrounding the pyramidal sinuous antenna, the methods used to research it, and the results that were obtained. As a preview for the rest of this thesis, an overview of each chapter is given below.

Chapter 2: An overview of parabolic reflectors and dual reflectors are presented. It is useful to understand them when investigating a reflector feed. An important figure of merit, the aperture efficiency, is also explained. This performance metric is used throughout the thesis when comparing results.

Chapter 3: The planar sinuous antenna as well as the conical sinuous antenna are introduced. Since the pyramidal sinuous antenna is based on them, knowledge regarding these antennas is required. Due to how the antenna is fed in the following chapters, a section about mixed mode S-parameters is also included.

Chapter 4: In this chapter the simulation, construction and measurements of a $2-6$ GHz pyramidal sinuous antenna is given. The challenges and methods involved for each stage are described and the final results are examined and compared.

Chapter 5: Continuing from the previous chapter, the simulation, construction and measurements of an attempted $10:1$ bandwidth pyramidal sinuous antenna is presented. New challenges, and how they were addressed, are the focus here.

Chapter 6: In order to determine the pyramidal sinuous antenna's performance as a feed for an SKA dish, a straightforward parameter study was conducted on it. The best possible results in terms of differential reflection coefficients and sensitivity are given. Preceding this, a short explanation about sensitivity is also provided.

Chapter 2

Overview of Reflector Antennas

Reflector antennas, as their name suggests, radiate by scattering incoming waves in a desired direction. They have existed, in some form or another, since the discovery of electromagnetic radiation in 1888. It was, however, during the Second World War that their designs and analysis techniques truly leapt forward. In the 1960s, reflector antennas were extensively used for space communication applications. Today, they are an integral part to modern society.

Certain types of reflector antennas are capable of achieving high gains and low noise. Consequently they are a favoured option for radio astronomy purposes. This includes, among others, the SKA project. Since the pyramidal sinuous antenna is intended to serve as a reflector feed, it is therefore beneficial to understand how these antennas function.

This chapter aims to impart that understanding. It will essentially involve a qualitative summary of reflector antennas as explained in [12]. Predominantly, parabolic reflector antennas and dual reflector antennas will be presented. Knowledge about the former is useful when analysing the latter. Plane and corner reflector antennas, however, will be introduced first as stepping stones to the more complex varieties. How these antennas are physically structured, how they operate and how they are analysed will be discussed.

A key performance metric of reflector antennas is the so-called aperture efficiency. It is used extensively in later chapters when comparing the results of pyramidal sinuous antennas. What it is and how to calculate it will be described in thorough detail. Aperture efficiency also plays an important part when calculating the sensitivity of a SKA dish, but more will explained later.

2.1   Plane Reflector Antenna

The simplest type of reflector antenna consists of an antenna – referred to as the feed – in front of a perfect conducting plane. Radiated energy is directed in the desired direction with help from the plane. The feed's polarization and its position relative to the plane control the overall system's radiation properties. If the feed is a horizontal or vertical linear element, then the overall system's radiation properties can easily be analysed using Image Theory as shown in Fig. 2.1. If the plane is electrically large relative to the feed, it can be idealized as an infinite plane. If not, special techniques such as the Geometrical Theory of Diffraction can be used to accurately analyse it.
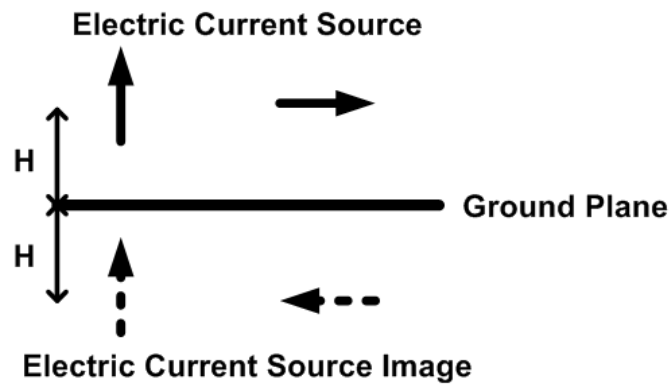
Figure 2.1: Image Theory applied on plane reflecting antenna

2.2 Corner Reflector Antenna

When two plane reflector antennas are joined, they form a corner reflector antenna. The two planes help diminish radiation in the back and side directions and better direct energy in the forward direction. Instead of using a metal sheet as a plane, sometimes a grid of wires can serve as a cheaper and lighter alternative.

Generally, a dipole or an array of collinear dipoles that are placed parallel to the vertex is used as the feed. This configuration can also easily be analysed using Image Theory, as shown in Fig. 2.2. The number of images and their positions are controlled by the angle of the corner reflector antenna and the feed, whereas their polarities are controlled by the feed's polarity.
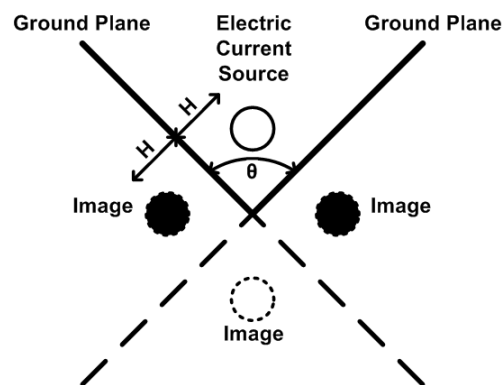
Figure 2.2: Image Theory applied on corner plane reflecting antennas

2.3 Parabolic Reflector Antenna

The simple change from a plane to a corner reflecting surface modified the radiation characteristics. Further improvements can be obtained if the reflector plane uses an enhanced structure. Parabolic reflector antennas*, as indicated by their name, use parabolic shapes to achieve this. When efficiently fed from their focus point and carefully designed, they are capable of achieving a high-gain pencil beam radiation pattern with low side lobes

---

*Parabolic reflector antennas can take two different forms. One uses a parabolic cylinder for the reflector shape while the other uses a paraboloid. This section is applicable to the latter.

and good cross-polarization discrimination. Additionally, they are considered to provide a good compromise between cost and performance, which makes them a popular choice for radio astronomy applications.

2.3.1 Operation

The reflector surface of parabolic antennas allows an incoming plane wave to be redirected towards a point in space. Geometrical optics has shown this to be the case due to the nature of parabolas: when a bundle of rays, starting on a plane normal to a parabola's symmetry axis, is directed parallel to the parabola's symmetry axis towards the parabola, the application of Snell's law locally on the parabolic surface reflects all the rays to the parabola's focus. Figure 2.3 illustrates this well. Essentially all incoming parallel rays converge to a spot after travelling the same distance. The feed is placed at this spot.

A parabolic reflector antenna's performance is largely dependent on its feed's radiation pattern and the focal length to diameter (F/D) ratio. Historically, horn or waveguide antennas were used as feeds. However, increasingly demanding requirements for radio astronomy and space communication applications have led research for new, more efficient feeds.
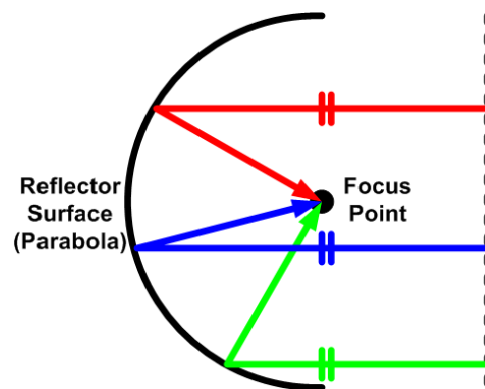
Figure 2.3: A parabolic shape focuses incoming parallel rays

2.3.2 Geometry

The physical structure consists of a feed as well as an electrically large paraboloid – a parabola rotated around its symmetry axis – used as the reflector as shown in Fig. 2.4. For the Cartesian coordinate system as used in the figure, the paraboloid's shape is described by [12]

$$z = F - \frac{x^2 + y^2}{4F} \qquad \text{with } x^2 + y^2 \leq \left(\frac{D}{2}\right)^2 \qquad (2.1)$$

where F is the focal length of the paraboloid and D is its equivalent aperture's diameter. These two parameters are often related to one another in a more familiar form as

$$\frac{F}{D} = \frac{1}{4}\cot\left(\frac{\theta_0}{2}\right) \qquad (2.2)$$

where θ_0, also shown in Fig. 2.4, is called the subtended half angle of the dish. The role of the F/D ratio in a reflector antenna's performance will be discussed in more detail when aperture efficiency is presented.
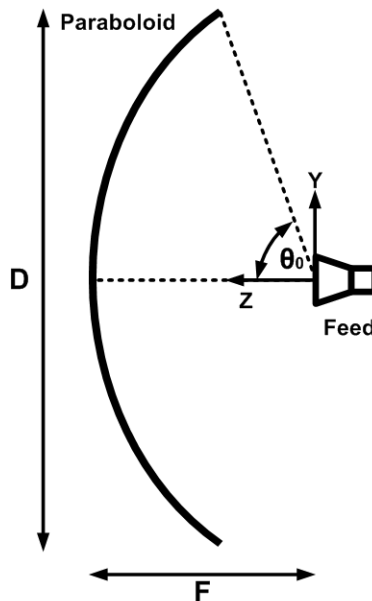
Figure 2.4: A prime focused reflector antenna side view

2.3.3   Analysis

To analyse a parabolic reflector antenna's performance, generally either the aperture distribution method or the current distribution method is used. Both deliver accurate results in the main beam and nearby side lobes. The former method, however, can be performed with equal ease regardless of the feed pattern or feed placement while the latter becomes complex and time consuming when asymmetry in the feed pattern or feed placement occurs. Both use the following approximations:

1. There is no current density on the shadow side of the reflector.

2. The discontinuity of the current density on the rim of the reflector (where the illuminated and shadow side of the reflector connect) is ignored.

3. Direct radiation from the feed and aperture blockage caused by the feed are neglected.

To obtain more accurate results, especially for the far minor lobes, geometrical diffraction or full wave techniques can be applied.

For the aperture method, a few steps have to be performed. First, the fields reflected by the paraboloid have to be determined over the so-called aperture plane. This is simply a plane normal to the paraboloid's symmetry axis that usually (but not always) passes through the focus point. Often geometrical optic techniques, such as ray tracing, are used to accomplish this. Then, equivalent sources are formed over this plane with equivalent sources outside the plane assumed to be zero. Lastly, the radiated fields are calculated using the equivalent sources.

For the current distribution method there are fewer steps. First, induced currents on the reflector surface have to be determined. This can be accomplished using a Physical Optics approximation. Assuming the reflector is large compared to a wavelength and the incident wave is relatively flat, then, locally, a parabolic surface resembles a plane reflector. Thus image theory can be used to calculate the surface current as given by

$$\hat{\boldsymbol{J}}_s = \hat{\boldsymbol{H}}^i + \hat{\boldsymbol{H}}^r = 2\hat{\boldsymbol{n}} \times \hat{\boldsymbol{H}}^i = 2\hat{\boldsymbol{n}} \times \hat{\boldsymbol{H}}^r \tag{2.3}$$

where $\hat{\boldsymbol{J}}_{\boldsymbol{s}}$ is the surface current, $\hat{\boldsymbol{H}}^{\boldsymbol{i}}$ is the incident magnetic field, $\hat{\boldsymbol{H}}^{\boldsymbol{r}}$ is the reflected magnetic field and $\hat{\boldsymbol{n}}$ is a unit vector normal to the reflector surface. The surface current is then integrated over the reflector surface to determine the far field radiation.

For both methods, the far-field of the entire reflector system is the superposition of the far-field of the feed and the far-field of the reflector. The former, though, often has minimal effect in the bore-sight direction.

2.3.4   Miscellaneous

Other aspects to take into account when designing parabolic reflectors revolves around the feasibility of the feed placement. It requires struts to hold it in place which, alongside the feed, cause additional aperture blockage that lowers performance. Additionally, the receiver electronics also pose a dilemma. If placed on the feed itself, it can cause a very bulky and unwieldy mechanical design, whereas if placed away from the feed long transmission lines are required. These are detrimental to low noise applications such as radio astronomy.

One method to address these challenges is to place the feed off axis. This is referred to as an offset reflector antenna. It is more complex to analyse than a prime fed reflector antenna and can potentially introduce cross-polarization problems. If, however, it is properly designed better performance can be gained since aperture blockage is reduced. Another method is to use a secondary reflector.

2.4   Dual Reflector Antenna

Dual reflector antennas have several trade-offs when compared to prime fed parabolic antennas. For added cost and complexity, convenient feed placement and design flexibility are obtained. They are also capable of achieving larger equivalent F/D ratios than their single reflector counterparts. This allows them to use feeds with a higher gain which often have larger apertures and wider bandwidths.

Depending on the shapes of the main reflector as well as the sub-reflector dish, there exist multiple configurations of dual reflector antennas. Presented here is the classical Gregorian form with an intermittent mention to the classical Cassegrain form [13]. The two have much in common, though they also exhibit crucial differences. The major difference is that the former has an ellipsoid sub-reflector while the latter has a hyperboloid sub-reflector.

2.4.1   Operation

Similar to parabolic reflector antennas, dual reflector antennas allow an incoming plane wave to converge to a single spot due to the shapes of the reflectors. From a geometrical optics perspective, all parallel incoming rays are reflected off the main reflector, travel to the sub-reflector, bounce off the sub-reflector, and converge at the feed after travelling the same distance. This is illustrated in Fig. 2.5.

As shown in the figure, the reflector system has two focal points through which all the rays pass. The feed is placed at one of them, referred to as the secondary focus point of the reflector system, while the main reflector's focus point is located at the other one, called the primary focus point of the reflector system. In a classical Gregorian configuration, the primary focus point sits between the two reflectors while in a classical Cassegrain
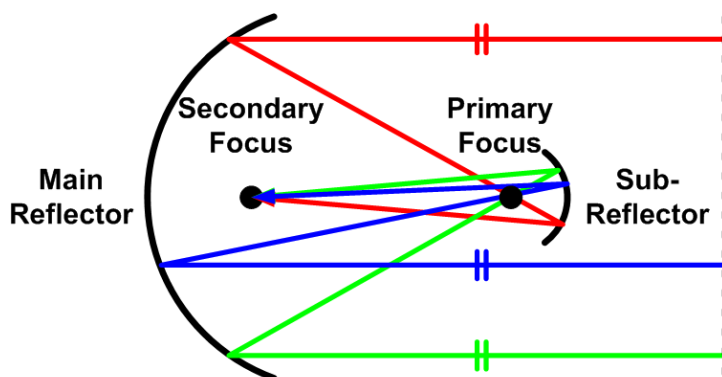
Figure 2.5: The main reflector and the sub-reflector focus incoming parallel rays.

configuration the sub-reflector is in the middle. This allows Cassegrain reflector antennas to have a compact design which is mechanically easier to implement than Gregorian reflector antennas. Gregorian reflector antennas, however, are the more practical choice when using feeds with a higher gain which, as was stated, tend to have wider bandwidths.

2.4.2 Geometry

Dual reflector antennas consist of a feed, an electrically large parabolic main reflector and a smaller ellipsoid / hyperboloid sub-reflector. There exists 21 parameters to fully describe any dual reflector's geometry that fulfils the Mizugutch [14] conditions for zero cross-polarized radiation. This includes offset dual reflectors. Only five, though, are required to be specified and the rest can be calculated as guided by [15]. The parameters define the dishes' shapes and their positions relative to each other and the feed.

A simple dual reflector is shown in Fig. 2.6 with variables from [13]. Using the relevant Cartesian coordinate system, the main reflector's paraboloid shape (previously mentioned in (2.1), but repeated here for convenience) is given by

$$z = \frac{x^2 + y^2}{4F_m} - F_m \qquad \text{with } x^2 + y^2 \leq \left(\frac{D_m}{2}\right)^2 \tag{2.4}$$

where F_m is the main reflector's focal length and D_m its aperture diameter.

The sub-reflector's shape can then be determined according to

$$z = a\sqrt{1 + \frac{x^2 + y^2}{f^2 - a^2}} - f \tag{2.5}$$

where the variables a and f are sub-reflector surface parameters. The variable f is half the distance between the sub-reflector's two foci and the variable a is related to the sub-reflector's eccentricity e by

$$a = \frac{f}{e}. \tag{2.6}$$

Depending on their values, (2.5) can either describe hyperboloids or ellipsoids as shown in Fig. 2.7.

The remaining parameters shown in Fig. 2.6 relate the dishes' focal locations and the feed's position with one another. Variables θ_P and θ_S are the subtended half angles for the primary and secondary focus points, respectively, while L is the distance from
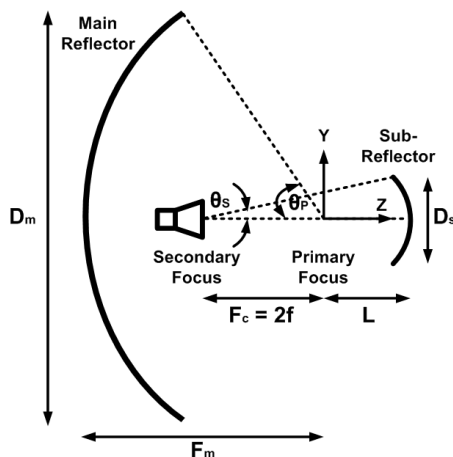
Figure 2.6: Parameters for a dual reflector antenna

the primary focus point to the sub-reflector's vertex. They can be determined by solving (2.7) − (2.9).

$$\frac{F_m}{D_m} = \pm\frac{1}{4}\cot\left(\frac{\theta_P}{2}\right) \tag{2.7}$$

$$\frac{1}{\tan(\theta_P)} + \frac{1}{\tan(\theta_S)} = 2\frac{F_c}{D_s} \tag{2.8}$$

$$1 - \frac{\sin\frac{1}{2}(\theta_P - \theta_S)}{\sin\frac{1}{2}(\theta_P + \theta_S)} = 2\frac{L}{F_c} \tag{2.9}$$

Equation (2.7) is the same as (2.2) with the addition of a plus / minus sign. The positive sign applies to Cassegrain forms and the negative sign to Gregorian forms.

2.4.3 Analysis

To understand and predict the essential performance of dual reflector antennas, the concept of the virtual feed is useful [13]. This method replaces both the real feed and the sub-reflector with a virtual feed as shown in Fig. 2.8 for a Cassegrain form. Thus the dual reflector is simplified to an equivalent parabolic reflector that can be analysed as previously discussed. The virtual feed is located at the reflector system's primary focus. Its effective aperture can be obtained by finding the optical image of the real feed's effective aperture in the sub-reflector. Although the virtual feed provides a useful qualitative understanding for analysing dual reflector antennas, it is an inconvenient method to obtain accurate quantitative predictions.

Another concept that overcomes this shortcoming is the equivalent paraboloid [13]. In this case both the main dish and the sub-reflector are instead replaced by an equivalent parabolic surface as shown in Fig. 2.9 for a Cassegrain form. Once again the dual reflector antenna is simplified to a parabolic reflector (pointing in the opposite direction) that can be analysed as previously discussed. This equivalent paraboloid is determined using geometrical optics ray tracing and does not take into account possible diffraction caused by the sub-reflector.

The equivalent paraboloid's F/D ratio is given in (2.10). It shares the same aperture diameter as the main dish, D_m, but has a greater focal length, F_e. This is the reason why

(a) Hyperboloid geometry

(b) Ellipsoid geometry
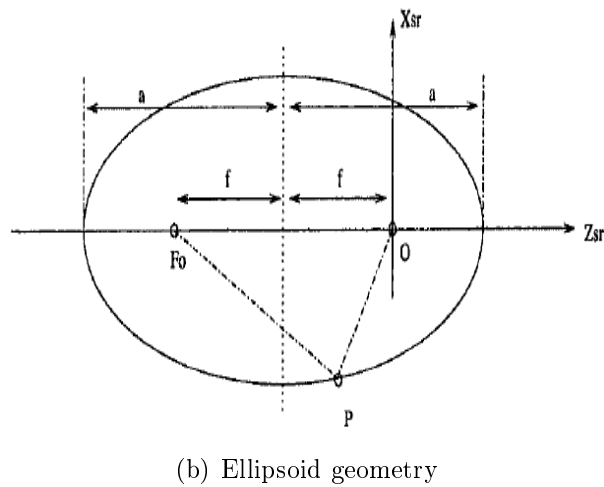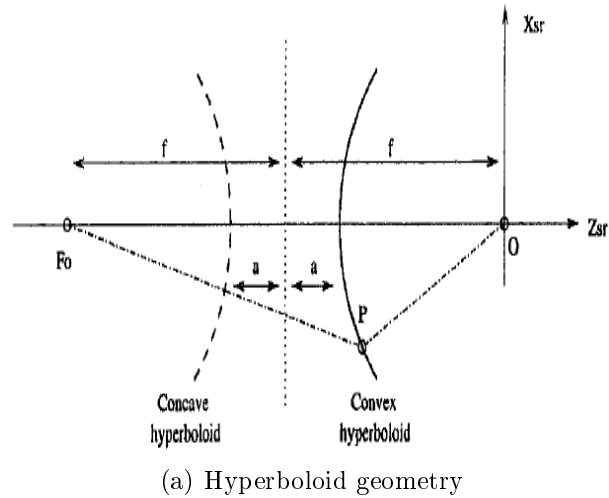
Figure 2.7: Sub-reflector geometry from [15]

dual reflectors are capable of achieving a higher equivalent F/D ratio than their single reflector counterparts.

$$\frac{F_e}{D_m} = \frac{1}{4}\cot\left(\frac{\theta_S}{2}\right) \tag{2.10}$$

The ratio of the main dish and the equivalent dish's focal lengths are given in (2.11). The positive sign applies to the Cassegrain form while the negative sign applies to the Gregorian form.

$$\pm\frac{F_e}{F_m} = \frac{\tan\left(\frac{1}{2}\theta_P\right)}{\tan\left(\frac{1}{2}\theta_S\right)} = \frac{L_r}{L} \tag{2.11}$$

Both analysis methods mentioned can provide good results. For a more accurate analysis of dual reflectors, though, diffraction techniques have to be applied.

2.4.4 Miscellaneous

As in the case of parabolic reflector antennas, the sub-reflector of dual reflector antennas can be offset. These offset dual reflector antennas have to be carefully designed, but they

Figure 2.8: The virtual feed concept [13]

Figure 2.9: The equivalent parabola concept [13]

can potentially deliver better performance since they experience less aperture blockage. To analyse them, the concept of the equivalent paraboloid can be applied as explained in [16]. Thus in the forthcoming analyses of the feed's performance, it is only necessary to consider equivalent symmetrical parabolic reflectors instead of dual reflectors.

Shaping is another technique applicable to reflector antennas. By suitably modifying the default reflector surfaces, it is possible to obtain desired amplitude and phase distributions over one or both reflectors. Essentially, shaping allows for further design flexibility where trade-offs in performance metrics can be expected. Changing the shape of the reflectors through a mapping function as done in [17], for example, allows the receiving sensitivity to be improved at the cost of increased near-in sidelobe levels.

The SKA uses shaped clear aperture offset Gregorian dishes. Compared to Cassegrain reflector antennas, larger feeds are typically used for Gregorian reflector antennas. This is beneficial when operating at high frequencies where small feed dimensions can become impractical. The shaping and offsetting of the dishes help improve the overall performance.

2.4.5 Aperture Efficiency

When describing a reflector antenna's performance, aperture efficiency is a widely used metric. Generally, efficiency is defined as the ratio of output power to input power of a system. Similarly, aperture efficiency is the ratio of the effective aperture area to the physical aperture area of a reflector antenna as given by

$$A_e = \eta_{ap} A_{ph}. \tag{2.12}$$

It is comprised of various losses that, when combined, determine how well the antenna is utilising its physical area. The various losses are considered factors, or subefficiencies, of the total aperture efficiency [18] as given by

$$\eta_{ap} = \eta_{BOR1} \eta_{sp} \eta_{pol} \eta_{ill} \eta_{ph} \eta_{d}. \tag{2.13}$$

The subefficiencies are

- η_{BOR1} the BOR1 (Body-Of-Revolution type 1) efficiency

- η_{sp} the spillover efficiency

- η_{pol} the polarization efficiency

- η_{ill} the illumination efficiency

- η_{ph} the phase efficiency

- η_{d} the diffraction efficiency caused by the sub-reflector in a dual reflector antenna.

There exists additional losses, such as aperture blockage caused by the feed or the struts, but they can easily be taken into account if needed and will be ignored for an offset reflector system.

The subefficiencies are calculated individually. This allows the major contributors of the performance loss to be easily identified. Note in the following descriptions, the subefficiencies are functions of both the subtended half angle, or F/D ratio, of a parabolic reflector antenna as well as the radiation pattern of the feed. For dual reflector antennas, its equivalent parabolic reflector's F/D ratio is used instead. To start the calculations, first consider the radiated far field of any feed. It is given by [19]

$$\hat{\boldsymbol{E}}(r, \theta, \phi) = \frac{1}{r} e^{-jkr} \hat{\boldsymbol{G}}(\theta, \phi) \tag{2.14}$$

where r is the distance from the phase reference point to the observation point, $1/r$ is the divergence factor, e^{-jkr} is the phase factor and $\hat{\boldsymbol{G}}(\theta, \phi)$ is the radiation field function. The field function consists of a θ and a ϕ component as shown by

$$\hat{\boldsymbol{G}}(\theta, \phi) = G_\theta(\theta, \phi)\hat{\boldsymbol{\theta}} + G_\phi(\theta, \phi)\hat{\boldsymbol{\phi}} \tag{2.15}$$

with $\hat{\boldsymbol{\theta}}$ and $\hat{\boldsymbol{\phi}}$ the unit vectors in the directions of increasing polar angle, θ, and azimuth angle, ϕ, respectively.

Since it is periodic in the ϕ-direction – with a period of 2π – (2.15) can be expanded into a Fourier series as given by

$$\hat{\boldsymbol{G}}(\theta, \phi) = \sum_{n=0}^{\infty} \left[A_n(\theta) \sin(n\phi) + B_n(\theta) \cos(n\phi) \right] \hat{\boldsymbol{\theta}} + \sum_{n=0}^{\infty} \left[C_n(\theta) \cos(n\phi) - D_n(\theta) \sin(n\phi) \right] \hat{\boldsymbol{\phi}}$$

$$\tag{2.16}$$

with

$$G_\theta(\theta, \phi) = \sum_{n=0}^{\infty} [A_n(\theta) \sin(n\phi) + B_n(\theta) \cos(n\phi)]$$

$$G_\phi(\theta, \phi) = \sum_{n=0}^{\infty} [C_n(\theta) \cos(n\phi) - D_n(\theta) \sin(n\phi)]$$

(2.17)

where the minus sign in front of $D_n(\theta)$ is due to symmetry reasons. The advantage of the Fourier series formulation is that the far field can be analytically expanded to all ϕ-angles if it is only known in a few ϕ-planes [20].

Incidentally, in measurements and simulations the far field is only known in a finite number of ϕ-planes. For N ϕ-planes the known far field pattern components are

$$G_\theta(\theta, k \cdot \Delta\phi) \text{ and } G_\phi(\theta, k \cdot \Delta\phi) \text{ for } k = 0, 1, 2, \ldots, N-1 \qquad (2.18)$$

with $\Delta\phi = 2\pi/N$ the interval between the ϕ-planes.

The Fourier coefficients can then be determined through an inverse discrete Fourier transform [21] as given by

$$A_n(\theta) = \frac{2}{N} \sum_{k=0}^{N-1} G_\theta(\theta, k\Delta\phi) \sin(kn\Delta\phi)$$

$$B_n(\theta) = \frac{2}{N} \sum_{k=0}^{N-1} G_\theta(\theta, k\Delta\phi) \cos(kn\Delta\phi)$$

$$C_n(\theta) = \frac{2}{N} \sum_{k=0}^{N-1} G_\phi(\theta, k\Delta\phi) \cos(kn\Delta\phi)$$

$$D_n(\theta) = \frac{2}{N} \sum_{k=0}^{N-1} G_\phi(\theta, k\Delta\phi) \sin(kn\Delta\phi)$$

(2.19)

where $n = 0, 1, \ldots, (N-1)/2$ are referred to as the ϕ-modes. The highest ϕ-mode component obtainable in N ϕ-planes, is $(N-1)/2$ due to the periodicity of sinusoidal functions.

Further explanations of the subefficiencies and how they are calculated are provided next.

BOR1 Efficiency

Though the general feed radiation pattern consists of multiple ϕ-mode components, it is only the $n = 1$ ϕ-mode that contributes to the on-axis gain of the feed [18]. All higher order ϕ-modes' contributions to the radiated field pattern cancel each other out on-axis, though not necessarily elsewhere. Therefore, they represent power lost in the side lobes.

The $n = 1$ ϕ-mode components are referred to as the $BOR1$ pattern. They are rotationally symmetric, and when used to excite a rotationally symmetric structure such as a reflector dish, they excite no other orders of ϕ-modes. Thus, only the $BOR1$ pattern of a feed leads to the on-axis gain of an axially symmetric reflector system. This is also a valid assumption when dealing with axially symmetric equivalent reflector systems, given that diffraction and edge effects are ignored. Regarding their name, BOR or Body-Of-Revolution is an established abbreviation used to describe rotationally symmetric objects

while the index "1" alludes to the first order variation of the field pattern in the ϕ-direction.

$BOR1$-efficiency is therefore defined as the ratio of power in the $BOR1$ components of a feed's radiation pattern to the total power of the feed's radiation pattern. It can be thought of as a measure of the rotational symmetry inherent in the radiation pattern and is calculated as

$$
\begin{aligned}
\eta_{BOR1} &= \frac{\int_0^{2\pi}\int_0^{\pi}\left[|G_{\theta 1}|^2+|G_{\phi 1}|^2\right]\sin\theta d\theta d\phi}{\int_0^{2\pi}\int_0^{\pi}\left[|G_{\theta}(\theta,\phi)|^2+|G_{\phi}(\theta,\phi)|^2\right]\sin\theta d\theta d\phi}\\
&= \frac{\int_0^{\pi}\left[|A_1(\theta)|^2+|B_1(\theta)|^2+|C_1(\theta)|^2+|D_1(\theta)|^2\right]\sin\theta d\theta}{\int_0^{2\pi}\int_0^{\pi}\left[|G_{\theta}(\theta,\phi)|^2+|G_{\phi}(\theta,\phi)|^2\right]\sin\theta d\theta d\phi}
\end{aligned}
\tag{2.20}
$$

with

$$
\begin{aligned}
G_{\theta 1} &= A_1(\theta)\sin\phi + B_1(\theta)\cos\phi\\
G_{\phi 1} &= C_1(\theta)\sin\phi - D_1(\theta)\cos\phi
\end{aligned}
\tag{2.21}
$$

and

$$
\int_0^{2\pi}\int_0^{\pi}\left[|G_{\theta 1}|^2+|G_{\phi 1}|^2\right]\sin\theta d\theta d\phi = \int_0^{\pi}\left[|A_1(\theta)|^2+|B_1(\theta)|^2+|C_1(\theta)|^2+|D_1(\theta)|^2\right]\sin\theta d\theta.
\tag{2.22}
$$

Co-polar and Cross Polar Fields

Before calculating the other subefficiencies, it is important to introduce the useful relationship between the fields in the E- and H-plane and the co- and cross-polar fields in the $\phi = 45°$-plane for $BOR1$-antennas. As an illustration, consider a y-polarized infinitesimal electric dipole located on the symmetry axis. It only excites $A_1(\theta)$ and $C_1(\theta)$; an x-polarized dipole would only excite $B_1(\theta)$ and $D_1(\theta)$. $A_1(\theta)$ is its pattern in the E-plane, or $\phi = 90°$-plane in this case, and $C_1(\theta)$ is its pattern in the H-plane, or $\phi = 0°$-plane. Using Ludwig's third definition for polarization [22], with the co-polar and cross-polar unit vectors given by (2.23) and (2.24), respectively, it can be shown [18] that the co-polar field in the $\phi = 45°$-plane is half the sum of E- and H-plane fields while the cross-polar field is half their difference. This is shown in (2.25) and (2.26), respectively.

$$
\hat{a}_{co} = \sin\phi\hat{\boldsymbol{\theta}} + \cos\phi\hat{\boldsymbol{\phi}}
\tag{2.23}
$$

$$
\hat{a}_{xp} = \cos\phi\hat{\boldsymbol{\theta}} - \sin\phi\hat{\boldsymbol{\phi}}
\tag{2.24}
$$

$$
\hat{\boldsymbol{G}}(\theta,\phi)\cdot\hat{a}_{co}|_{\phi=45°} = CO_{45}(\theta) = \frac{1}{2}[A_1(\theta)+C_1(\theta)]
\tag{2.25}
$$

$$
\hat{\boldsymbol{G}}(\theta,\phi)\cdot\hat{a}_{xp}|_{\phi=45°} = XP_{45}(\theta) = \frac{1}{2}[A_1(\theta)-C_1(\theta)]
\tag{2.26}
$$

Using the terms in (2.25) and (2.26), the co- and cross polar fields can be calculated anywhere as given by (2.27) and (2.28).

$$
G_{co}(\theta,\phi) = \hat{G}(\theta,\phi)\cdot\hat{a}_{co} = CO_{45}(\theta) - XP_{45}(\theta)\cos(2\phi)
\tag{2.27}
$$

$$
G_{xp}(\theta,\phi) = \hat{G}(\theta,\phi)\cdot\hat{a}_{xp} = XP_{45}(\theta)\sin(2\phi)
\tag{2.28}
$$

The aperture efficiency and its remaining subefficiencies can also be described in terms of (2.25) and (2.26). The advantage of this approach is that there is no ϕ dependency to take

into account when calculating them. Equation (2.29) gives the full aperture efficiency; the remaining subefficiencies' calculations are shown next.

$$\eta_{ap} = 2\cot^2(\theta_0/2)\frac{\left|\int_0^{\theta_0} CO_{45}(\theta)\tan(\theta/2)d\theta\right|^2}{\int_0^{\pi}\left[|CO_{45}(\theta)|^2 + |XP_{45}(\theta)|^2\right]\sin\theta d\theta} \qquad (2.29)$$

Spillover Efficiency

Spillover efficiency is defined as the fraction of total power radiated by the feed that is intercepted and collimated by the reflecting surface. Stated differently, it is the power radiated by the feed in a parabolic reflector's subtended half angle in relation to its total power.

$$\eta_{sp} = \frac{\int_0^{\theta_0}\left[|CO_{45}(\theta)|^2 + |XP_{45}(\theta)|^2\right]\sin\theta d\theta}{\int_0^{\pi}\left[|CO_{45}(\theta)|^2 + |XP_{45}(\theta)|^2\right]\sin\theta d\theta} \qquad (2.30)$$

Polarization Efficiency

Polarization efficiency calculates the power in the desired polarization relative to the total radiated power, both within the subtended half angle.

$$\eta_{pol} = \frac{\int_0^{\theta_0}|CO_{45}(\theta)|^2\sin\theta d\theta}{\int_0^{\theta_0}\left[|CO_{45}(\theta)|^2 + |XP_{45}(\theta)|^2\right]\sin\theta d\theta} \qquad (2.31)$$

Illumination Efficiency

Illumination efficiency, also known as taper efficiency, represents the uniformity of the amplitude distribution of the feed pattern over the surface of the reflector. It indicates how much of the reflector area is being effectively illuminated.

$$\eta_{ill} = 2\cot^2(\theta_0/2)\frac{\left[\int_0^{\theta_0}|CO_{45}(\theta)|\tan(\theta/2)d\theta\right]^2}{\int_0^{\theta_0}|CO_{45}(\theta)|^2\sin\theta d\theta} \qquad (2.32)$$

There is a natural trade-off between spillover and illumination efficiency as a function of the F/D ratio. Assume there is a reflector system with a feed designed for a specific F/D ratio. If the ratio is changed, a larger ratio would imply that the reflector surface is being more uniformly illuminated, but less of the feed's rays are being reflected. Conversely, a smaller ratio would imply that more of the feed's rays are being reflected, but less of the reflector surface is being uniformly lit.

Phase Efficiency

Phase efficiency is a measure of the phase errors inherent in the co-polar radiation field. It is the only subefficiency that is dependent on the location of the feed relative to the focus of the reflector. In fact, the phase centre of the feed is uniquely defined as the spot that maximises the phase efficiency.

$$\eta_{ph} = \frac{\left|\int_0^{\theta_0} CO_{45}(\theta)\tan(\theta/2)d\theta\right|^2}{\left[\int_0^{\theta_0}|CO_{45}(\theta)|\tan(\theta/2)d\theta\right]^2} \qquad (2.33)$$

Diffraction Efficiency

Diffraction efficiency is a loss caused by diffraction on the rim of a sub-reflector in a dual reflector system. A method to analytically calculate it is presented in [23]. The solution applies to the family of functions of the form

$$G(\theta) = (m+1)\cos^{2m}(\theta/2) \tag{2.34}$$

where the value of m is chosen so that (2.34) best corresponds to a given feed's actual radiation pattern.

When using such a field radiation pattern in a dual reflector system with parameters shown in Fig. 2.10, the diffraction efficiency is given as

$$\eta_d = \left| 1 + \frac{m\sin^2(\theta_0/2)\cos^m(\theta_0/2)(j-1)\Delta\rho}{1 - \cos^m(\theta_0/2)\sqrt{2\pi D}} \right|^2 \tag{2.35}$$

with

$$\Delta\rho = \sqrt{\frac{\lambda(\rho_{m0} + \sigma\rho_{s0})}{\pi} \left| \frac{\rho_{m0}}{\rho_{s0}} \right|} \tag{2.36}$$

where ρ_{m0} and ρ_{s0} are the distances from the virtual focus (the origin in the figure) to the main reflector and sub-reflector, respectively, along the central ray (corresponding to θ_0 in the figure). The value of σ is set to 1 for Gregorian systems and to -1 for Cassegrain systems.
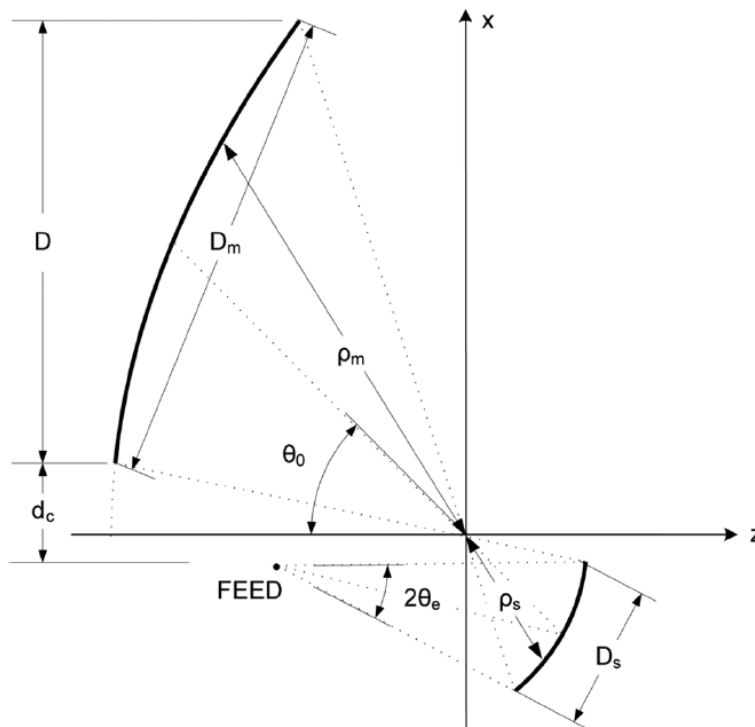
Figure 2.10: Offset dual reflector with parameters used to calculate η_d [23]

This completes the explanation about aperture efficiency calculations. Readily available in-house code was used to determine the subefficiencies, and consequently, also the aperture efficiency.

Chapter 3

Overview of Sinuous Antennas

In the previous chapter it was explained that the performance of a reflector antenna is primarily dependent on its F/D ratio and feed's radiation pattern. While one division of research on the SKA is concerned about improving the reflector dishes, another part is focussed on the reflector feeds. For the SKA dishes, the desired feed should possess a rotationally symmetric radiation pattern (high η_{BOR1}) and provide dual senses of polarization [1]. The wideband antennas being investigated possess these properties and so does the pyramidal sinuous antenna.

It is derived from the conical sinuous antenna, which in turn is based on the original planar sinuous antenna. This chapter focusses on these two antennas. Understanding the planar sinuous antenna's behaviour is necessary to understanding the conical sinuous antenna's behaviour. Due to it being a slight variation, the knowledge also applies to the pyramidal sinuous antenna.

Regarding the chapter's content, the essentials of the planar sinuous antenna will be explained. That includes its geometry, why it radiates, how to excite it and how to feed it. The conical sinuous antenna shares some of these aspects, though obviously deviates from many of them. The aspects relevant to the conical sinuous antenna will be further detailed.

Relating to the performance metrics for antennas in general, the reflection coefficient is an important one. It is a common figure of merit in microwave theory. Due to the feeding scheme used for the sinuous antennas, it is desirable to describe it by the differential reflection coefficient. However, often only the the standard reflection coefficients are available. Therefore, as part of the chapter about the reflector's feed, a method to convert the standard S-parameters to the mixed mode S-parameters will also be explained.

3.1 Planar Sinuous Antenna

First introduced in 1987 [24], DuHamel's sinuous antenna improves on the capabilities of Archimedes and log-spiral antennas. It is easily recognizable due its uniquely curved arms. Their sinuousoidal pattern is log-periodic in nature and allows for the antenna's wideband performance. Unlike its predecessors, the sinuous antenna provides dual orthogonal senses of polarization – either linear or circular. It is also, through an absorbing back-cavity, able to obtain unidirectional radiation. Due to this, the sinuous antenna is a popular choice for direction finding and radar warning receiver applications.

3.1.1 Geometry

In general, the sinuous antenna consists of $N \geq 2$ arms. The default version has 4 arms (2 for single polarization) due to the feeding complexities inherent for any other number. A 4 arm sinuous antenna is shown in Fig. 3.1(c). The antenna arms are placed in such a manner that rotating it by $360/N°$ around the centre point results in the same structure.

Each arm is comprised of Q sinuous cells. A single cell, q, is defined by the two sinuous curves [25]

$$\phi_1(r) = (-1)^q \alpha \sin\left(\frac{\pi \ln(r/R_q)}{\ln \tau}\right) + \delta \qquad \text{for } R_{q+1} \leq r \leq R_q \qquad (3.1a)$$

$$\phi_2(r) = (-1)^q \alpha \sin\left(\frac{\pi \ln(r/R_q)}{\ln \tau}\right) - \delta \qquad \text{for } R_{q+1} \leq r \leq R_q \qquad (3.1b)$$

where ϕ and r are the polar coordinates of any point along the curve. Variable α is termed the angular width and variable δ the rotation angle. A single sinuous curve (containing Q sinuous cells) excluding δ is shown in Fig. 3.1(a). While α determines a sinuous curve's width, δ influences a sinuous arm's thickness as shown in Fig. 3.1(b). The outer radius, R_q, and inner radius, R_{q+1}, of a sinuous cell are related to each other by

$$R_{q+1} = \tau R_q \qquad \text{for } 1 \leq q < Q \qquad (3.2)$$

with $\tau < 1$ called the growth rate. Thus τ determines the spacing between each sinuous cell. Continuously applying equation 3.2 results in the first and last sinuous cells relating to each other according to

$$R_Q = \tau^Q R_1 \qquad (3.3)$$

Though it is possible to define angular growth and growth rate as functions of the q'th sinuous cell, they are generally defined as constant values.

A sinuous arm thus swings between the two angles $\phi = \pm(\alpha + \delta)$ while its radius decreases logarithmically as a function of τ. Figure 3.1 illustrates how a sinuous curve, consisting of sinuous cells, evolves to a sinuous arm, and then to a sinuous antenna. Due to the definition used in (3.1), the sinuous arms are allowed to interleave with each other, but cannot touch. Due to convenience, the start and end radii of a sinuous arm are described as part of the following section.

(a) Sinuous curve   (b) Sinuous arm   (c) Sinuous antenna
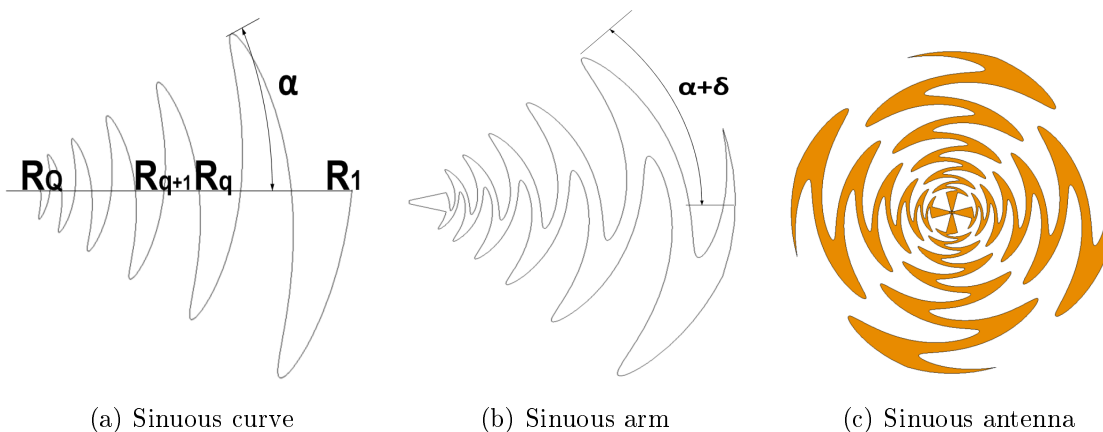
Figure 3.1: Geometry of a sinuous antenna
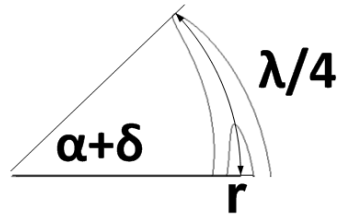
Figure 3.2: Active region of a sinuous arm

3.1.2 Radiation and Excitation

Radiation on a sinuous antenna occurs in areas referred to as active regions. These are zones where the electrical path length to the bend and back of a sinuous cell is approximately an odd multiple of $\lambda/2$ where λ is the wavelength. Using simple trigonometry the first active region, as shown in Fig. 3.2, occurs approximately when

$$r(\alpha + \delta) = \frac{\lambda}{4} \tag{3.4}$$

with the angles in radians. Attenuation after the first active region is large which diminishes radiation from higher order active regions.

Using equation (3.4), the start radius and end radius of a sinuous arm can be determined. Since a practical sinuous antenna only radiates over a finite bandwidth, its arms' radii are given by

$$R_Q = 0.5 \frac{\lambda_{max}}{4(\alpha + \delta)} \tag{3.5a}$$

$$R_1 = 1.2 \frac{\lambda_{min}}{4(\alpha + \delta)} \tag{3.5b}$$

where λ_{max} is the wavelength corresponding to the maximum radiation frequency, λ_{min} to the minimum radiation frequency, R_Q to the innermost radius and R_1 to the outermost radius. The reason the start radius is halved is to provide a transition region between the feed points and the first active region. Similarly, the end radius is increased in order to compensate for edge effects. Alongside the variables in (3.1), these are all the parameters required to describe a planar sinuous antenna's geometry.

The reason the antenna radiates is as follows. In an active region, the circumferential currents at the start and end of a cell are in phase. This is due to them travelling in opposite directions (since the current is reflected at the bend), but with one current delayed by 180° in phase relative to the other (due to the electrical path length). The protrusions at the bends also add shunt capacitance. This reduces undesired radiation patterns produced by the reflections.

For a 4 arm sinuous antenna, the arms act as transmission lines carrying an outwardly travelling wave when excited from the centre. The idea is to provide equivalent standing wave currents for each pair of arms. Then, for the full antenna, the active regions form radiating rings with a radial width a fraction of a wavelength. Figure 3.3 shows how the radiating active regions shrink as the frequency increases.

The planar sinuous antenna then radiates bidirectionally with one sense of polarization in each hemisphere. Depending on how it is excited, different radiation pattern shapes are possible.
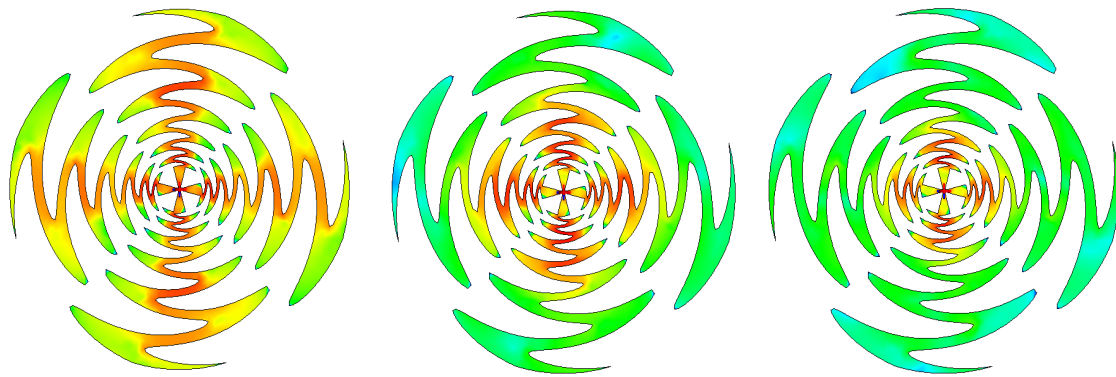
(a) Active regions at 2 GHz   (b) Active regions at 4 GHz   (c) Active regions at 6 GHz

Figure 3.3: Active regions of a sinuous antenna as a function of increasing frequency

For the general case, the voltage excitation for a sinuous arm is given by

$$V_{n,m} = A_m e^{j2\pi mn/N} \tag{3.6}$$

where $n = 1, 2, \cdots N$ is the arm number (with N the total number of arms), $m = +1, +2, \cdots N$ is the mode number and A_m is the complex amplitude of the excitation of mode m. When applying the same mode number for the voltage excitation on each arm, a rotationally symmetric radiation pattern is formed. A Different mode number leads to a different radiation pattern shape. All of these radiation patterns are rotationally symmetric and, except for mode $m = 1$ (which is the same as mode $m = N - 1$), have a null on-axis.

For example, exciting a 4 arm sinuous antenna with mode $m = 1$ in equation (3.6) means the voltage excitation for each arm will be $(+j; -1; -j; +1)$. The resulting dual circularly polarised radiation patterns in the H-plane are shown in Fig. 3.4(a). If $m = 2$ is applied instead in equation (3.6), the voltage excitation will be $(-1; 0; -1; 0)$. Its corresponding radiation pattern is shown in Fig. 3.4(b) with the null clearly visible. For applications as a feed in a reflector system, only the mode $m = 1$ is considered.
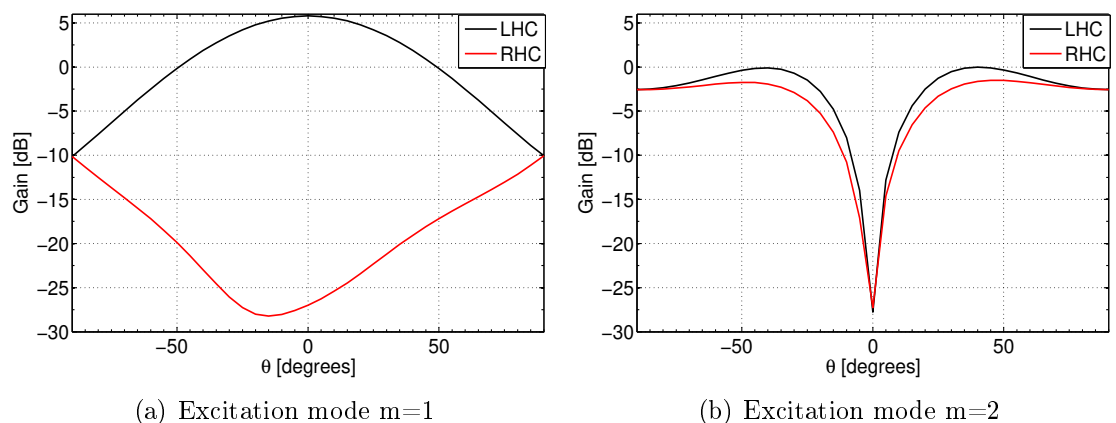
(a) Excitation mode m=1   (b) Excitation mode m=2

Figure 3.4: Gain of circularly polarised radiation pattern shapes for different excitation modes of a four arm planar sinuous antenna

A 4 arm planar sinuous antenna is capable of dual polarization – either circular or linear. To achieve circular polarization, the normalized voltage excitation for each arm is

[25] $(+1; \pm j; -1; \mp j)$. Thus opposite arms are driven differentially with respect to each other, while orthogonal arms are 90° out of phase relative to one another. For single linear polarization only one pair of opposing arms should be driven differentially while the other pair is terminated in a matched load. The resulting normalized voltage excitation is $(+1; 0; -1; 0)$. In the case of dual linear polarization both pairs of opposing arms should be driven differentially with each pair driven independently.

3.1.3   Feeding

When feeding the antenna there are various aspects to take into account. These include the input impedance, the feed point locations, and the actual feeding networks.

Starting with the input impedance, consider a self complimentary sinuous antenna. Self complimentary implies, for a planar structure, that interchanging the metallic area with the free space background does not change the antenna's geometry. This can be obtained if $\delta = \pi/2N$. Though it is not a requirement, if self complimentary is applied, the sinuous antenna's input impedance to ground of each arm is frequency independent and given by [26]

$$Z_m = \frac{30\pi}{\sin \frac{m\pi}{N}}. \tag{3.7}$$

When a 4 arm sinuous antenna is excited for either circular or linear polarization (in mode $m = 1$), this corresponds to an input impedance of 133 Ω. As a consequence of exciting opposing arms differentially, the terminal impedance of a pair of arms is double a single arm impedance, in other words 267 Ω.

Before connecting the antenna to a feed network the feeding region should be considered. The locations of the feeding points influence the radiation pattern, but can also allow for a simpler feeding network. In [27] a few feeding structures, shown in Fig. 3.5, were investigated. Note that overlapping sinuous arms can be achieved by printing them on opposite sides of a substrate. To summarise the observations, the default feeding point structure shown in Fig. 3.5(a) provided the most rotationally symmetric radiation pattern and lowest axial ratio over the frequency range. However, it requires a thoughtful feeding network that can untangle the antenna arm pairs. The other feeding structures, shown in Fig. 3.5(b) and 3.5(c), manage to untangle the antenna arms, but perform worse. Results from the structure shown in Fig. 3.5(d) were good due to it untangling the arm pairs while ensuring their electrical path lengths remain equal.

A schematic of the required feeding network is shown in Fig. 3.6. Opposing arms have to be differentially fed. Therefore, they are connected to baluns. Often the baluns are also used to transform the input impedance. For circular polarization, both baluns should be connected to a 3 dB quadrature hybrid. In the default feeding network two 8.3 dB hybrids are used in tandem to accomplish this.

Two practical feeding networks (excluding the hybrid) are shown in Fig. 3.7. Both require the antenna arm pairs to already be untangled and both include matching networks. The first, shown in Fig. 3.7(a), is a realization of a Marchand balun using a microstrip to slotline transition. The second, shown in Fig. 3.7(b), is a tapered microstrip balun. It is an attractive option since it is low cost and simple to manufacture.

3.1.4   Unidirectional Radiation

The sinuous antenna becomes useful when its radiation is pointing in one direction. There exists different methods to achieve this. A few are shown in Fig. 3.8.

(a) Default feeding scheme

(b) Alternative feeding scheme

(c) Overlapping feeding scheme

(d) Alternative overlapping feeding scheme
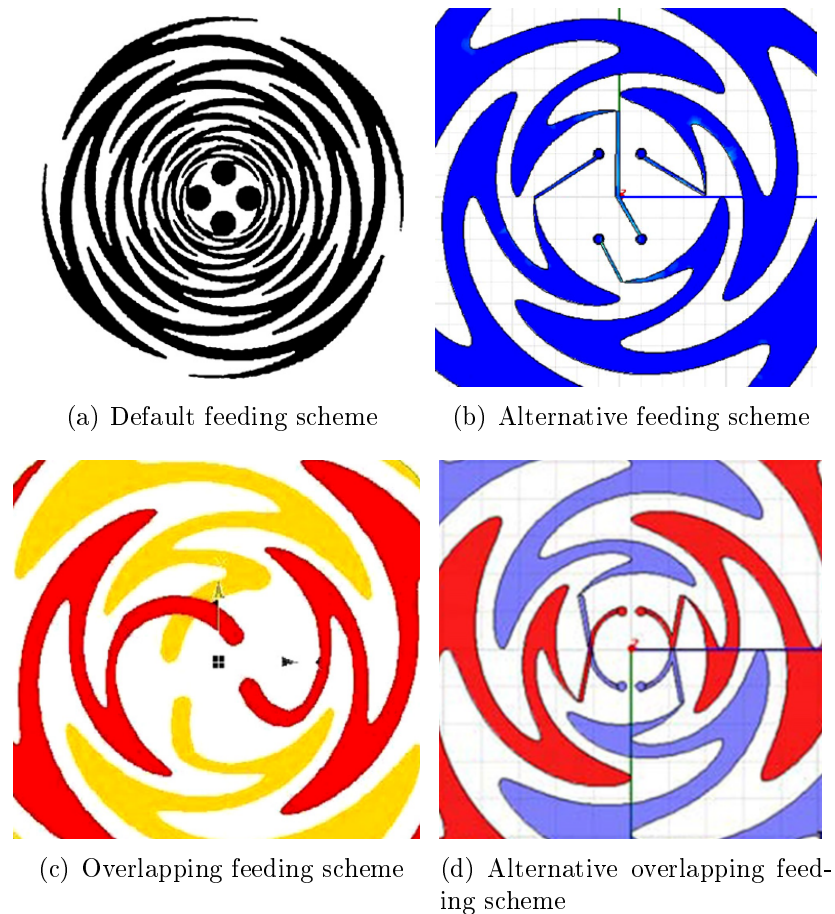
Figure 3.5: Different feed point locations for a sinuous antenna [27]
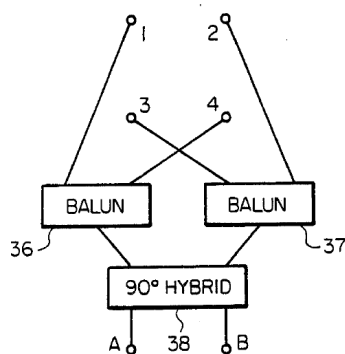
Figure 3.6: Schematic of standard feeding network for a circularly polarised four arm sinuous antenna [24]

The classic method [24], shown in Fig. 3.8(a), is to place a sinuous antenna above an absorbing cavity. The cavity reflects the back radiation which leads to unidirectional radiation. The absorbing material, however, also increases the antenna's noise temperature which prevents its use in radio astronomy applications.

In [11] a planar sinuous antenna was placed above a conducting ground plane as shown in Fig. 3.8(b). The ground plane reflects the back radiation like the cavity, but has no absorbing material to lessen performance. The antenna operated over a 3:1 bandwidth and achieved acceptable results when used as a reflector feed.

(a) Microstrip/slotline Marchand balun (b) Tapered microstrip balun
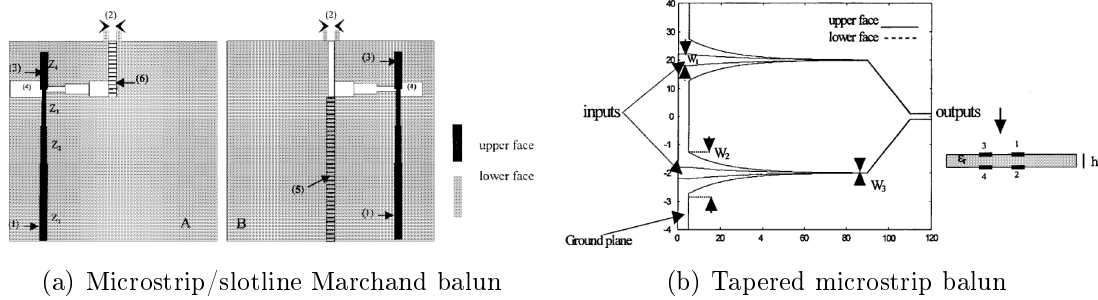
Figure 3.7: Different feeding networks for a sinuous antenna [28]

Another method projects the sinuous antenna onto a conical or pyramidal shape as shown in Fig. 3.8(c). This leads to improved front-to-back ratio. However, it also causes the phase centre of the antenna to move as a function of frequency which prohibits its use as reflector feed.

(a) Absorbing cavity [24]   (b) Reflecting ground plane   (c) Conical projection [24]
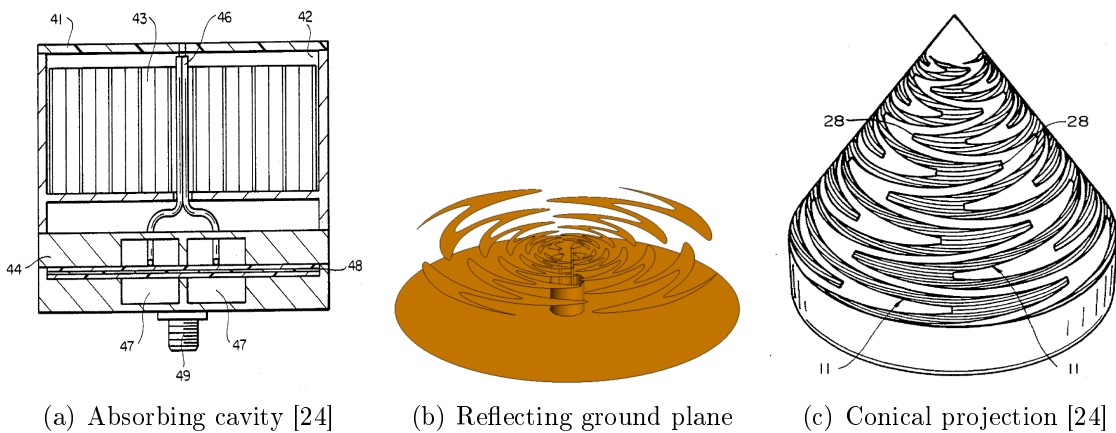
Figure 3.8: Different methods to obtain unidirectional radiation for sinuous antennas

3.2   Conical Sinuous Antenna

The conical sinuous antenna [10] garnered attention as a possible candidate for the SKA and other radio astronomy projects. Being based on the planar sinuous antenna, it shares many its progenitor's attractive qualities while adding unidirectional radiation and a near constant phase centre to the list. Consequently, a large portion of the previous section is still applicable. In the following section, the relevant differences of the antenna and their effects are presented.

3.2.1   Geometry

The conical sinuous antenna can be described as a planar sinuous antenna projected onto an inverted cone suspended above a conducting ground plane. It is shown in Fig. 3.9. Due to the ground plane the antenna can be loosely conceptualised as a plane reflector with the inverted cone as the feed. This explains why the antenna has a near constant phase

centre: the ground plane causes the cone to have an image which allows the structure to be symmetrical.
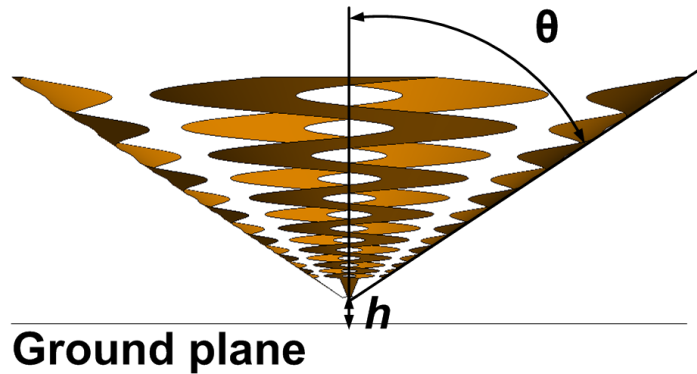
Figure 3.9: Side view of a conical sinuous antenna

Looking from the top, the antenna resembles its planar counterpart. Therefore, the geometry of the conical sinuous antenna includes all the parameters and definitions of the planar sinuous antenna, and adds the ground plane's radius, the cone's half angle, and the cone's height above the ground plane to the list.

Regarding the conducting ground plane, in [11] it was chosen as circular with a radius equal to a sinuous arm. It is explained that by doing so, the antenna's η_{BOR1} is prevented from deteriorating at certain frequencies.

For maximum broadside radiation, an active region should be placed a quarter wavelength above the ground plane. Then the backward travelling wave gets reflected by the ground plane, traverses half a wavelength and travels in phase with the forward travelling wave. To achieve this as a first order approximation the cone's half angle, defined as θ in the figure, can be determined with simple trigonometry and (3.4) as

$$\theta = \arctan\left(\frac{1}{\alpha + \delta}\right) \tag{3.8}$$

with the angles in radians.

However, in [10] it was shown that varying the conical sinuous antenna's parameters away from the standard configuration ($\alpha = 45°$ and $\delta = 22.5°$) one may improve the impedance match of the antenna. Adding to this, an extensive parametric study and optimization of the antenna was performed in [11]. All the design parameters (α, δ, τ and θ) were varied independently from each other while the cone's height above the ground plane, h, was kept constant. The optimisation showed various trade-offs in the antenna's return loss, aperture efficiency when used as dish feed, and cross-polarization isolation performance metrics. Optimal parameters were determined to achieve the best results for all the performance metrics. Afterwards, h was also varied to see its effect. Moving the cone closer to the ground plane increased the aperture efficiency and sharply decreased the return loss. Moving the cone away from the ground plane decreased both.

All the design parameters required to specify a conical or pyramidal sinuous antenna's geometry have been described and are summarised in Table 3.1.

Table 3.1: Design parameters of a conical sinuous antenna

Parameter	Description
α	Angular width
δ	Rotation angle
τ	Growth rate
θ	Cone's half angle
h	Cone's height above ground plane
f_{min}	Minimum frequency used to determine outer radius
f_{max}	Maximum frequency used to determine inner radius

3.2.2 Feeding

While gaining some attractive qualities, the conical sinuous antenna loses other features. A prominent one involves the input impedance becoming frequency dependent due to the ground plane. A feeding network used by [10] to address this is explained next.

Using the default feeding region, opposite arms of the antenna are connected with twin lines with a characteristic impedance given by [29]

$$Z_c = \frac{120}{\sqrt{\epsilon_r}} \arccos\left(\frac{D}{d}\right) \tag{3.9}$$

where D is the distance between the conductors' centre and d are their diameters. If Z_C is close to the real part of an antenna arm pair's input impedance, then a length of twin lines will gradually reduce the impedance's real part and change its reactive part from inductive to capacitive. Therefore, it is important to keep the lines' length short.

The lines pass through a hole in the center of the ground plane whereafter each line is connected to its own LNA (specifically designed for the correct higher input impedance). Afterwards they are connected to commercial 180° hybrid couplers at the difference ports.

In [11] each line is instead connected to a stepped impedance matching network. It should be stressed that direct connection to LNAs is the preferred approach for wideband applications. This is in order to reduce loss in the matching network. In general, the design of the LNAs is not a trivial task - especially for cryogenic applications - and remains an active research field outside the scope of this thesis.

3.3 Mixed Mode S-Parameters

In the previous section it was stated that the sinuous antenna is differentially excited. While circuits are commonly described by their S-parameters, it is often advantageous to characterize differential circuits by their Mixed Mode S-parameters. In the coming simulations and measurements, the antenna arms will be individually excited and only the standard S-parameters will be available. Therefore, this section briefly explains how the available standard S-parameters can be transformed to their equivalent Mixed Mode S-parameters according to [30].

Consider a single ended 4-port Device-Under-Test (DUT) as shown in Figure 3.10(a).

(a) A single ended 4-port DUT (b) A differential 2-port DUT
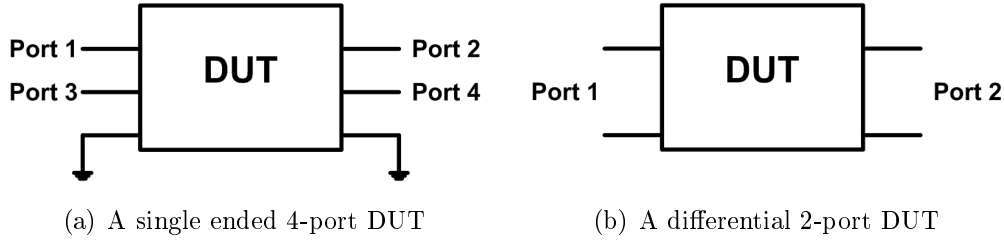
Figure 3.10: Equivalent DUT's

Its standard S-parameters are given by

$$B_{std} = S_{std}A_{std}$$

$$\begin{bmatrix} b_1 \\ b_2 \\ b_3 \\ b_4 \end{bmatrix} = \begin{bmatrix} S_{11} & S_{12} & S_{13} & S_{14} \\ S_{21} & S_{22} & S_{23} & S_{24} \\ S_{31} & S_{32} & S_{33} & S_{34} \\ S_{41} & S_{42} & S_{43} & S_{44} \end{bmatrix} \begin{bmatrix} a_1 \\ a_2 \\ a_3 \\ a_4 \end{bmatrix} \tag{3.10}$$

where b_i is a port's normalized reflected power wave and a_i is a port's normalized incident power wave.

Next, consider a differential 2-port DUT as shown in Fig. 3.10(b). Its Mixed Mode S-parameters are given by

$$B_{mm} = S_{mm}A_{mm}$$

$$\begin{bmatrix} b_{d1} \\ b_{d2} \\ b_{c1} \\ b_{c2} \end{bmatrix} = \begin{bmatrix} S_{d1d1} & S_{d1d2} & S_{d1c1} & S_{d1c2} \\ S_{d2d1} & S_{d2d2} & S_{d2c1} & S_{d2c2} \\ S_{c1d1} & S_{c1d2} & S_{c1c1} & S_{c1c2} \\ S_{c2d1} & S_{c2d2} & S_{c2c1} & S_{c2c2} \end{bmatrix} \begin{bmatrix} a_{d1} \\ a_{d2} \\ a_{c1} \\ a_{c2} \end{bmatrix} \tag{3.11}$$

where b_{di} refers to a port's differential-mode response, b_{ci} refers to a port's common-mode response, a_{di} refers to a port's differential-mode stimulus and a_{ci} refers to a port's common-mode stimulus.

Then, let port 1 and 3 in Fig. 3.10(a) be connected as a single differential port and port 2 and 4 as another differential port. Thus the circuit resembles the one in Fig. 3.10(b). In [31] it was shown that the single ended incident and reflected waves are related to the differential incident and reflected waves as

$$A_{mm} = MA_{std}$$

$$\begin{bmatrix} a_{d1} \\ a_{d2} \\ a_{c1} \\ a_{c2} \end{bmatrix} = \frac{1}{\sqrt{2}} \begin{bmatrix} 1 & 0 & -1 & 0 \\ 0 & 1 & 0 & -1 \\ 1 & 0 & 1 & 0 \\ 0 & 1 & 0 & 1 \end{bmatrix} \begin{bmatrix} a_1 \\ a_2 \\ a_3 \\ a_4 \end{bmatrix} \tag{3.12}$$

$$B_{mm} = MB_{std}$$

$$\begin{bmatrix} b_{d1} \\ b_{d2} \\ b_{c1} \\ b_{c2} \end{bmatrix} = \frac{1}{\sqrt{2}} \begin{bmatrix} 1 & 0 & -1 & 0 \\ 0 & 1 & 0 & -1 \\ 1 & 0 & 1 & 0 \\ 0 & 1 & 0 & 1 \end{bmatrix} \begin{bmatrix} b_1 \\ b_2 \\ b_3 \\ b_4 \end{bmatrix} \tag{3.13}$$

with the conversion matrix and its inverse given as

$$M = \frac{1}{\sqrt{2}} \begin{bmatrix} 1 & 0 & -1 & 0 \\ 0 & 1 & 0 & -1 \\ 1 & 0 & 1 & 0 \\ 0 & 1 & 0 & 1 \end{bmatrix} \tag{3.14}$$

$$M^{-1} = \frac{M^*}{|M|} = \frac{1}{\sqrt{2}} \begin{bmatrix} 1 & 0 & 1 & 0 \\ 0 & 1 & 0 & 1 \\ -1 & 0 & 1 & 0 \\ 0 & -1 & 0 & 1 \end{bmatrix}. \tag{3.15}$$

Substituting 3.12 and 3.13 into 3.10 leads to

$$B_{std} = S_{std}A_{std}$$
$$M^{-1}B_{mm} = S_{std}M^{-1}A_{mm}$$
$$B_{mm} = MS_{std}M^{-1}A_{mm}. \tag{3.16}$$

Thus the mixed mode S-parameters can be calculated from the standard S-parameters as

$$S_{mm} = MS_{std}M^{-1}$$

$$S_{mm} = \frac{1}{2} \begin{bmatrix} S_{11} - S_{13} - S_{31} + S_{33} & S_{12} - S_{14} - S_{32} + S_{34} \cdots \\ S_{21} - S_{23} - S_{41} + S_{43} & S_{22} - S_{24} - S_{42} + S_{44} \cdots \\ S_{11} - S_{13} + S_{31} - S_{33} & S_{12} - S_{14} + S_{32} - S_{34} \cdots \\ S_{21} - S_{23} + S_{41} - S_{43} & S_{22} - S_{24} + S_{42} - S_{44} \cdots \end{bmatrix}$$

$$\begin{matrix} \cdots S_{11} + S_{13} - S_{31} - S_{33} & S_{12} + S_{14} - S_{32} - S_{34} \\ \cdots S_{21} + S_{23} - S_{41} - S_{43} & S_{22} + S_{24} - S_{42} - S_{44} \\ \cdots S_{11} + S_{13} + S_{31} + S_{33} & S_{12} + S_{14} + S_{32} + S_{34} \\ \cdots S_{21} + S_{23} + S_{41} + S_{43} & S_{22} + S_{24} + S_{42} + S_{44} \end{matrix}. \tag{3.17}$$

Chapter 4

Pyramidal Sinuous Antenna

The conical sinuous antenna was assessed in [11] as part of a larger study. In that thesis a $2-6$ GHz version was designed, optimised and manufactured. To summarise the results, the simulated model showed promising performance, but the manufactured model did not. The reason was due to the manufactured model's physical deviations from the simulated model. Due the fabrication process, unwanted interleaving occurred between the antenna's arms. In addition, the structure did not adhere to a cone's shape – especially near its feeding points. This resulted in the manufactured model's performance being significantly worse than its simulated counterpart.

As a follow-up to that study, an inverted pyramidal sinuous antenna suspended over a conducting ground plane is investigated in this chapter. A pyramid has flat sides which should allow the antenna's arms to be easily manufactured using standard, low cost printed circuit board processes. Furthermore, unwanted interleaving and structural deviations should not occur. Though in theory it has an improved manufacturing process, this has yet to be tested. It still has to be established whether a model can be easily made that would perform as its simulation predicted.

In this chapter the modelling, construction and measuring of a $2-6$ GHz pyramidal sinuous antenna is presented. The methods and nuances taken into account for each phase is given. A closer look is also taken at the effects of the antenna's feeding network. In the end the performance results are presented and comparisons are made to a conical sinuous antenna counterpart.

4.1   Modelling

A step-by-step approach was undertaken to model the full antenna. Starting with a base model, new sections were added one-by-one to determine each section's effect on the overall performance. As the foundation of the approach, a parametric model of the pyramidal sinuous antenna was made in FEKO [32]. The model uses the same design parameters as the optimised conical sinuous antenna in [11] in order to compare the two's performance later on. Table 4.1 provides their design parameter values. The main difference between the two models is simply the surface onto which the sinuous curve is projected. Figure 4.1 shows the two antennas and highlights their different projection shapes.

In order to feed the base model, opposing arms are connected with edge ports so that they can be excited differentially. Figure 4.2 shows a top view of the pyramidal sinuous antenna with a close up of its feeding structure. Note that one arm pair's port crosses above the other arm pair's port.

Table 4.1: Design parameters of a pyramidal sinuous antenna

Parameter	Value
α	24.85°
δ	14.95°
τ	0.842
θ	56.48°
h	5 mm
f_{min}	2 GHz
f_{max}	6 GHz
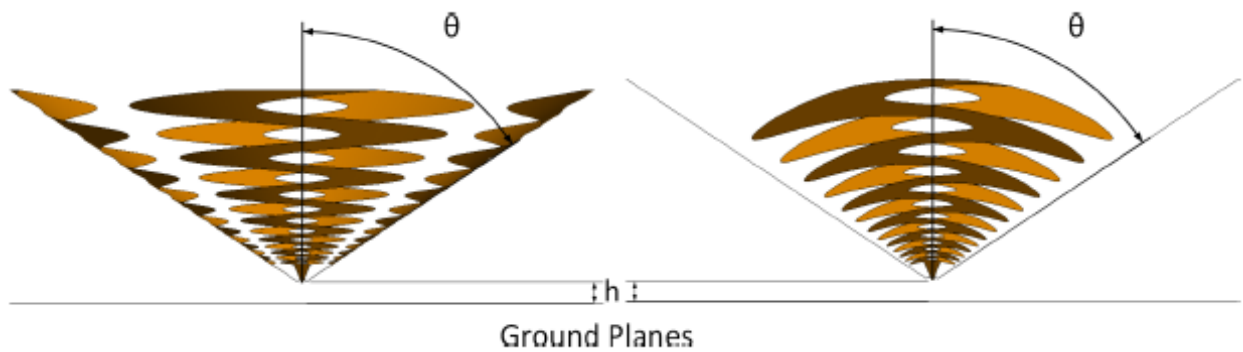
Figure 4.1: Side views of the conical sinuous antenna (left) and the pyramidal sinuous antenna (right).

The port impedances were chosen as $Z_{in} = 300$ Ω as was done in [11]. For the far-field simulations only one pair of arms was excited differentially, thus corresponding to a single linear polarization (see previous chapter on how to excite the sinuous antenna for this case).
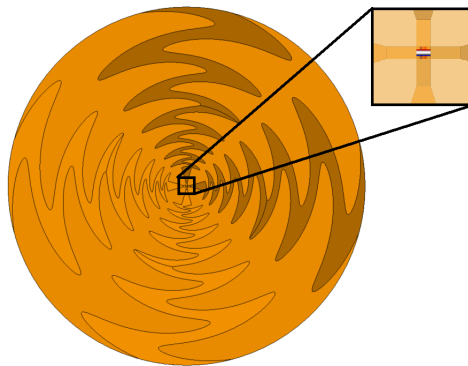
Figure 4.2: Top view of pyramidal sinuous antenna.

How to simulate the base model has to be discussed before new sections can be added to it. A trade-off exists in Method-of-Moment solvers between the accuracy of a simulation and the simulation time. While a minimum level of accuracy is necessary, increasing it further quickly leads to inefficient solving times. Finding a proper balance between the two is an important place to start the design process.

4.1.1   Mesh Study

To simulate the model it first needs to be segmented into a mesh. A denser mesh leads to a better geometrical representation of the antenna as well as a more accurate simulation result. This comes at the cost of an exponentially larger matrix to solve and, consequently, a longer simulation time.

A mesh study was performed on the base model to determine the appropriate mesh necessary for the simulations. Different meshes were used to segment the base model. The sizes of the mesh elements were chosen as $\lambda_{max}/8$, $\lambda_{max}/12$, $\lambda_{max}/16$ and $\lambda_{max}/20$ where λ_{max} is the wavelength at the maximum frequency. Two important performance metrics, the differential reflection coefficient and the gain, were analysed using the different meshes. Their performances are shown in Fig. 4.3(a) and 4.3(b), respectively. Reflection coefficients were simulated over the frequency range while the antenna's gain patterns were simulated over the polar angle for frequencies 2, 4 and 6 GHz. Only the last frequency point's results are shown for the gain patterns, since it is where the difference in the meshes' performance is the largest.

To compare the results of the different meshes, the absolute difference between each mesh's performance and the mesh with the smallest element size were taken ($|x_{\text{compare}} - x_{\lambda/20}|$ where x refers to either the differential reflection coefficient or the gain pattern). They are shown in Fig. 4.3(c) and 4.3(d) for reflection coefficient and gain, respectively.

(a) Differential reflection coefficent   (b) Directive gain at 6 GHz

(c) Reflection coefficient difference   (d) Directive gain difference
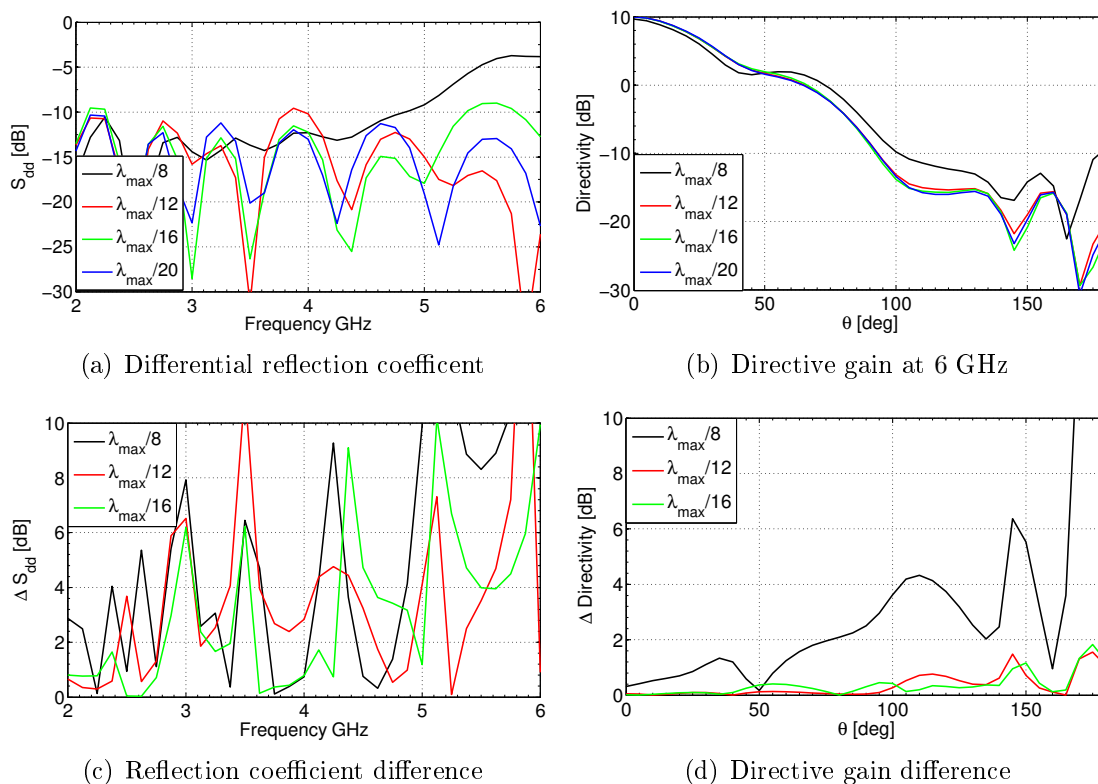
Figure 4.3: The differential reflection coefficient (a) and directive gain (b) of an increasingly finer meshed antenna and their absolute difference, (c) and (d), respectively, to the smallest mesh size.

A few observations can be made. The first thing to note is that the directive gain, and by implication the far-fields, are much less sensitive to the density of the mesh than the port parameters. This is due to the calculation of far-fields involving the averaging of

the equivalent source currents. The effects of current source outliers are diminished when averaged. It was seen that only the gain from the sparsest mesh showed a significant discrepancy from the other meshes' gain. Added to this, the discrepancy only became notable at higher frequencies. All the other meshes perform similarly with regard to the gain.

The reflection coefficients, however, tell a different tale. All the meshes' performance deviate from the densest mesh's performance. This difference increases at higher frequencies. To illustrate that point, the mean difference was taken over half the frequency range as well as over the entire frequency range between each mesh's reflection coefficient and the densest mesh's reflection coefficient. They are given in Table 4.2. It should be mentioned that the calculations also take into account the differences at the troughs of the reflection coefficients, which are actually irrelevant. Over the entire bandwidth the mean difference between the densest and second densest mesh is 3.2 dB while over half the bandwidth it reduces to 1.6 dB.

Table 4.2: Mean S_{dd} difference for various mesh sizes

Mesh size	$2 - 4$ GHz	$2 - 6$ GHz
$\lambda_{\max}/8$	2.8 dB	5.4 dB
$\lambda_{\max}/12$	3 dB	3.6 dB
$\lambda_{\max}/16$	1.6 dB	3.2 dB

From the observations made above, two conclusions can be made:

- A very dense mesh is required to accurately describe the performance of the base model – especially at the higher frequencies. Although the results of the gain patterns have converged, the results for the differential reflection coefficient have not. Unfortunately, the simulation time becomes unjustifiably long. Since a reflection coefficient of -10 dB is aimed for, being a few dB's inaccurate near the end of the frequency range was considered acceptable.

- Using the same very dense mesh is excessive to describe the performance accurately at the lower frequencies. A less dense mesh is sufficient for them.

Based on these conclusions it was decided to use two meshes to cover the pyramidal sinuous antenna. The transition of the meshes occurs at the active region, as determined by (3.4), corresponding to the geometrical mean frequency as given by

$$f_{\mathrm{mean}} = \sqrt{f_{\min}f_{\max}}. \tag{4.1}$$

For a $2-6$ GHz antenna, this equates to $f_{\mathrm{mean}} = 3.46$ GHz. Active regions corresponding to the lower frequencies were covered by a mesh with the element size $\lambda_{max}/16$, while active regions corresponding to the higher frequencies were covered by a mesh with element size $\lambda_{max}/20$.

A final observation was made in regard to the ground plane. The ground plane, unlike the sinuous arms, is an electrically large, but uncomplicated area. As shown in Fig. 4.4, the surface current magnitude over it exhibits very little variance, even at the highest frequency. Consequently, a coarse mesh with element size $\lambda_{max}/8$ proved sufficient to cover it without losing information about the model's performance.
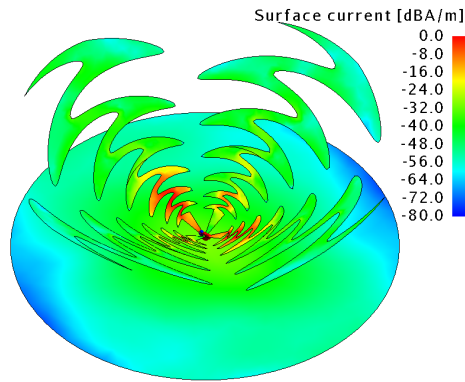
Figure 4.4: Normalised surface current on antenna at 6 GHz.

4.1.2 Frequency Points

The following step is to decide at which frequencies to simulate. Sampling the model at many frequency points means a longer total simulation time; assessing the model at few frequency points may lead to a loss of its true performance. The following rationalization was used to choose the required number of frequency points.

Pyramidal sinuous antennas, as previously discussed, are derived from planar sinuous antennas and share many of their characteristics. Planar sinuous antennas are part of the log-periodic family of antennas. These antennas exhibit a logarithmically periodic structure which results in their logarithmically periodic performance over frequency [12]. The performance repeats itself at two frequencies related to each other by

$$f_2\tau = f_1, \quad f_2 > f_1 \tag{4.2}$$

with τ the same growth rate as defined in (3.2). Comparing (3.2) and (4.2) shows they are two sides of the same coin.

Over an entire frequency range the performance will logarithmically repeat itself n times. The number of repetitions can be calculated according to

$$f_{\max}\tau^n \leq f_{\min}$$
$$n \geq \frac{\log\left(\frac{f_{\min}}{f_{\max}}\right)}{\log(\tau)} \tag{4.3}$$

where the comparison sign flips due to $\log(\tau) < 0$. Applying (4.3) for the values given in Table 4.1 ($f_{\min} = 2$ GHz, $f_{\max} = 6$ GHz and $\tau = 0.842$) means the performance can be expected to contain (when rounded up) $n = 7$ periods. To adequately capture the performance in one period, it was decided to sample at least 5 frequency points in it. Thus in total the simulation of the base model is conducted over $7 \times 5 + 1 = 36$ logarithmically spaced frequency points.

In Fig. 4.5 two simulations of the same model, one finely sampled and the other sampled as described above, are shown. It is evident that the sparsely sampled model still captures the necessary information as its finely sampled equivalent.

4.1.3 Feed Network

With the base model's simulation aspects explained, the feeding network can be investigated. As previously described, the feeding network consists of each antenna arm connecting through the use of a pin to a stepped impedance matching network. New sections
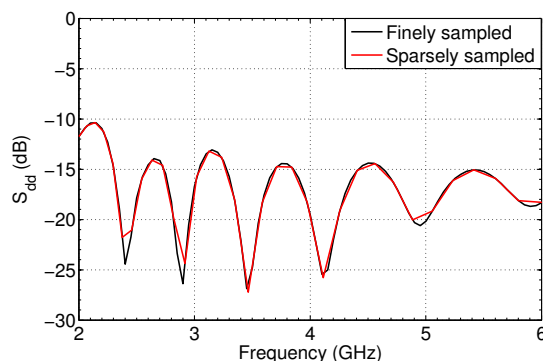
Figure 4.5: Comparison of a model with many frequency points and a model with few frequency points.

of the feeding network were added to the base model one-by-one and each section's effect compared to the base model. Also, the effect of etching the antenna arms and the matching network on dielectric substrates were studied.

As a reference to its potential capabilities, the base model's performance is presented first in Fig. 4.6. The differential reflection coefficients of its two ports are shown in Fig. 4.6(a). Their maximum values are -10 dB, which occur at the start of the frequency range. They remain below it over the rest of the spectrum. In Fig. 4.6(b) the input impedance at a single port is illustrated. As was expected, it varies as a function of frequency. However, the mean real impedance is 280 Ω which is close to the chosen port impedance of $Z_{in} = 300$ Ω. The normalised co-polar and cross-polar radiation fields in the E-plane are shown in Fig. 4.6(c). It can be seen the patterns maintain their symmetry throughout the frequency range. The aperture efficiency of the antenna in an equivalent prime-fed paraboloid reflector system with subtended angle $\theta_0 = 48°$ is shown in Fig. 4.6(d). The minimum aperture efficiency is $\eta_{ap} = 65\%$. In the forthcoming results, the reflection coefficient and the aperture efficiency are used to compare the models' performance. Note in the following graphs of the aperture efficiency, unless stated otherwise, solid lines correspond to the base model while dashed lines relate to the model being compared.

Effect of Pins and Ground Hole

The first addition of the feed network is to add pins to the antenna arms. Since they have a chosen diameter of $d = 0.5$ mm and an impedance of $Z_{in} = 300$ Ω is required between a pair of pins, the centre distance between them was determined using (3.9) as $D = 3.1$ mm.

These pins were passed through a hole in the ground plane. Two models are showcased to describe the effects of the pins and ground hole. The one with a larger hole is shown in Fig. 4.7 and the one with a smaller hole is shown in Fig. 4.8.

It is evident from the graphs that minor changes occur. In Fig. 4.7(c) slight deterioration occurs in the spillover efficiency at the higher frequencies. It is assumed that the hole in the ground allows higher frequency waves to escape through it instead of being reflected. Shrinking the hole, as seen in Fig. 4.8(c), nullifies this effect.

The differential reflection coefficient for both models, shown in Fig. 4.7(b) and 4.8(b), are fairly similar. They are slightly shifted from, and lower than, the base model's case. This is due the short length of the pins which marginally alter the input impedance.

(a) Differential reflection coefficent

(b) Input impedance

(c) Copolar and cross polar fields

(d) Aperture efficiency with $\theta_0 = 48°$
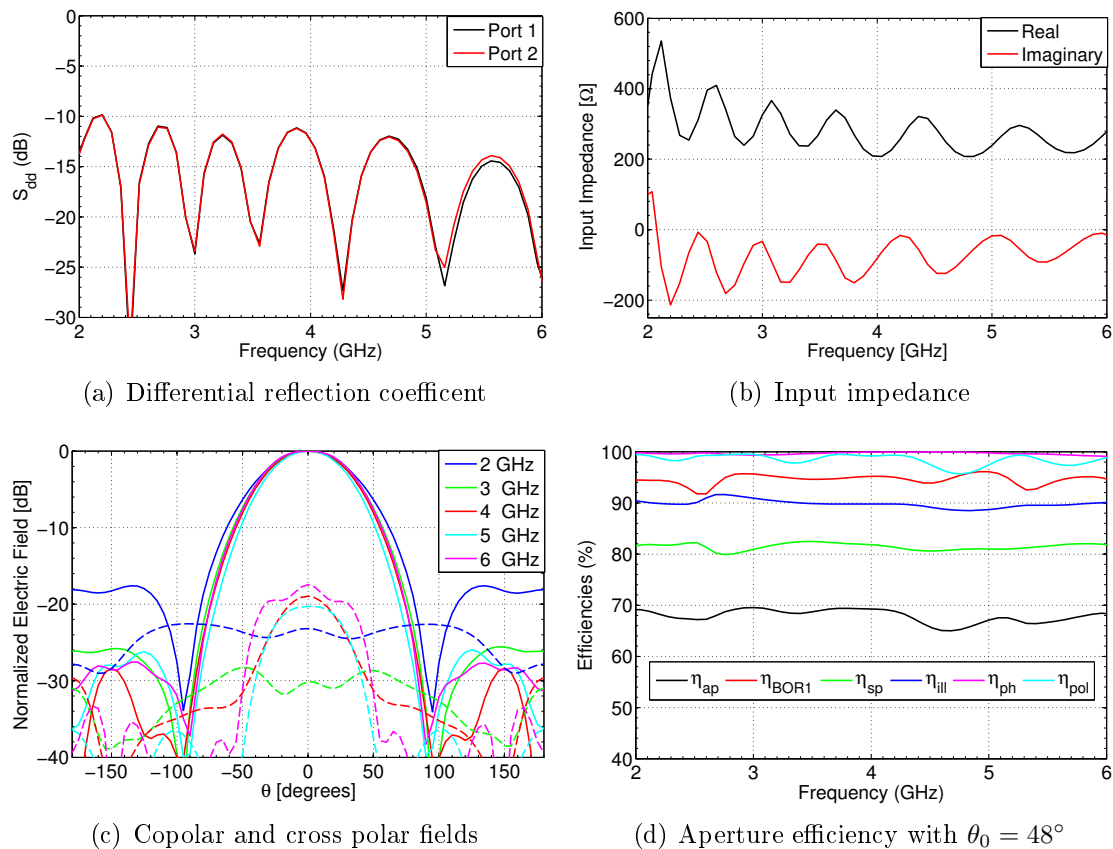
Figure 4.6: Performance of base antenna

Thus, to summarise, a small hole in the ground and short pin lengths have little effect on the base model's performance.

Effect of Substrates

The second addition is to study the effect of substrates. They are required for the arms and the matching network, and lead to an immense increase in the number of mesh cells. Consequently, they also increase the simulation time. Two models are used to illustrate their effect. The first model is the base model with the substrates applied to the antenna arms. The second model adds the pins to the arms that pass through the ground hole and through a small substrate block.

From the available substrates Rogers 4003C was chosen. It has a dielectric constant of $\epsilon_r = 3.38$. The height of the antenna arms' substrate is 0.508 mm. It is kept thin in order to lessen its effect on the radiation. Contrarily, the height of the substrate block is 1.524 mm. If characteristic impedance is kept constant, then a thicker substrate allows a microstrip line to be wider. With the available manufacturing equipment, this was preferred over a narrow track.

The first model and its performance are shown in Fig. 4.9. As can be seen in the graphs, both the differential reflection coefficient and the aperture efficiency are shifted to the left when compared to the base model. The shift becomes more pronounced as the frequency increases.

The second model is shown in Fig. 4.10. After the pins pass through the substrate block, they are split up into four single-ended transmission lines. The new port

(a) Model

(b) Reflection coefficient

(c) Aperture efficiency with $\theta_0 = 48°$
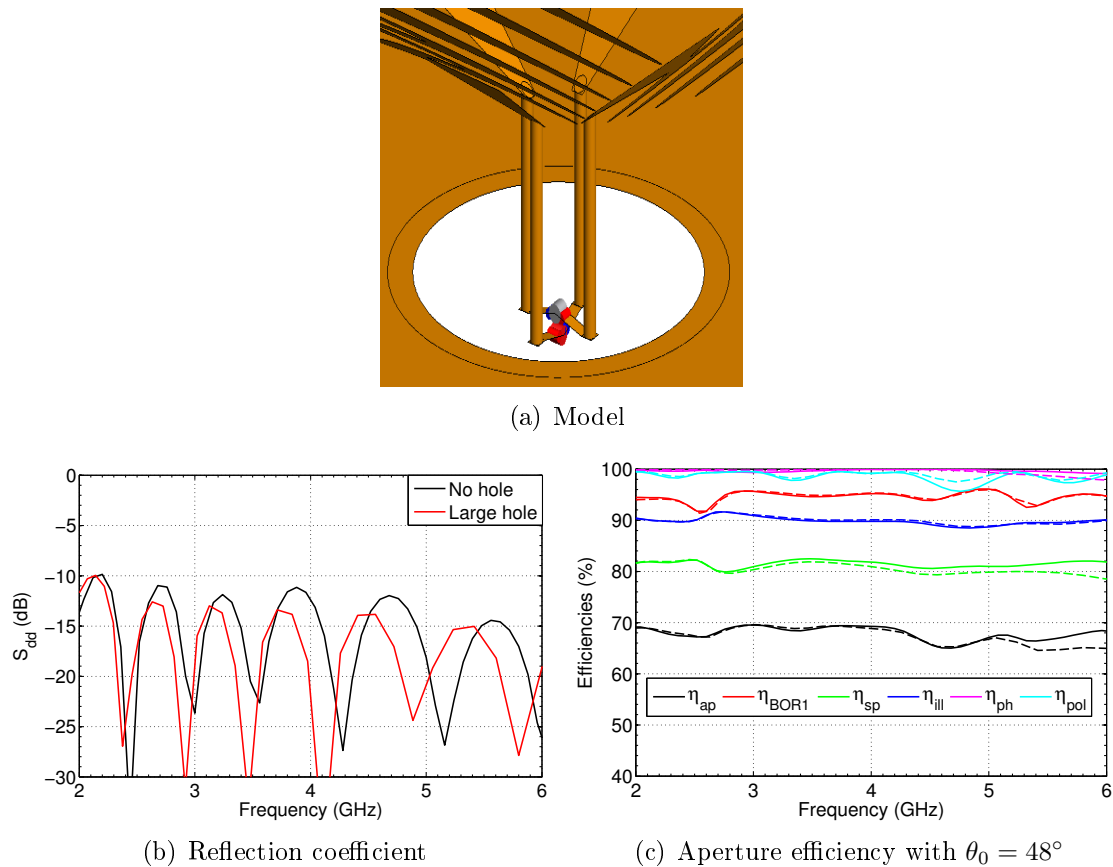
Figure 4.7: Performance of antenna with large hole. For aperture efficiency, the solid lines represent the base model while the dashed lines represent the model being compared.

impedances were selected based on the following rationalization. Consider the simplified schematic of a pair of antenna arms shown in Fig. 4.11. From its definition [33], the differential impedance of two symmetric transmission lines is twice the odd-mode impedance of a single transmission line as given by

$$Z_{\text{diff}} = 2Z_{0o}. \tag{4.4}$$

If the lines are uncoupled, then the odd-mode (and even-mode) impedance of a line is the same as its characteristic impedance. This leads to (4.4) becoming

$$Z_{\text{diff}} = 2Z_0 \tag{4.5}$$

with Z_0 the characteristic impedance. Therefore, given that the input impedance of a pair of arms was previously chosen as $Z_{in} = 300 \ \Omega$, and assuming that the transmission lines are uncoupled once they split up, the single ended port impedances were chosen as $Z_{\text{port}} = 150 \ \Omega$.

The performance of the model is shown in Fig. 4.10(b) and 4.10(c). Note that the mixed mode S-parameters, as explained in Chapter 3.3, are used to describe it. For convenience it is repeated here as

$$S_{d1d1} = \frac{1}{2} \left(S_{11} - S_{13} - S_{31} + S_{33} \right) \tag{4.6}$$

where port 1 and 3 are on opposite ends of the model.

(a) Model

(b) Reflection coefficient

(c) Aperture efficiency with $\theta_0 = 48°$

Figure 4.8: Performance of antenna with small hole

The shift between the two models' graphs is still due to the substrate on the arms. The degradation in the reflection coefficient is due to the pins passing through the ground substrate. A mismatch occurs between the pins in free space and the pins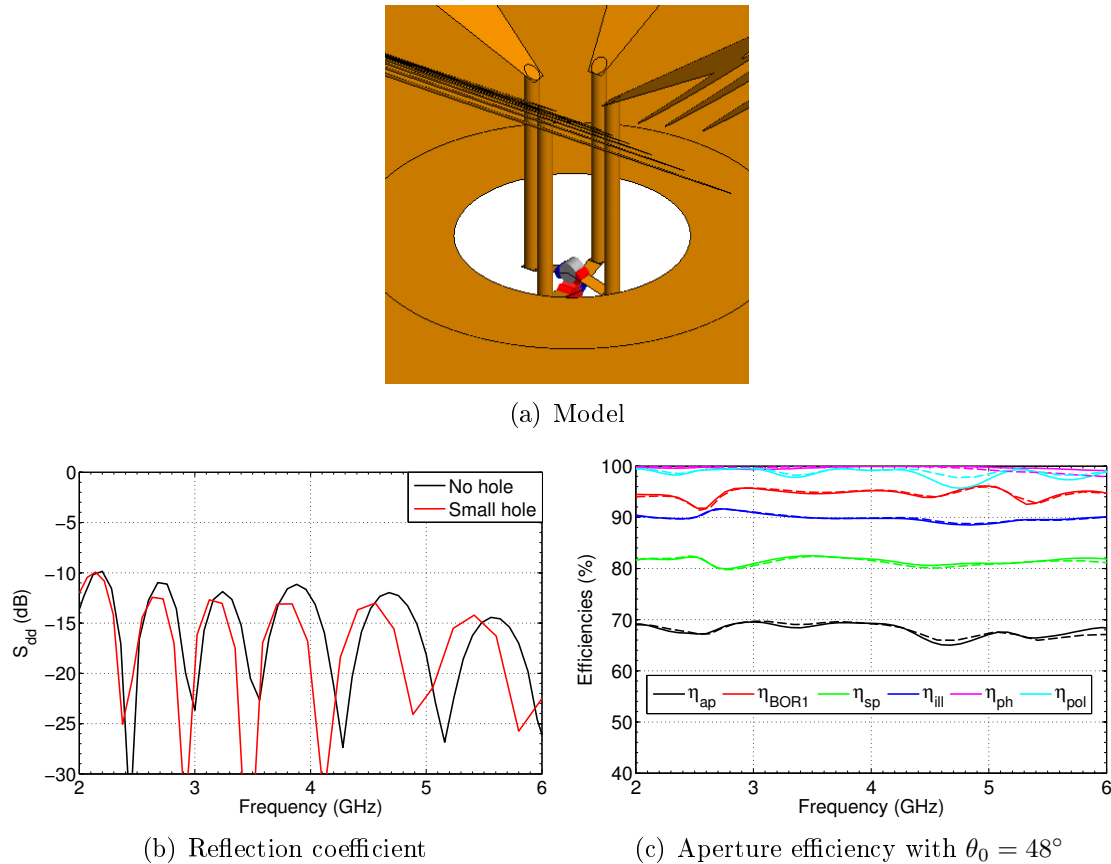 in the substrate due to the different dielectric constants of the media involved. At the band edge, a drop in the BOR1 efficiency is noticed.

This model was used to design and optimise a matching network in a circuit solver. To summarise, the substrates on the arms shifted the performance while the pins passing through ground substrate increased the reflection coefficient.

Effect of Matching Network

The final phase is about a matching network that transforms the port impedance to 50 Ω so that the antenna can be measured. To accomplish this, the standard S-parameters of the previous model were imported into Microwave Office [34]. A third order microstrip stepped impedance transformer was then designed and added to each of the imported model's ports. The width and length of each section were optimised for a less than -10 dB differential reflection coefficient. Take note this means the optimization was applied to S_{d1d1} and not to S_{11}. Table 5.3 provides the optimised values. A circuit schematic is shown in Fig. 4.12(a) alongside its differential reflection coefficient in Fig. 4.12(b). At the very end of the frequency range, a maximum value of -5.5 dB is reached.

A corresponding matching network of the circuit schematic was added to the FEKO model. The view of its underside is given in Fig. 4.13(a) with the matching network shown. As is evident, the ground plane is used for both the antenna and the microstrip

(a) Model

(b) Reflection coefficient

(c) Aperture efficiency with $\theta_0 = 48°$
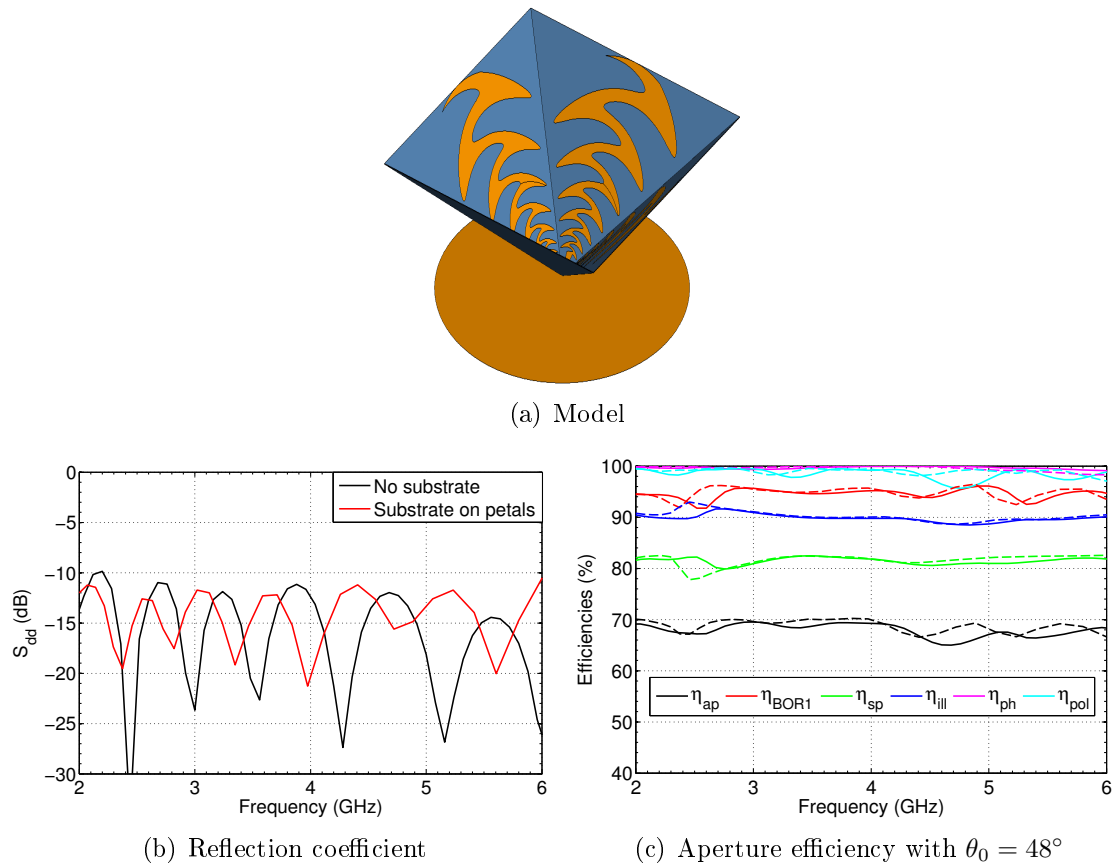
Figure 4.9: Performance of antenna with subbstrate on arms

Table 4.3: Values for third order stepped impedance transformer

Parameter	Value
w_1	0.8 mm
w_2	1.8 mm
w_3	3 mm
length	12.8 mm

line. This allows the antenna to have a lower profile than is possible with the other feeding networks that were explained. In order to reduce the simulation time, substrates on the antenna arms were omitted from the model. Based on previous observations, it was assumed, but not confirmed, the omission would only shift the actual performance results.

As shown in Fig. 4.13, the performance of this model still resembles the base model – especially at the lower frequencies. The reflection coefficient, shown in Fig 4.13(b), is mainly below −10 dB with a jump at the start of the band to −8 dB. If the substrates were added to the antenna arms, however, its reflection coefficient would be expected to perform according to Fig. 4.12(b). The aperture efficiency, shown in Fig. 4.13(c), starts to degrade at the higher frequencies, but remains above 62%. This model's physical parameters were used in the fabrication process and its performance was used to compare to the measured results.

(a) Model

(b) Reflection coefficient

(c) Aperture efficiency with $\theta_0 = 48°$
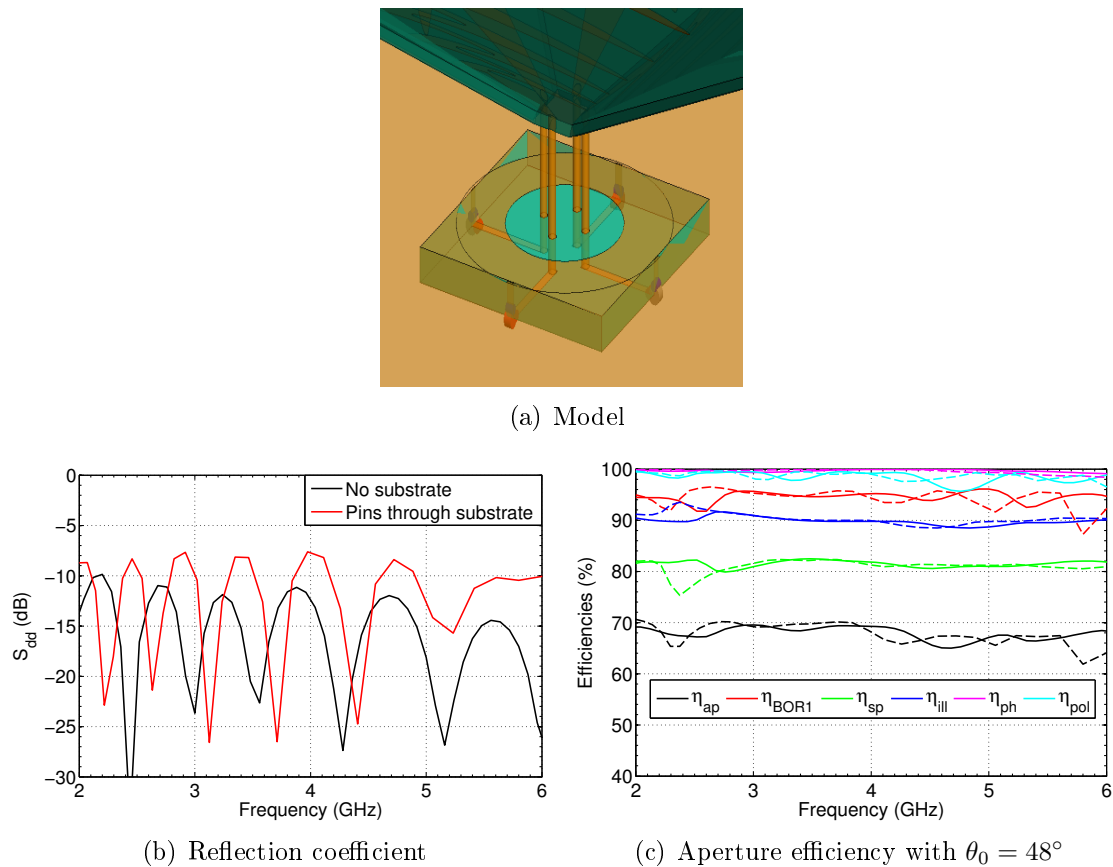
Figure 4.10: Performance of antenna with substrate on arms and pins passing though a substrate block
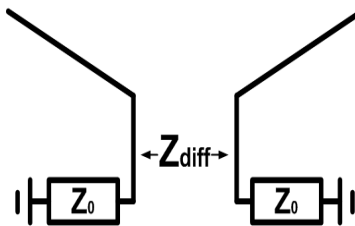
Figure 4.11: Schematic of a pair of antenna arms

4.2   Construction and Measuring

Though both are straightforward processes, the manufacturing and measuring of the antenna do contain certain nuances. The former has certain inherent challenges while the latter was accomplished in a specific manner. Details applicable to each are discussed next.

4.2.1   Construction

Fabrication of the antenna was done in the department's workshop. Four identical arms and a ground plane with matching network underneath were etched onto Rogers 4003C substrates with dielectric constant of $\epsilon_r = 3.38$. The substrate with a thickness of 0.508 mm was used for the antenna arms and the substrate with a thickness of 1.524 mm
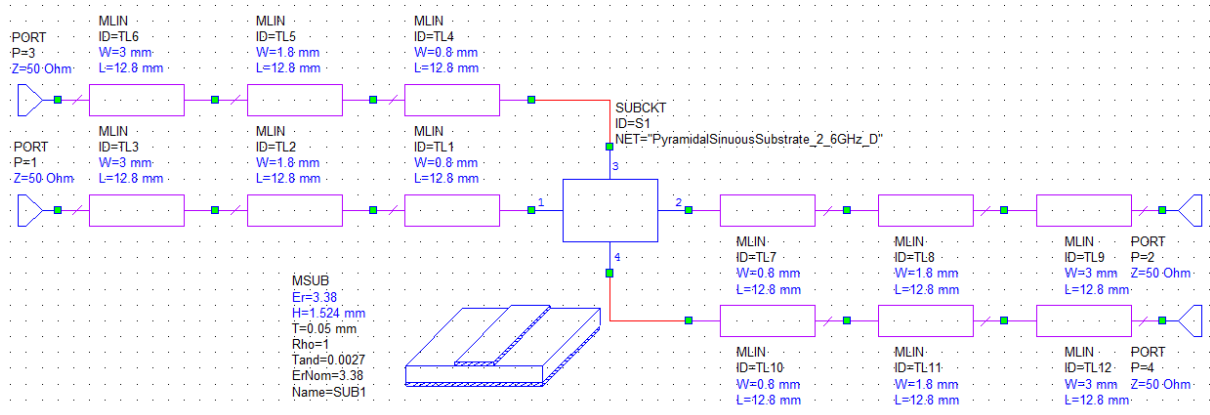
(a) Schematic
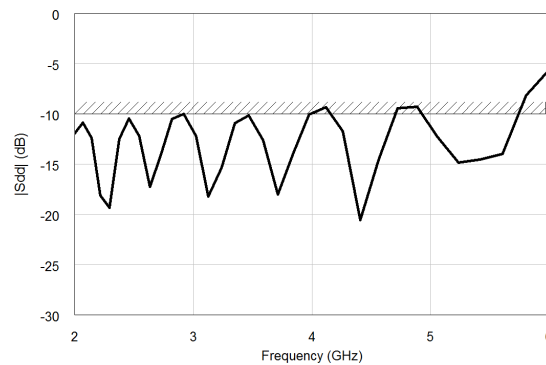
(b) Reflection coefficient

Figure 4.12: Schematic of matching network and differential reflection coefficient

was used for the ground plane / matching network. Holes were drilled in all of them to allow the pins to pass through.

The antenna arms were connected in a pyramidal shape using sticky tape. Though it is quick and easy to assemble them, the pyramidal structure does not have a strict 34° half-angle for each side.

Pins with a 0.5 mm diameter attached the pyramidal structure to the ground plane and were soldered in place. Note this is not a trivial task. The pins do, however, manage to provide sturdy support for the antenna arms. Figure 4.14 shows the fabricated model. It should be mentioned that the manufactured model resembles its intended simulation model much better than the conical sinuous antenna did in [11].

4.2.2 Measurements

Measurements were made of the antenna's port parameters and its far-fields. Regarding the former, a two port vector network analyser (VNA) was used to determine its standard S-parameters. Two ports were connected to the VNA at a time while the remaining two ports were connected to 50 Ω loads. Various port combinations had to be made to obtain all the necessary data. After sorting the data appropriately, the mixed mode S-parameters were calculated according to (3.17).

The far-fields were measured at a spherical antenna test range. Two probes were required to cover the frequency range. A dual ridge horn antenna [35] was used for the $2-5$ GHz range while a rectangular open ended waveguide [36] was used for the $5-6$ GHz

(a) Model

(b) Reflection coefficient

(c) Aperture efficiency with $\theta_0 = 48°$
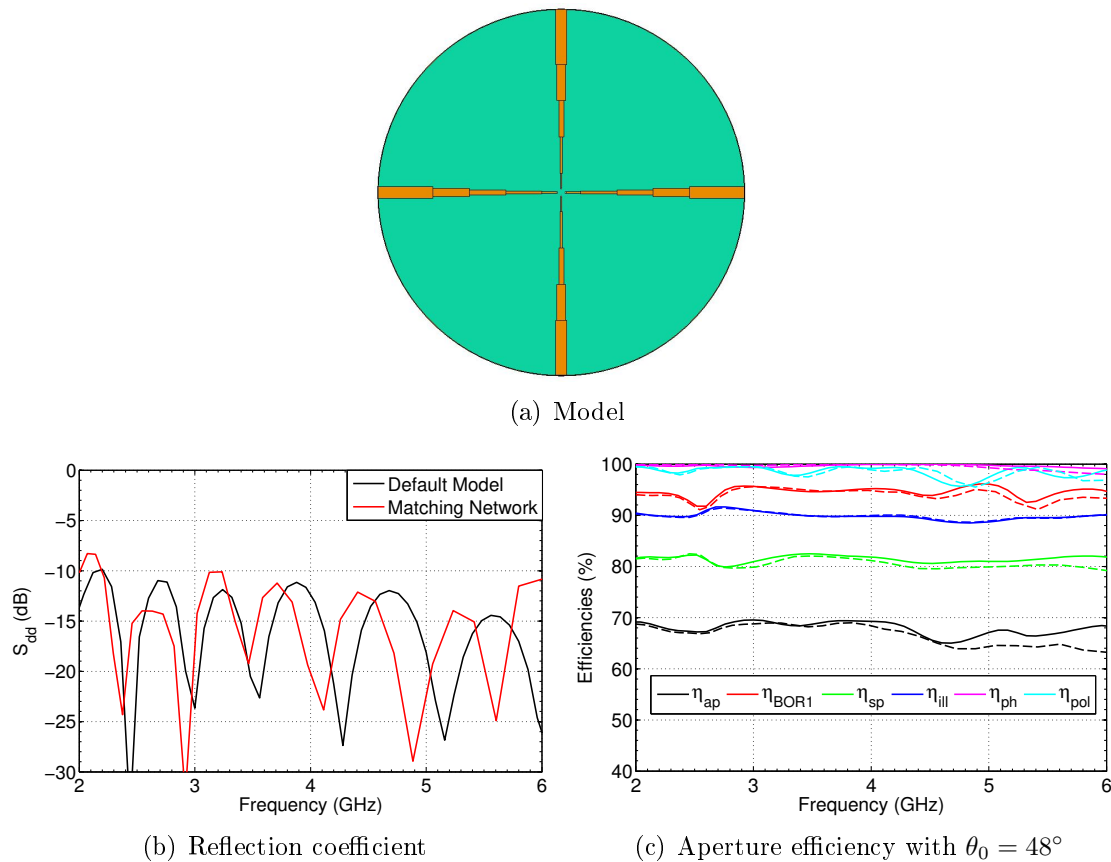
Figure 4.13: Performance of antenna with matching network, but no substrate on antenna arms.

frequency range. It was assumed, and later confirmed, that a negligible discontinuity occurs at the crossover frequency.

In order to measure a single linear polarization the following methodology was used. One port was excited while the other ports were connected to 50 Ω loads. Then, the antenna was measured. Afterwards, the antenna was reset to its original position and the opposite port was excited (with the remaining ports connected to 50 Ω loads). Then, the antenna was measured again. The setup is symbolically shown in Fig. 4.15.

With the measured field patterns for two opposite ports it is possible to calculate their differential and common mode field patterns according to [37]. This method is only applicable if there exists symmetry between the single ended ports. Due to linearity, the differential and common mode field patterns can be determined from

$$E_d(\theta, \phi) = \frac{1}{\sqrt{2}}(E_1(\theta, \phi) - E_3(\theta, \phi)) \tag{4.7a}$$

$$E_c(\theta, \phi) = \frac{1}{\sqrt{2}}(E_1(\theta, \phi) + E_3(\theta, \phi)) \tag{4.7b}$$

where E_d is the differential mode field pattern, E_c is the common mode field pattern, E_1 is the field pattern obtained from the single ended excitation at one port and E_3 is the field pattern obtained from the opposite port. The $1/\sqrt{2}$ factor is to account for the transmission coefficient of an ideal power combiner. Essentially (4.7) is the application of an ideal 3 dB 180° hybrid coupler. Since the models were differentially excited, only the differential mode field pattern is required for single linear polarization.

(a) Top

(b) Bottom

(c) Side

(d) Isometric
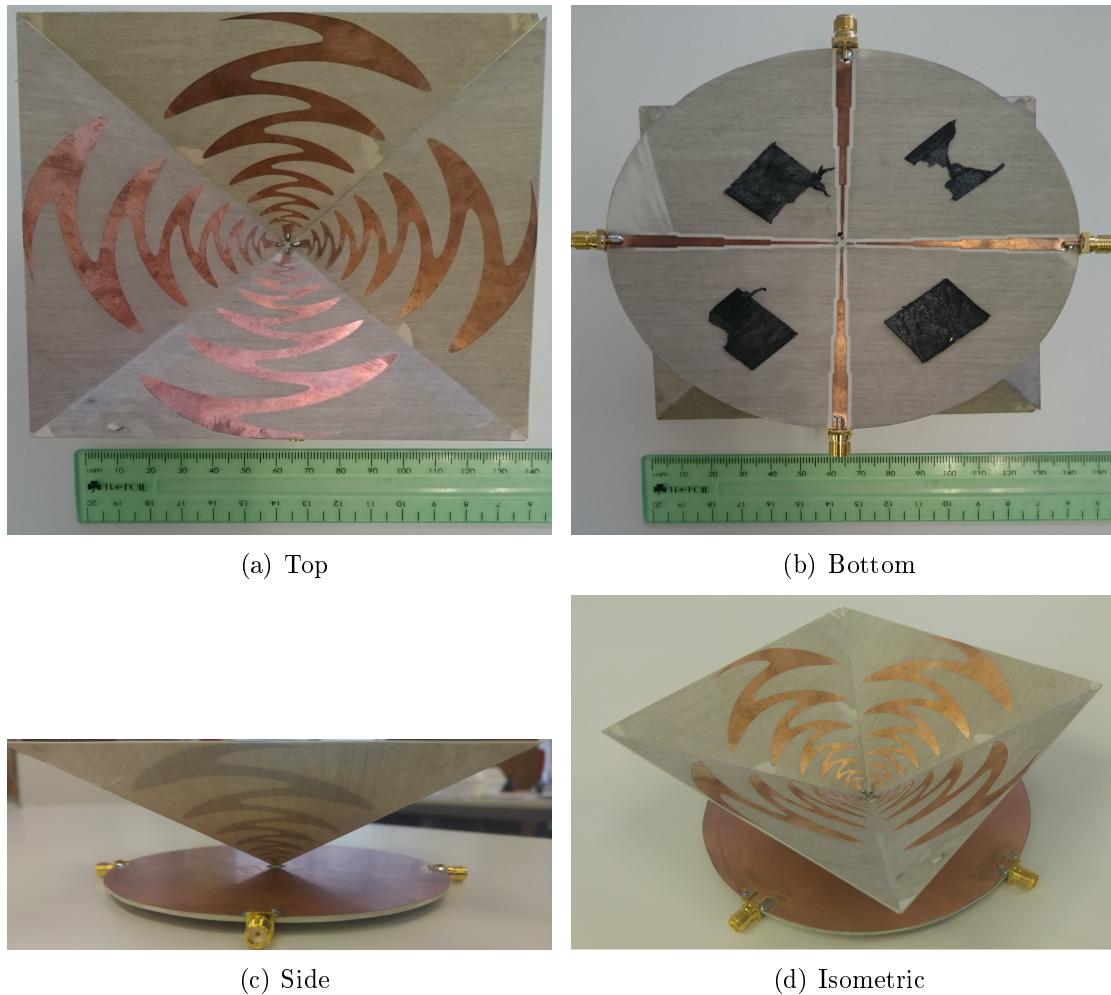
Figure 4.14: Manufactured antenna

4.3   Results and Comparison

After acquiring the measured data and appropriately manipulating it to the correct form, the manufactured model's performance can be presented. It will be compared to an equivalent model's performance to determine how accurate the simulation was. Also, it will be compared to a conical sinuous antenna's performance in order to highlight the advantage of the pyramidal sinuous antenna.

4.3.1   Simulation Comparison

To start the observations, the normalized co-polar and cross-polar radiation patterns in the E-plane are shown in Fig. 4.16. Though the two are fairly similar, the manufactured model's main beam is slightly narrower and stabler over the frequency range.

As was previously explained, aperture efficiency is depended on the feed's radiation fields as well as the reflector system's F/D ratio. Since the measured fields are now available, a quick investigation of the minimum aperture efficiency as a function of the F/D ratio was performed. The results are shown in Fig. 4.17. In the range $0.51 \leq F/D \leq 0.56$ (which corresponds to subtended angle range of $52° \geq \theta_0 \geq 48°$), the minimum aperture efficiency obtained is in the region of $62\% - 63\%$ for the simulated model and $60\% - 61\%$ for the manufactured model.
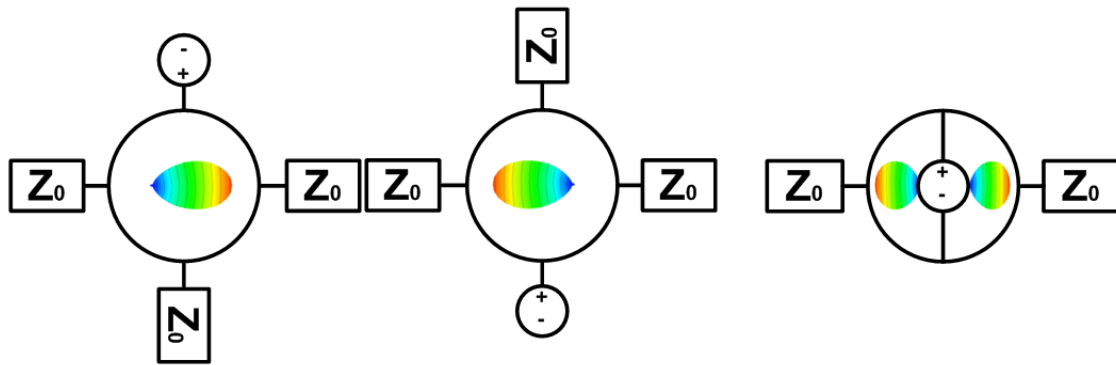
Figure 4.15: Two measured field patterns (left) can be used to calculate the differential field pattern (right)

(a) Simulation   (b) Measured
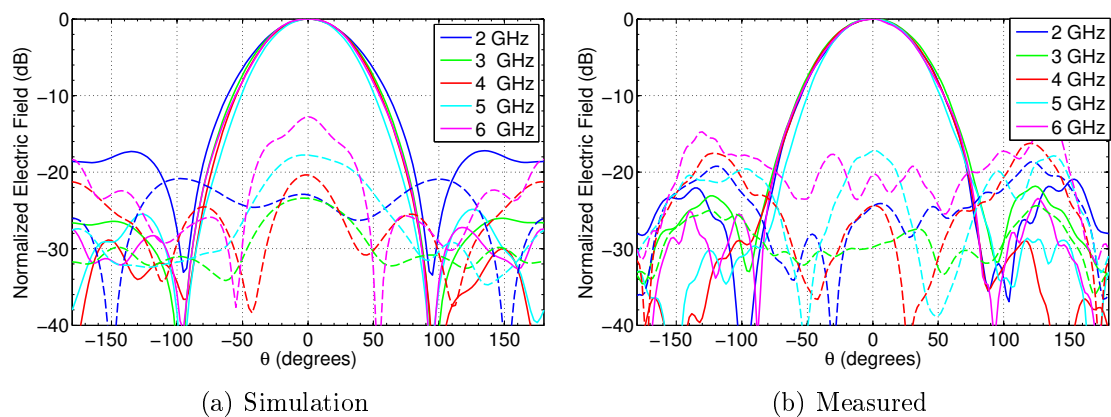
Figure 4.16: Co-polar and cross-polar radiation patterns in the E-plane
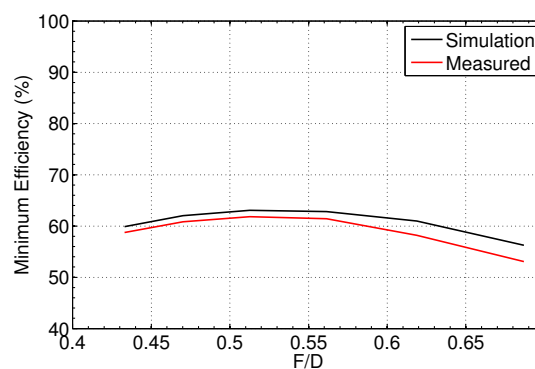
Figure 4.17: Minimum η_{ap} for different subtended angles in a reflector system

For comparison purposes a F/D ratio of 0.56 will be used. The aperture efficiency as well as the subefficiencies are shown in Fig. 4.18. Solid lines refer to the simulated model while dashed lines indicate the manufactured model's performance. It can be seen that the two performances do indeed closely correlate with each other.

Next, shown in Fig 4.19, are the differential reflection coefficients. While the two graphs are not exactly similar, there is a correlation between them. As expected, the simulation model's results are shifted to right relative to the manufactured model's results. Both have a maximum reflection coefficient of -8 dB, though they occur at different
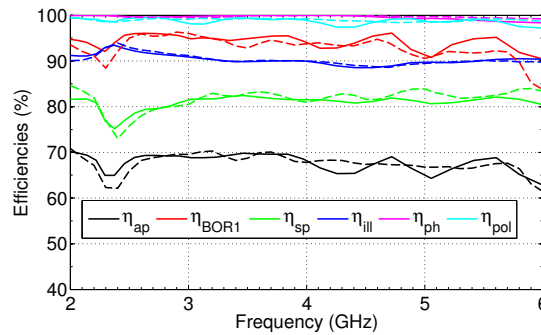
Figure 4.18: Efficiencies in a reflector system with $\theta_0 = 48°$. Solid lines represent the simulated model and dashed lines represent the manufactured model.

frequencies. Both also remain below -10 dB over almost all of the spectrum.
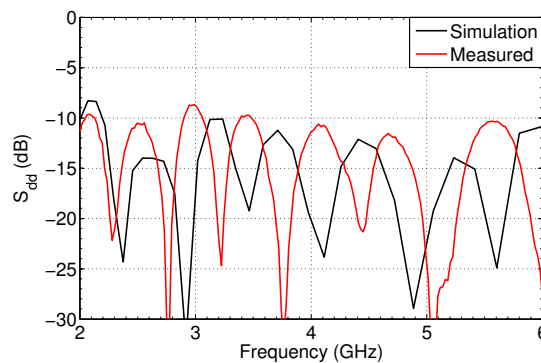
Figure 4.19: Reflection coefficients of manufactured and simulated models

4.3.2   Conical Sinuous Antenna Comparison

A conical sinuous antenna and pyramidal sinuous antenna with the same parameters' performance are shown next. In Fig. 4.20 the two models' aperture efficiency are compared. Only the theoretical aperture efficiency of the conical sinuous antenna is illustrated, but it seems to be very similar to the pyramidal sinuous antenna's results.

The true difference is noticed when comparing their differential reflection coefficients. It is shown in Fig. 4.21. Though the conical sinuous antenna's theoretical performance is superior to the pyramidal sinuous antenna's performance (since it was optimized), it is a different case for the practical performance. While the latter's result hovers around -10 dB, the former's result skirts around -5 dB. This highlights the advantage of the pyramidal sinuous antenna. Due to a more robust manufacturing process, it is more capable to perform akin to its simulated model than a conical structure would.

Figure 4.20: Aperture effieciency of the pyramidal and conical sinuous antennas with $\theta_0 = 48°$. Solid lines represent the simulated model and dashed lines represent the manufactured model.
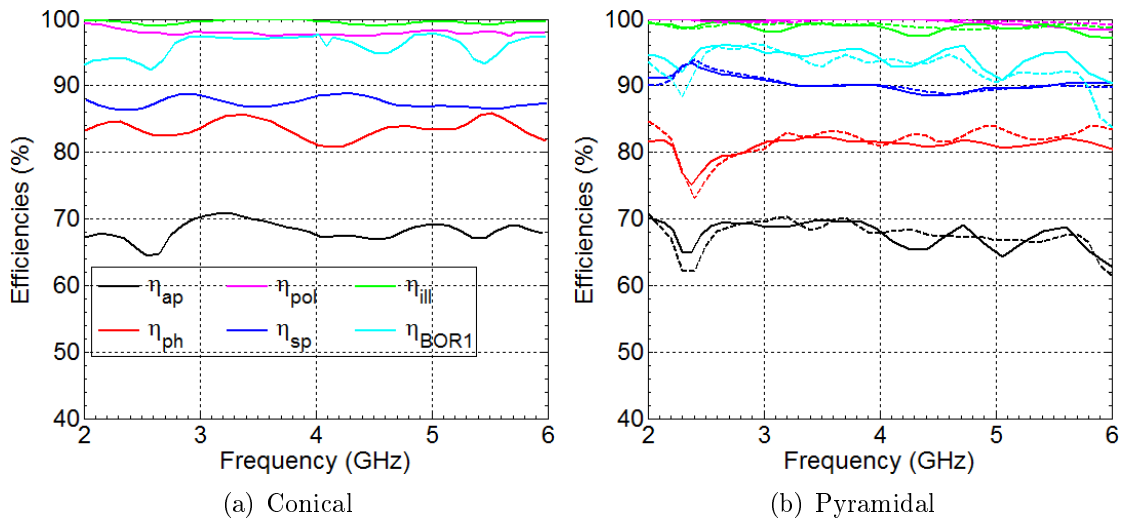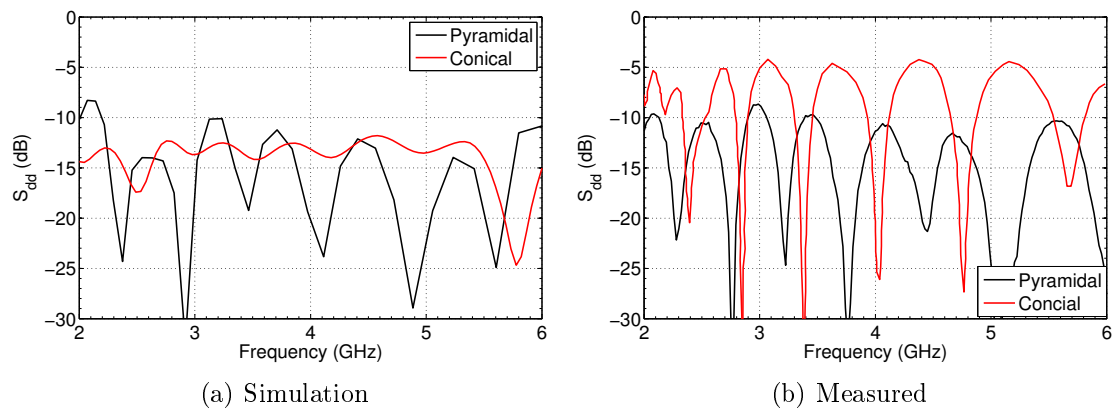

Figure 4.21: Reflection coeffiecients of the pyramidal and conical sinuous antennas

Chapter 5

Ultra Wideband Pyramidal Sinuous Antenna

Since the results of a 3:1 bandwidth pyramidal sinuous antenna confirmed it was feasible, it was decided to realise a 10:1 version. For the SKA a reflector feed with decent performance over an ultra wide bandwidth would drastically reduce the number of required feeds. Such a feed could potentially lead to huge cost savings. Added to this, it was assumed the process would be straightforward since much of the groundwork was already laid in the previous chapter. Early on, however, it became apparent this would not be the case.

In the preceding chapter the modelling, manufacturing and measuring of a pyramidal sinuous antenna was discussed in detail. In this chapter the modelling, manufacturing and measuring of a 10:1 version will be presented. It is intended to serve as an extension to the previous work, implicitly applying the processes described in that chapter while adding new ideas and further insights.

During the design process, fresh challenges arose while old ones exacerbated. Some were overcome, but others were not. These challenges relate to the long simulation time, feeding scheme and construction of an ultra wideband pyramidal sinuous antenna. Therefore, this chapter is focussed on how they were addressed. Details will be given about a new simulation approach, the problem of the pins passing through the substrate, and the difficulties with the construction. At the end, the measured results will be presented and discussed. An explanation on the difference between the measured and simulated performances will also be given.

5.1   Modelling

To start, a basic 10:1 pyramidal sinuous antenna model was simulated in order to affirm its potential as a wideband feed. The simulation considerations (mesh, input impedance, and so forth) of the model mimics those in the previous chapter. Also, the model shares the same design parameters as its predecessor, apart from the start and end frequencies. Initially, they were chosen as 1 GHz and 10 GHz, respectively. The design parameters are provided in the Table 5.1 and the model is shown in Fig. 5.1(a).

As seen in Fig. 5.1, the performance is promising. The reflection coefficient, shown in Fig. 5.1(b) is mainly below -10 dB over the frequency range, rising at the end to reach a maximum of -9.5 dB. Meanwhile, Fig. 5.1(c) shows the aperture efficiency to hover around 70% with dips near the start and end of the spectrum reaching a minimum of 66%.

Table 5.1: Design parameters of a 10:1 pyramidal sinuous antenna

Parameter	Value
α	24.85°
δ	14.95°
τ	0.842
θ	56.48°
f_{min}	1 GHz
f_{max}	10 GHz
h	5 mm
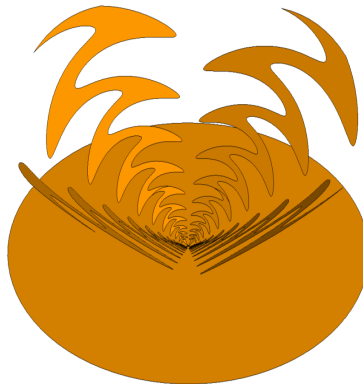
(a) Default 10:1 model
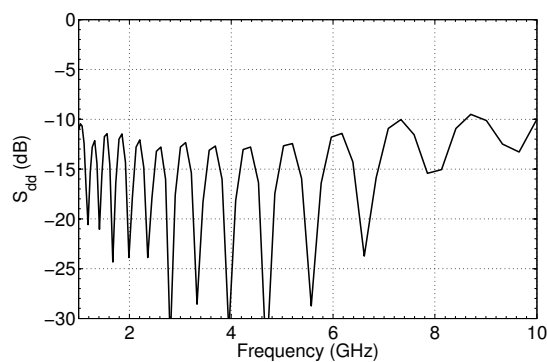
(b) Reflection Coefficient
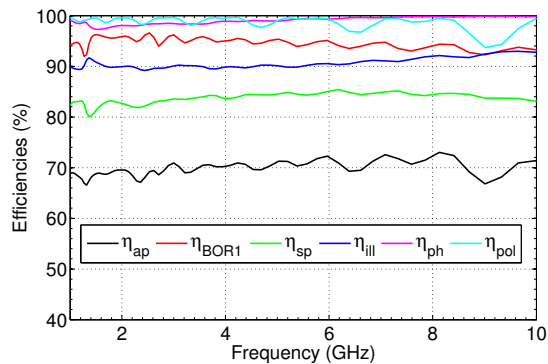
(c) Aperture efficiency with $\theta_0 = 48°$

Figure 5.1: Performance of 10:1 bandwidth pyramidal sinuous antenna

A notable trait of the model is its extremely long simulation time. Due to its wide bandwidth, the model requires a large number of mesh cells to segment it and many frequency points to sample it at. If further models were to be simulated, a new approach would be required. The one used is described next.

5.1.1 Simulation Procedure

Consider the ideal performance of the antenna as shown in Fig. 5.2(a). It acts as a bandpass filter with rapid degradation occurring around the band edges. The core idea of the new approach is to avoid simulating where the antenna is expected to perform well. Due to the quasi log-periodic nature of the antenna, it is assumed the performance between the band edges is equal or better than the performance at the band edges. Therefore,

only the performance at the band edges need to be simulated. This is illustrated in Fig. 5.2(b). The information that is lost is traded for a faster simulation time.

(a) Normal simulation   (b) New simulation
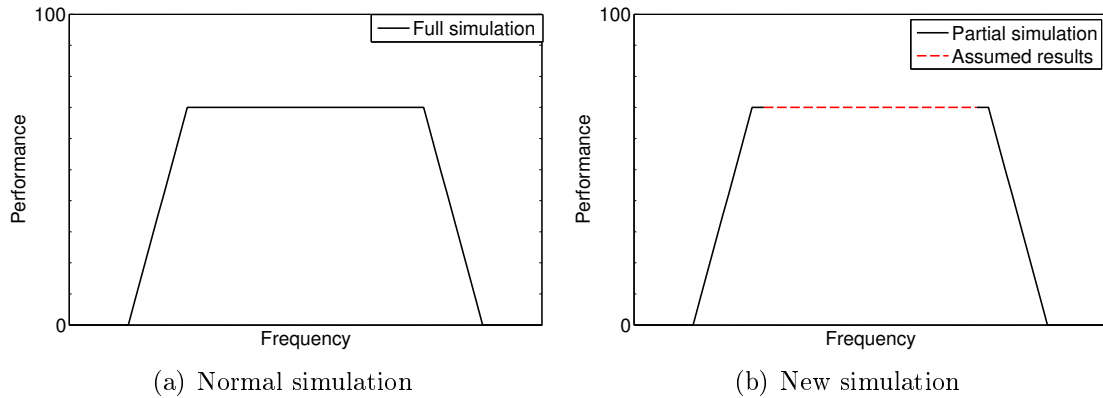
Figure 5.2: Different simulation procedures.

Only simulating at the band edge frequencies already assists this approach as it reduces the number of sampling points. In addition, it was observed simulating models designed for the band edges instead of the entire spectrum can drastically reduce the number of mesh elements while providing accurate results. The reason this is possible, it is assumed, is due to the periodic nature of the antenna and the resemblance the band edge models share with the full model. At a certain frequency only a specific part of the antenna is being used. It seems if only that specific part is simulated, then the same results will be obtained as if simulating the entire antenna at that frequency. An example is used to explain this.

In Fig. 5.3(b) a model designed for $2 - 6$ GHz is shown. Its performance is displayed as the black lines in Fig. 5.3(d) and Fig. 5.3(e). Analogous to this, a band edge model designed for the lower frequencies and a band edge model designed for the higher frequencies are shown in Fig. 5.3(a) and Fig. 5.3(c), respectively. Their performances are displayed as the green lines in Fig. 5.3(d) and Fig. 5.3(e).

It is clearly seen that the full model and the band edge models' performances overlap to a sufficient degree. The low frequency band edge model's reflection coefficient is marginally shifted to the right of the full model's while their aperture efficiencies are in very good agreement. Contrarily, the high frequency band edge model's reflection coefficient is similar to the full model's while its aperture efficiency is equal or less than the full model's. In further observations it became apparent that a high frequency band edge model's aperture efficiency was generally a few percentage points lower than the full model's. It is something to keep in mind when using this method.

Both band edge models use less mesh elements than the full model. For the low frequency band edge model, since it is being simulated at lower frequencies, this is achieved by using markedly larger, though electrically still small, mesh elements to segment it. In the case of the high frequency band edge model, though it still uses extremely small mesh elements, a sizeable portion of the antenna has been cut away. Together with fewer frequency sampling points, the simulation time is drastically quicker than before.

Obviously, there exists a few caveats to this method. Firstly, though the band edge models are designed to operate over a smaller frequency range than the full model, they still require a sufficient number of active regions to accurately replicate the full antenna's performance. To explain this concept better, consider the following crude example. A full

(a) Low frequency band edge model

(b) Full model

(c) High frequency band edge model

(d) Reflection Coefficient

(e) Aperture efficiency with $\theta_0 = 48°$
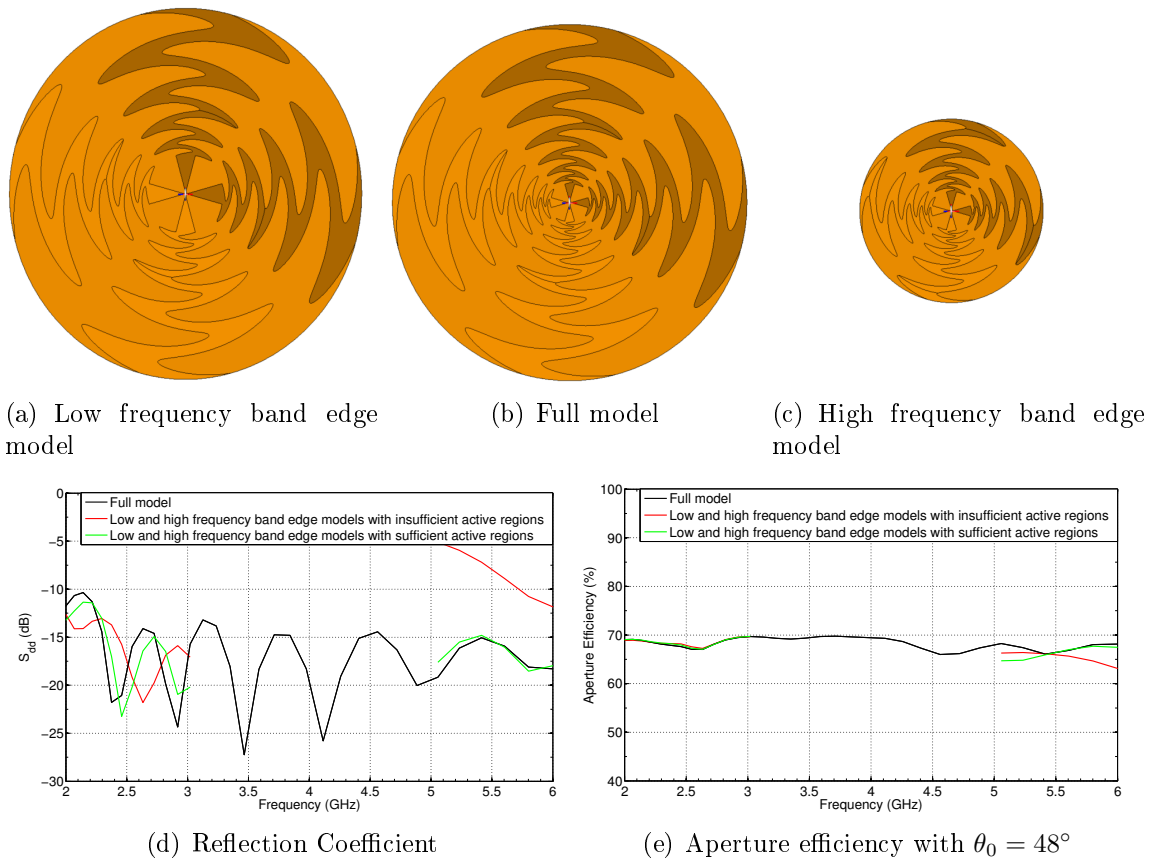
Figure 5.3: A full model (black) is compared to a pair of band edge models. In the graphs it is first compared to band edge models with an insufficient number of active regions (red); then it is compared to a pair of band edge models with a sufficient number of active regions (green)

model has ten active regions per arm and a 10:1 bandwidth. Meanwhile, its low frequency band edge model only has five active regions and a 5:1 bandwidth. The full model and the band edge model's performance then only mimic each other over a 2:1 section of the full model's bandwidth. If the band edge model instead only had 2 active regions and a 2:1 bandwidth, its performance would not resemble the full model's performance in any way.

A band edge model having too few active regions leads to inaccuracies between its performance and the full model's performance. In Fig. 5.3(d) and Fig. 5.3(e) the red lines represent such band edge models. The low frequency band edge model's reflection coefficient differs from the full model's, but its aperture efficiency is still similar to the full model's. The high frequency band edge model's reflection coefficient and its aperture efficiency are, instead, noticeably different from the full model's. How to determine the optimal number of active regions was not investigated. A sufficient number was determined experimentally in each case.

Secondly, it is critically important that the band edge models physically resemble the full model where their active regions overlap. They are the same as the full model apart from active regions missing in the centre / at the outer edge. They are not scaled or translated versions of the full model. If the band edge models geometrically differ from the full model, they are simulating different cases.

This simulation method was applied on a 10:1 pyramidal sinuous antenna to affirm its accuracy. The low frequency band edge model had enough active regions to cover

the frequency range $1 - 3$ GHz while the high frequency band edge model had enough to cover $4 - 10$ GHz. Their results are shown in Fig. 5.4. In Fig. 5.4(a) it is seen that the reflection coefficient is accurately simulated over most of the spectrum. Slight differences start to occur at the ends of the band edge model's designed frequency ranges – at the higher frequencies for the low frequency band edge model, and at the lower frequencies for the high frequency band edge model. Since these edge effects of the band edge models do not resemble the full model's performance, they can be ignored. In Fig. 5.4(b) the aperture efficiency is shown with the band edge models represented by the dashed lines and the full model by the solid lines. While the low frequency band edge model is in very good agreement to the full model, the high frequency band edge model is not. It follows the behaviour of the full model, but is translated lower (mainly due to η_{sp} and η_{ill}). The difference in their results varies between $4\% - 10\%$ over the spectrum.

(a) Reflection Coefficient

(b) Aperture efficiency with $\theta_0 = 48°$
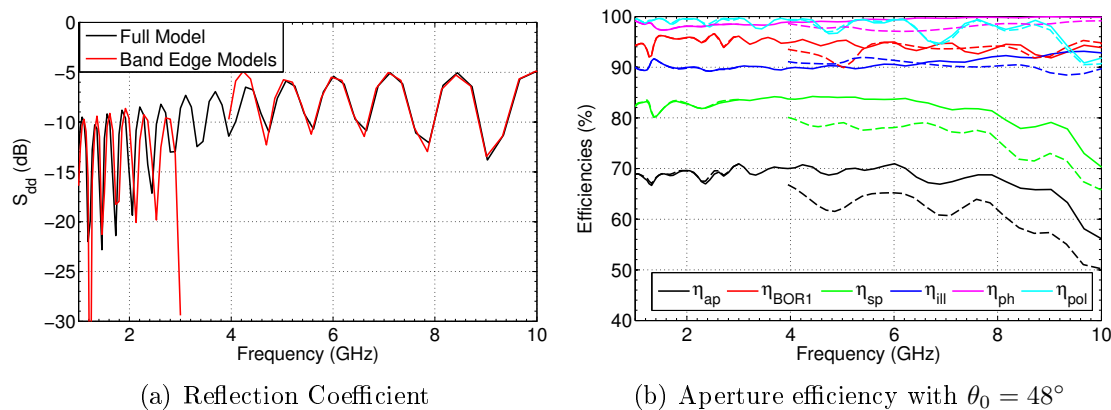
Figure 5.4: Comparison of full model (solid lines) designed for a 10:1 bandwidth and its corresponding band edge models (dashed lines).

Once again, the huge improvement to simulation time is duly noted. The trade of missing information for faster simulation times was considered worthwhile. Although the aperture efficiency at higher frequencies is imprecise, it can still be used if the translation effect is taken into account. This method is used in all the following cases, albeit at fewer frequency points.

5.1.2   Feed Dilemma

As in the case of the previous design, the 10:1 pyramidal sinuous antenna needed to be fed. It was decided to use the same feeding scheme as last time as this had proven to be a simple and adequate solution. However, in the ensuing simulations it become apparent the same performance results would not be repeated. Feeding the antenna over such a wide bandwidth is a challenge in itself.

The reason for the difficulty is due to the pins passing through the substrate. As previously stated, a mismatch in impedance occurs between the pins in the free space and the pins in the substrate. At higher frequencies this mismatch is worsened. Figure 5.5 shows the performance of the antenna when pins are attached and pass through a substrate. In Fig. 5.5(b) the reflection coefficient can be seen reaching a maximum of -5 dB at the higher frequencies while remaining below -10 dB at the lower frequencies. In Fig. 5.5(c) the aperture efficiency is seen to remain the same at the lower frequencies, but performs

worse (even when accounting for the translation error of the band edge model) at the higher frequencies.
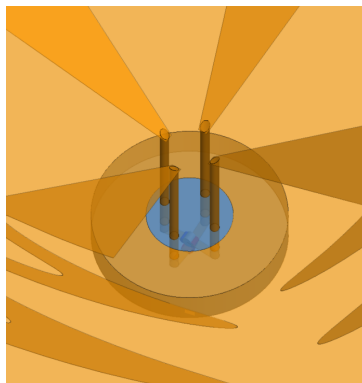
(a) Pins through substrate
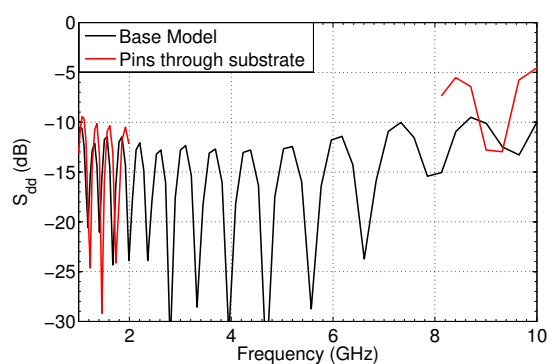
(b) Reflection Coefficient
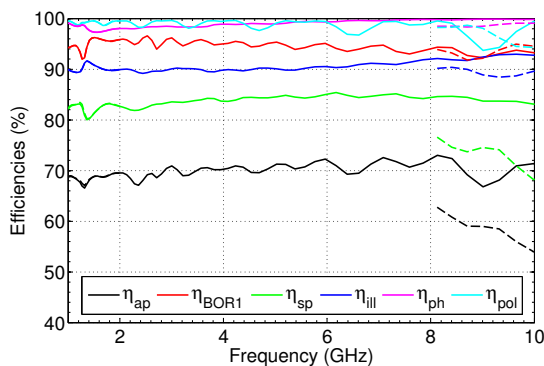
(c) Aperture efficiency with $\theta_0 = 48°$

Figure 5.5: The effect of pins passing through the substrate.

In order to alleviate the poor performance, a few different tweaks to the antenna were attempted. These include designing the antenna with slightly altered design parameters, shifting the height of the antenna above the ground plane, using substrates with a lower effective permittivity, cutting holes in the substrate to hopefully lessen its impedance, and, finally, removing the substrate around the pins altogether.

Only the last tweak provided worthwhile results. Its performance is seen in Fig. 5.6. When the pins are attached, but do not pass through the substrate, the same reflection coefficient as the base model can be obtained. This is seen in Fig. 5.6(b). Due to the high frequencies involved and the pins' electrically large lengths, an input impedance of 260 Ω is necessary. Figure 5.6(c) shows the aperture efficiency which performs slightly better than the previous model, but still worse than the base model.

Unfortunately, after consulting about its construction process, this feeding scheme was deemed impractical. From a mechanical standpoint, having the pins pass through the substrate provides them with rigid support. Removing that support would make a difficult assembly process even more so. Furthermore, it was discovered that the arms of the previous models were too large to be fabricated using the available etching machine. In order to manufacture an antenna, it would have to be designed for a higher starting frequency.

Therefore, after taking these aspects into consideration, it was decided to realise a best-as-possible 10:1 pyramidal sinuous antenna with its pins passing through a sub-
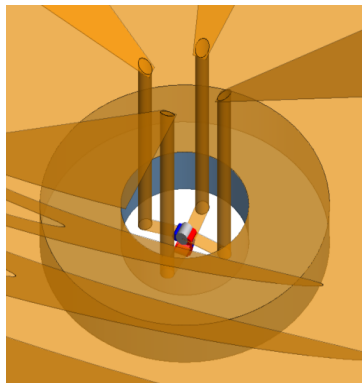
(a) Hole in substrate
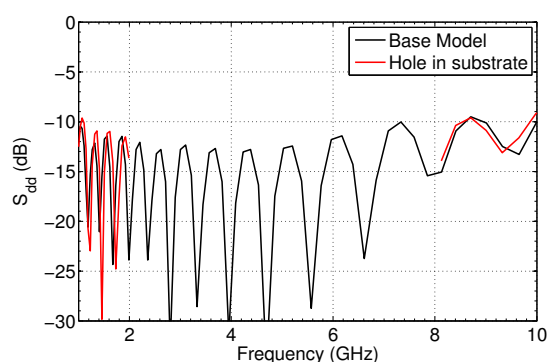
(b) Reflection Coefficient
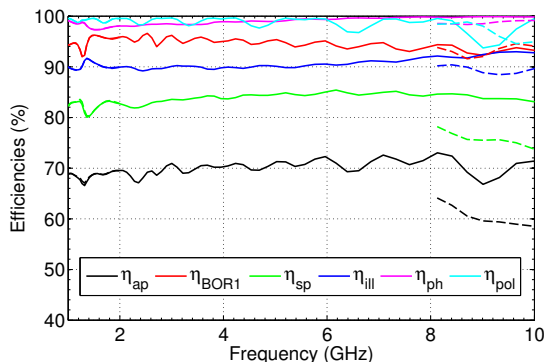
(c) Aperture efficiency with $\theta_0 = 48°$

Figure 5.6: The performance when the pins avoid passing through the substrate.

strate. In Table 5.2 the new design parameters are given. Operating over the frequency spectrum $1.2 - 12$ GHz allowed the antenna to be small enough to fit inside the etching machine, while having a lower height above the ground plane was seen to slightly lessen the maximum reflection coefficient. Also, the ground plane uses a different substrate with $\epsilon_r = 2.94$ and the input impedance of each of the four ports is 100 Ω.

Table 5.2: Design parameters of a 10:1 pyramidal sinuous antenna

Parameter	Value
α	24.85°
δ	14.95°
τ	0.842
θ	56.48°
f_{min}	1.2 GHz
f_{max}	12 GHz
h	1 mm

The model and its performance is shown in Fig. 5.7(a). Its results are poor, unfortunately, with the reflection coefficient reaching a maximum of -6 dB and the aperture efficiency a minimum of 51%. This model's S-parameters were exported into Microwave Office to design a matching network. No model was simulated with substrates on the antenna arms since, besides inflating the number of mesh elements and increasing the simulation duration, it was assumed at the time to only shift the results.

(a) Model

(b) Reflection Coefficient

(c) Aperture efficiency with $\theta_0 = 48°$
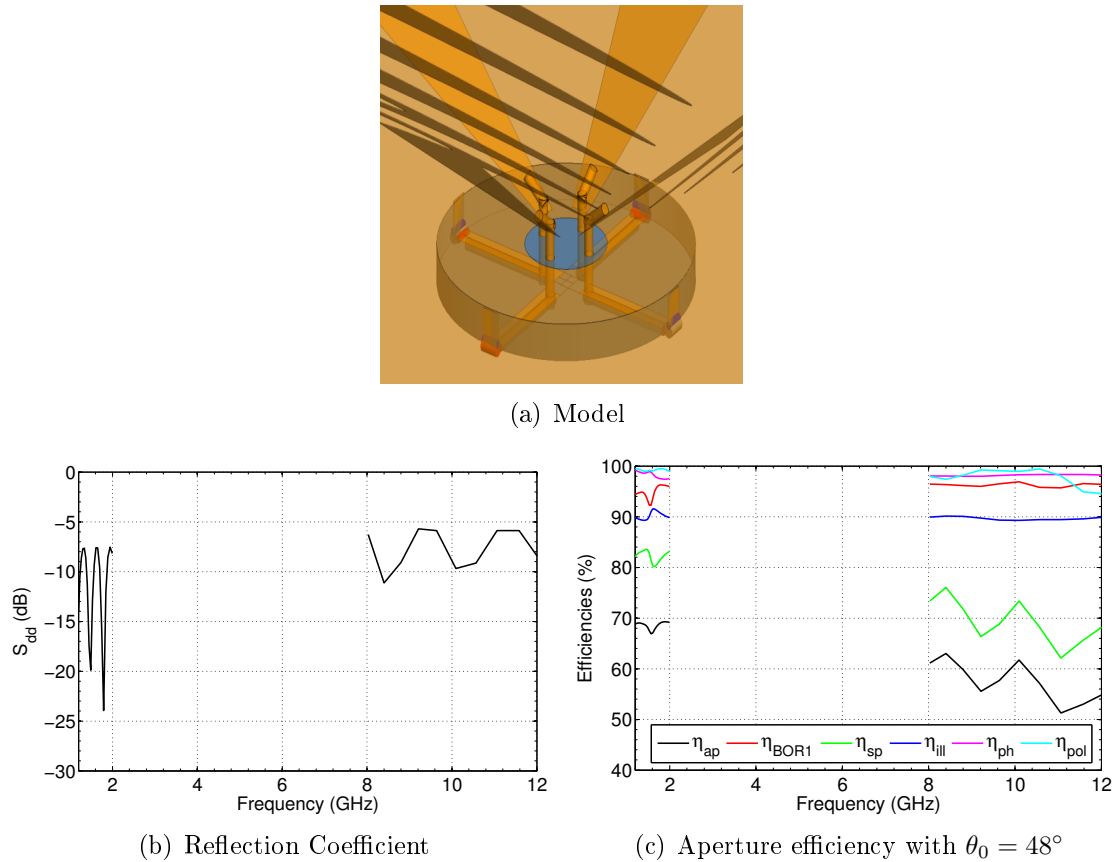
Figure 5.7: Performance of 10:1 bandwidth pyramidal sinuous antenna designed for $1.2 - 12$ GHz.

A consequence of the simulation procedure used thus far is that a stepped impedance matching network cannot be optimized for the entire frequency spectrum. Therefore, it was decided to use a Chebyshev matching network that would at least minimize S_{11} and S_{33} over the frequency range. In order to cover the wide bandwidth, a 12th order Chebyshev microstrip line was designed according to [38] and attached to each port. The width and length of each section is provided in Table 5.3 and a schematic of the matching network is shown in Fig. 5.8(a). This circuit was connected to each port. The differential reflection coefficient of the entire antenna is shown in Fig. 5.8(b). It reaches a maximum of -7 dB. Alongside the design parameters in Table 5.2, these are the model parameters used for manufacturing the antenna.

5.2 Construction and Measurement

The antenna arms and the matching networks were etched onto dielectric substrates with $\epsilon_r = 3.38$ and $\epsilon_r = 2.94$, respectively. Note that the former has a height of 0.508 mm and the latter 1.524 mm. Holes were drilled in them for the pins. The arms were once again connected using sticky tape. To help support the arms, foam blocks were cut out and planted between them and the ground plane. Lastly, the 0.5 mm diameter pins were threaded through the holes and soldered in place. Care should be taken with the final step. As seen in Fig. 5.9, due to the difficulty involved the feed area was slightly damaged. The fully constructed model is shown in Fig. 5.10.

Table 5.3: Values for twelfth order Chebyshev impedance transformer

Parameter	Value
w_1	0.7 mm
w_2	0.8 mm
w_3	0.9 mm
w_4	1.1 mm
w_5	1.3 mm
w_6	1.6 mm
w_7	1.9 mm
w_8	2.3 mm
w_9	2.6 mm
w_{10}	2.8 mm
w_{11}	3 mm
w_{12}	3.3 mm
length	3.1 mm
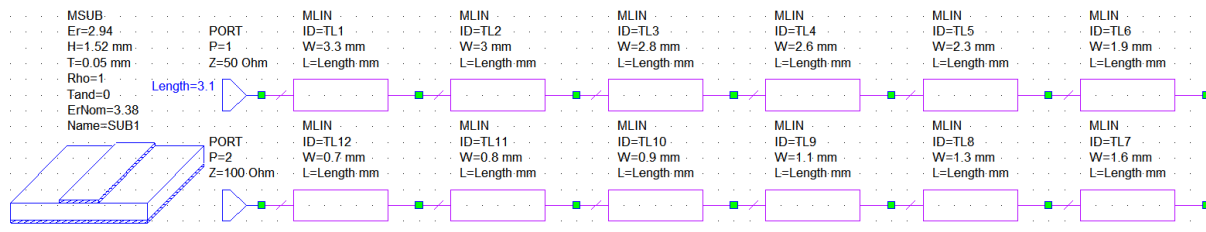
(a) Schematic
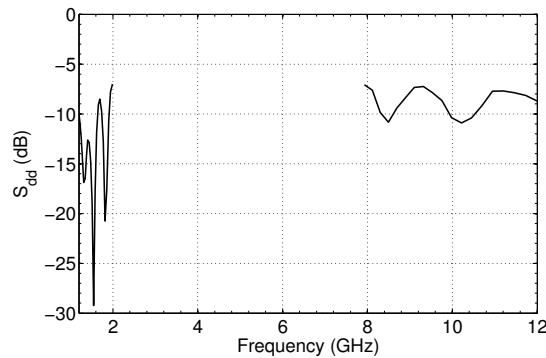
(b) Reflection coefficient

Figure 5.8: Schematic of matching network and differential reflection coefficient

Measuring the antenna was straightforward. The reflection coefficients and far-fields were obtained using a VNA and the spherical test range as previously explained. To acquire the latter over such a wide bandwidth, each port was measured over three bands using the test range's measuring probes. A dual ridge horn antenna was used as receiving feed for the $2 - 5.2$ GHz range, a rectangular open ended waveguide used for the $5.2 - 8.2$ GHz range and another rectangular open ended waveguide used for the final $8.2 - 12$ GHz range. Afterwards, the data was manipulated to the desired format and studied.

Figure 5.9: Closer look at the antenna's feed area
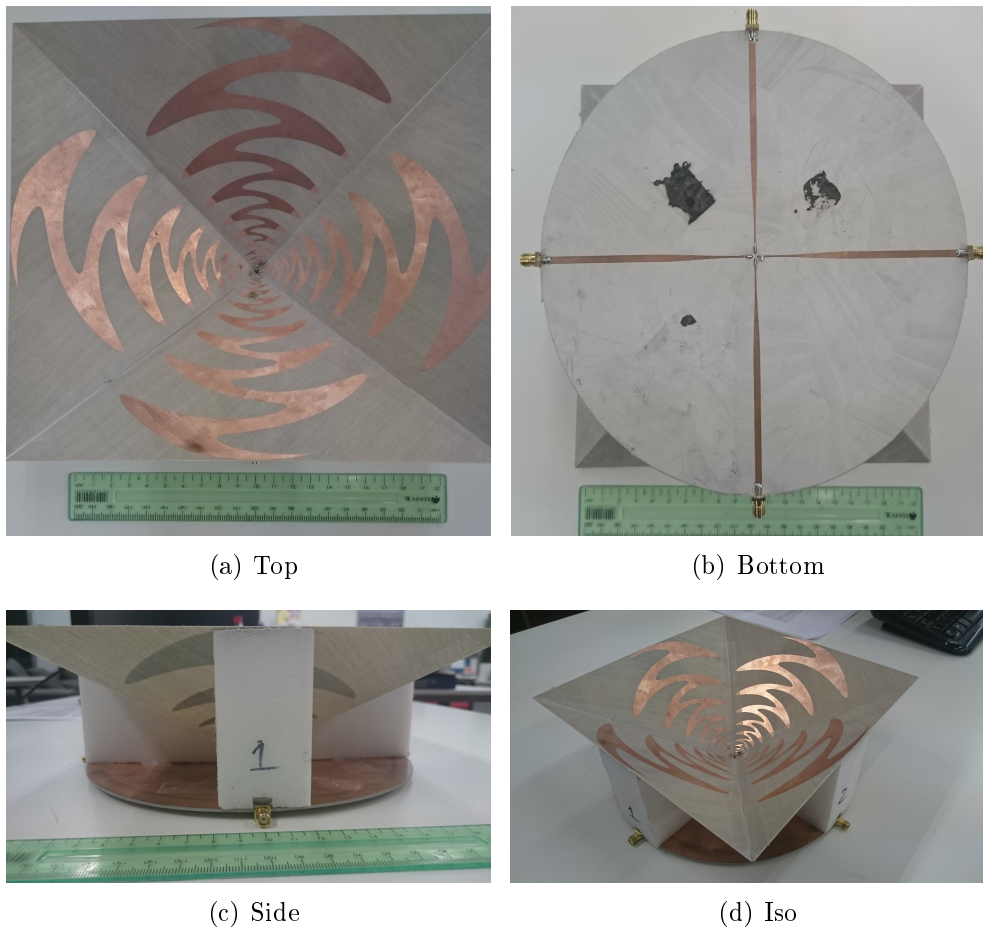
(a) Top

(b) Bottom

(c) Side

(d) Iso

Figure 5.10: Manufactured antenna

5.3   Results and comparison

The measured performance, unfortunately, did not match the simulated performance. Reasons for this will be discussed after the results are presented.

In Fig. 5.11 the aperture efficiency is given. Solid lines refer to the simulated results and dashed lines represent the measured results. Over the bandwidth, the measured aperture efficiency is seen to drastically decline as frequency increases, reaching a minimum of 20%. The main reason is due to the poor performance of ϵ_{BOR1}. This suggests severe

asymmetry in the far-fields. As shown in 5.12, this is indeed the case with the farfields becoming noticeably more asymmetric as the frequency increases.
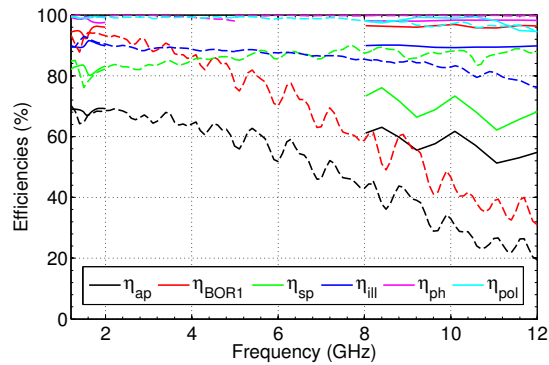
Figure 5.11: Efficiencies in a reflector system with $\theta_0 = 48°$. Solid lines indicate the simulated results; dashed lines indicate the measured results.

(a) 2 GHz

(b) 5 GHz

(c) 8 GHz

(d) 11 GHz
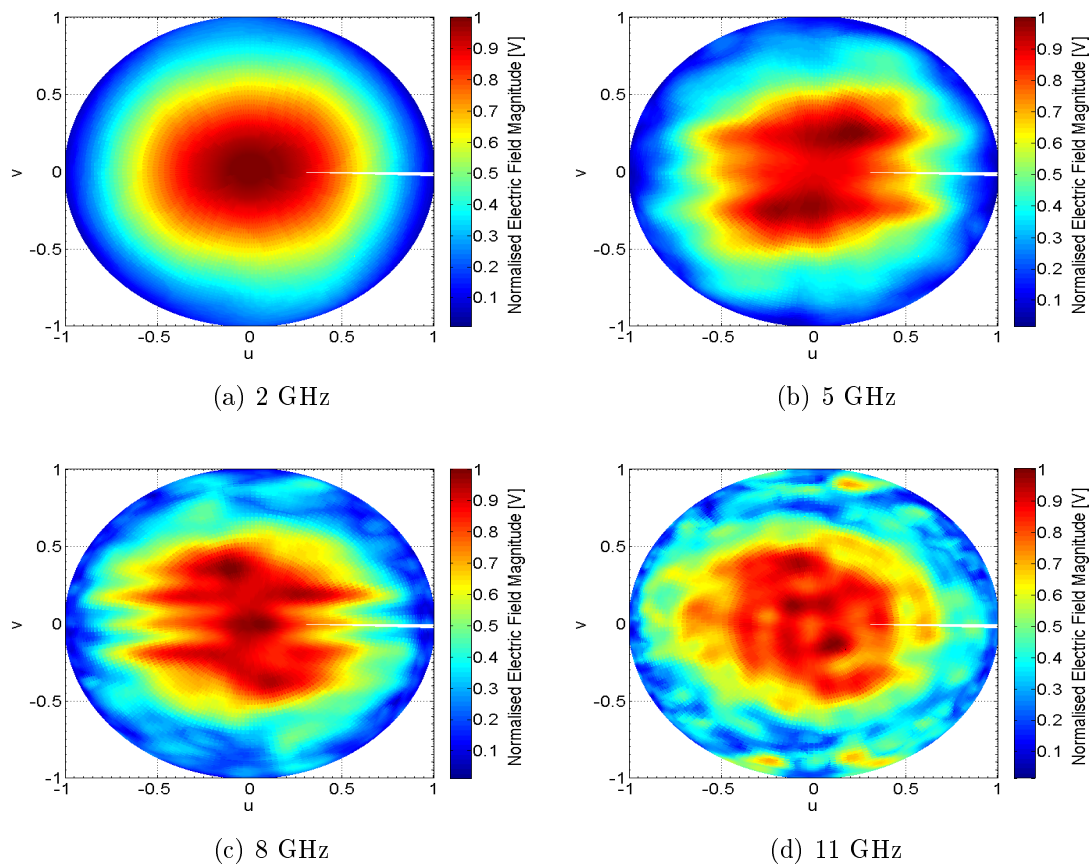
Figure 5.12: Far-fields radiation patterns at different frequencies

The reflection coefficient is shown in Fig. 5.13. Although the measured results are shifted, they are also higher than was expected.

While the antenna certainly does not perform well over a 10:1 bandwidth, it does perform reasonably decent over the lower frequencies. Looking over the $1.2 - 6$ GHz range, it can be seen the aperture efficiency is mostly above 60%, reaching a minimum of
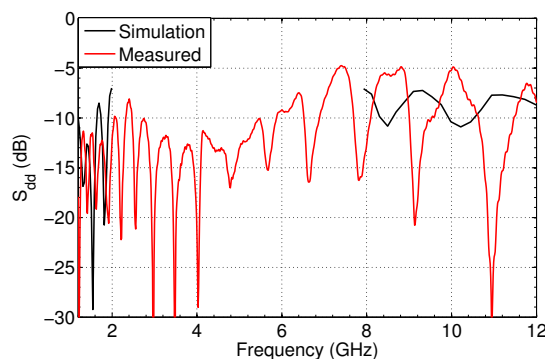
Figure 5.13: Reflection coefficients of built and simulated models

52% at the end. Similarly, the differential reflection coefficient is mostly below -10 dB across this range with a jump at 2.4 GHz to reach a maximum of -8 dB. The measured antenna can be thought as having a 5:1 bandwidth.

5.4   Performance Mismatch Explanation

Reasons for the fabricated antenna's unexpectedly poor performance was investigated. Initially, it was thought that the construction process was to blame. As shown in Fig. 5.9, asymmetry occurred in the feed area which could possibly explain the asymmetry in the far-fields. However, after incorporating the physical defects into the simulation model, the performance did not drastically deteriorate.

Upon further researching literature a possible reason was discovered. It seems the eleven feed encountered a similar problem. Briefly mentioned in Chapter 1 and shown in Fig. 1.2, the eleven feed is another reflector dish candidate for the SKA. It shares various similarities to the conical and pyramidal sinuous antennas such as log-periodic radiating areas and reflecting ground planes.

In [9], the eleven feed also encountered poorer performance at high frequencies due to ϵ_{BOR1}. It was speculated at the time that surface waves occur in its petals' dielectric substrate. These waves seemed to be excited at its feed area. During the simulations of the ultra wideband pyramidal sinuous antenna, modelling the dielectric substrate for the antenna arms were ignored for two reasons. Firstly, it improves the simulation time and the mesh's size. Secondly, during the $2-6$ GHz pyramidal sinuous antenna's simulations, omission of the substrate on the arms did not significantly alter the performance. It was assumed the same would be applicable for the 10:1 bandwidth case. In hindsight this was erroneous. When considering a dielectric substrate, it is important to remember that although its physical thickness is typically constant, its electrical thickness can change dramatically as a function of frequency.

In order to compensate for the non log-periodic substrate thickness of the eleven feed's petals, a scaling factor was introduced [39]. Each folded dipole's size (equivalent to an active region) was scaled down in accordance to a linear scaling factor applied to each dipole's length. The scaling factor was determined for each folded dipole using an equation as well as conducting a parameter study on the equation.

Unfortunately, due to time constraints this method could not be investigated for the pyramidal sinuous antenna. It should be investigated in future research.

Chapter 6

Performance on a Square Kilometre Array dish

Thus far the focus has mainly been on a pyramidal sinuous antenna. A 3:1 bandwidth version has been described in terms of reflection coefficient and aperture efficiency, and has proven to be manufacturable. However, only one version of the antenna has been evaluated. It is almost certain that a different geometry could provide improved performance. Therefore, the focus of this chapter is to determine the best possible performance the pyramidal sinuous antenna is capable of achieving. Specifically, it is the performance the antenna can achieve as a reflector feed for an SKA dish over Band 1 ($350-1050$ MHz).

It should be noted that in engineering there rarely exists a "best solution"; rather there tends to exist a "better solution" for a given situation. A design often has multiple requirements, and improving the performance for one requirement may decrease the performance for the rest. In order to evaluate the pyramidal sinuous antenna's capabilities, a straightforward parameter study was conducted on it. The performance metrics that were measured were its differential reflection coefficient and sensitivity.

Regarding the latter, it is one of the main design requirements of an SKA dish. This chapter starts by explaining what it is and how to calculate it. Then, a short description on how the parameter study was conducted is given. Lastly, the results are presented.

6.1   Sensitivity

Stated simply, the sensitivity of an antenna is a measure of the minimum detectable signal it is capable of receiving. Since radio astronomy sources are light years away, the receiving signals are especially faint. In order to detect them, the SKA dishes' sensitivity should be as high as possible. In the simplest form, it is given as[*]

$$\text{Sensitivity} = \frac{A_e}{T_{sys}} \tag{6.1}$$

where A_e is the effective aperture area of the antenna and T_{sys} is the system noise temperature.

The effective aperture area was explained in Chapter 2 as simply the product of an antenna's aperture efficiency and its physical aperture area. A thorough description was given to calculate the former, while the latter is an area calculation.

---

[*]For communication applications it is given as Sensitivity $= \text{Gain}/T_{sys}$

Regarding the denominator of (6.1), the system noise temperature quantifies the power residing in the noise that the entire system produces. It is dependent on all the stages in the receiving chain, but in general the antenna and the subsequent stage are the main contributors [40]. Therefore, the system temperature can be simplified as

$$T_{sys} = T_A + T_{rec} \tag{6.2}$$

where T_A is the antenna noise temperature and T_{rec} is the receiver noise. It is imperative for high sensitivity that the receiver noise should be low. Consequently, research for the SKA also involves cryogenic cooling methods for the receivers. This is outside of the scope of this thesis and it will be assumed to be a fixed value of $T_{rec} = 20$ K.

Antenna noise temperature is a measure of the power in the noise the antenna produces on its own. The less noise power it produces, the lower the minimum signal power can be in order to be detected. It is an intensive calculation, though a method to solve it faster specifically for offset Gregorian reflector systems is presented in [41] and summarised here.

Antenna Noise Temperature General Formulation

In general, the antenna noise temperature is defined [40] as a combination of the surrounding environment's brightness temperature as seen by the antenna, and the thermal noise generated by the antenna itself. It can be calculated as a function of frequency and the direction the antenna is pointing towards as

$$T_A(f|\hat{\mathbf{r}}_0) = \frac{\iint_{4\pi} N(f,\theta,\phi|\hat{\mathbf{r}}_0)\sin\theta d\theta d\phi}{\iint_{4\pi} P(f,\theta,\phi)\sin\theta d\theta d\phi}. \tag{6.3}$$

The antenna power radiation pattern $P(f,\theta,\phi)$ is simply the square of the field radiation pattern $G(f,\theta,\phi)$, while the function N can be expanded as

$$N(f,\theta,\phi|\hat{\mathbf{r}}_0) = T_b(f,\theta,\phi)P(f,\theta,\phi|\hat{\mathbf{r}}_0). \tag{6.4}$$

In equation (6.4) T_b is the brightness temperature distribution of the surrounding environment and $P(f,\theta,\phi|\hat{\mathbf{r}}_0)$ is the antenna power radiation pattern when the antenna is pointing in direction $\hat{\mathbf{r}}_0$. For the SKA, the model used for T_b is presented in [42]. It is a rotationally symmetric model with no variation in the ϕ-direction. This allows the direction the antenna is pointing towards to be described in terms of $\theta'(\theta_p,\theta,\phi)$ where θ_p is the tipping angle around which T_b is horizontally rotated. Due to the rotational symmetry, equation (6.4) can be separated into a sky brightness contribution and a ground brightness contribution, as given by

$$N(f,\theta,\phi|\hat{\mathbf{r}}_0) = \begin{cases} T_b^{sky}(f,\theta')P(f,\theta,\phi), & \theta' \in [0,\pi/2) \\ T_{b\parallel}(f,\theta')P_\parallel(f,\theta,\phi) + T_{b\perp}(f,\theta')P_\perp(f,\theta,\phi), & \theta' \in [\pi/2,\pi]. \end{cases} \tag{6.5}$$

where $0 \leq \theta' < \pi/2$ means the antenna is pointing towards the sky, and $\pi/2 \leq \theta' \leq \pi$ means the antenna is pointing towards the ground.

Sky Contribution

For the first part of equation (6.5), the brightness temperature originating from the sky can be calculated according to equation (6.6). As seen, it consists of various variables.

$$T_b^{\text{sky}}(f,\theta') = T_{bo}(f)e^{-\tau_{f,\theta'}(0,s_a)} + \int_0^{s_a} \frac{\kappa_a(f,z')T(z')e^{-\tau_{f,\theta'}(0,z')}}{\sqrt{1 - (\sin\theta'/(1 + (z'/r_e)))^2}}dz' \tag{6.6}$$

$T_{bo}(f)$ is the summation of the cosmic microwave background T_{CMB} and the directional averaged emission from the galaxy T_{go}. It is given as

$$T_{bo}(f) = T_{\text{CMB}} + T_{go}(f_0/f)^\beta \tag{6.7}$$

where the values $T_{\text{CMB}} = 2.73$ K, $T_{go} = 20$ K, $f_0 = 408$ MHz and $\beta = 2.75$ are suggested.

The opacity of the medium through which these emissions travel, compensated for a curved earth, is given as

$$\tau_{f,\theta'}(0, z) = \frac{1}{\sqrt{1 - (\sin\theta'/(1 + (s_a/r_e)))^2}} \int_0^z \kappa_a(f, \zeta)d\zeta \tag{6.8}$$

where earth radius $r_e = 6370.95$ km, atmosphere height $s_a = 100$ km and variable z refers to altitude. Note that the subscript $_{\theta'}$ specifies that the included integral should be solved over the path length through the atmosphere when tipped at the angle θ'.

Equation (6.8) also includes the effects of absorption by water vapour, $\kappa_{\text{H}_2\text{O}}(f, z)$, and oxygen, $\kappa_{\text{O}_2}(f, z)$, as a function of frequency and altitude as

$$\kappa_a(f, z) = \kappa_{\text{H}_2\text{O}}(f, z) + \kappa_{\text{O}_2}(f, z). \tag{6.9}$$

Any convenient standard atmosphere model may be used to calculate the pressure in (6.9). It may also be used to calculate the atmospheric temperature profile $T(z)$ in (6.6).

Ground Contribution

For the second part of equation (6.5), the brightness temperature caused due to the ground is polarization dependent. The subscripts $_\parallel$ and $_\perp$ are used to indicate the parallel and perpendicular polarizations, respectively. Calculation of $P_\parallel$ and $P_\perp$ is explained in detail in [42]. The polarized surrounding brightness temperature, meanwhile, is given as

$$\begin{aligned}
T_{b\parallel}(f, \theta') &= T_\parallel^{\text{sky}} + T_\parallel^{\text{gnd}} \\
&= \Gamma_\parallel(\theta_1)T_b^{\text{sky}}(f, \theta_1) + [1 - \Gamma_\parallel(\theta_1)]T_{\text{gnd}} \\
T_{b\perp}(f, \theta') &= T_\perp^{\text{sky}} + T_\perp^{\text{gnd}} \\
&= \Gamma_\perp(\theta_1)T_b^{\text{sky}}(f, \theta_1) + [1 - \Gamma_\perp(\theta_1)]T_{\text{gnd}}
\end{aligned} \tag{6.10}$$

where $\theta_1 = \pi - \theta'$ and ground temperature, T_{gnd}, is assumed to be 300 K. Lastly, the reflection coefficients for the two polarizations are given by

$$\begin{aligned}
\Gamma_\parallel(\theta_1) &= \left| \frac{\cos\theta_1 - \sqrt{\epsilon_2 - \sin^2\theta_1}}{\cos\theta_1 + \sqrt{\epsilon_2 - \sin^2\theta_1}} \right|^2 \\
\Gamma_\perp(\theta_1) &= \left| \frac{\epsilon_2\cos\theta_1 - \sqrt{\epsilon_2 - \sin^2\theta_1}}{\epsilon_2\cos\theta_1 + \sqrt{\epsilon_2 - \sin^2\theta_1}} \right|^2
\end{aligned} \tag{6.11}$$

with ϵ_2 approximately 3.5 for dry land.

For a more rapid calculation of the antenna noise temperature, it is assumed that the sources are unpolarized and the antenna has a high gain. Then, an averaged polarization reflection coefficient can be defined as

$$\overline{\Gamma}(\theta_1) = \frac{\Gamma_\parallel(\theta_1) + \Gamma_\perp(\theta_1)}{2}. \tag{6.12}$$

This simplifies (6.5) to

$$
N(f,\theta,\phi|\hat{\mathbf{r}}_0) = \begin{cases} T_b^{\mathrm{sky}}(f,\theta')P(f,\theta,\phi), & \theta' \in [0,\pi/2] \\ \left[\left(1 - \overline{\Gamma}(\theta_1)\right)T_{\mathrm{gnd}} + \overline{\Gamma}(\theta_1)T_b^{\mathrm{sky}}(f,\theta')\right]P(f,\theta,\phi), & \theta' \in [\pi/2,\pi] \end{cases} \quad (6.13)
$$

which is used to solve the the antenna noise temperature in (6.3) which, in turn, is used alongside the effective aperture area to calculate the sensitivity in (6.1). Using this simplification leads to a less than $\pm 5\,\%$ averaged error from the full calculation for T_A over the tipping angle $-85° \leq \theta_p \leq 85°$. In-house code was used to perform the calculations.

6.2   Parameter Study

In order to conduct a parameter study, the default model of the pyramidal sinuous antenna introduced in Chapter 4 was used. For convenience, it is shown again here in Fig. 6.1. Though this model does not contain a dielectric substrate, it is intended to be simulated at low frequencies which would not experience the problem the ultra wideband model encountered.
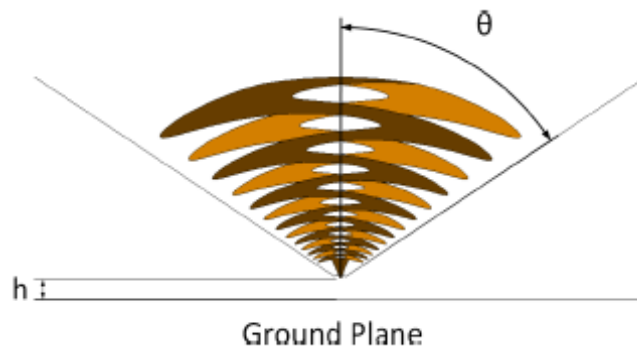
Figure 6.1: Pyramidal sinuous antenna model used for parameter study

The accompanying parameter space for the antenna's geometry is given in Table 6.1. Instead of varying the rotation angle δ and angular width α independently, they were varied as factor δ/α and sum $\delta + \alpha$. This allows for easier maximum and minimum search limits in the parameter space.

Table 6.1: Parameter space of reflector feed

Parameter	Number of points
$0.75 \leq \tau \leq 0.9$	31
$0.4° \leq \delta/\alpha \leq 0.8°$	41
$28° \leq \delta + \alpha \leq 44°$	17
$47° \leq \theta \leq 59°$	13
$h = 5$ mm	1
$f_{min} = 350$ MHz	N/A
$f_{max} = 1050$ MHz	N/A

All the points in the parameter space were solved using the university's High Performance Cluster (HPC) [43]. When the simulations completed, the necessary data was extracted and the relevant calculations to determine the performance were made. As previously stated, the differential reflection coefficient and the sensitivity were the chosen metrics.

Each model's performance, however, was characterised over frequency. In order to compare their differential reflection coefficients with one another, the maximum value within the frequency band was chosen to represent a model's performance. In the case of comparing sensitivities, the mean value above 650 MHz was used. This is due to the noise in the atmosphere dominating the calculation at the lower end of the spectrum, which causes their values to be less impactful.

Before discussing the performance results, the graphs in Fig. 6.2 should be mentioned. In the figure the maximum differential reflection coefficient of models in the centre of the parameter space are shown; each graph only has one variable changing while the rest remain at fixed values. As can be observed, the graphs are not monotonic in nature. This critically implies that an optimal solution is indeed included in the parameter space.

(a) $\delta/\alpha = 0.6°$, $\delta + \alpha = 35°$ and $\theta = 53°$

(b) $\tau = 0.825$, $\delta + \alpha = 35°$ and $\theta = 53°$

(c) $\tau = 0.825$, $\delta/\alpha = 0.6°$ and $\theta = 53°$

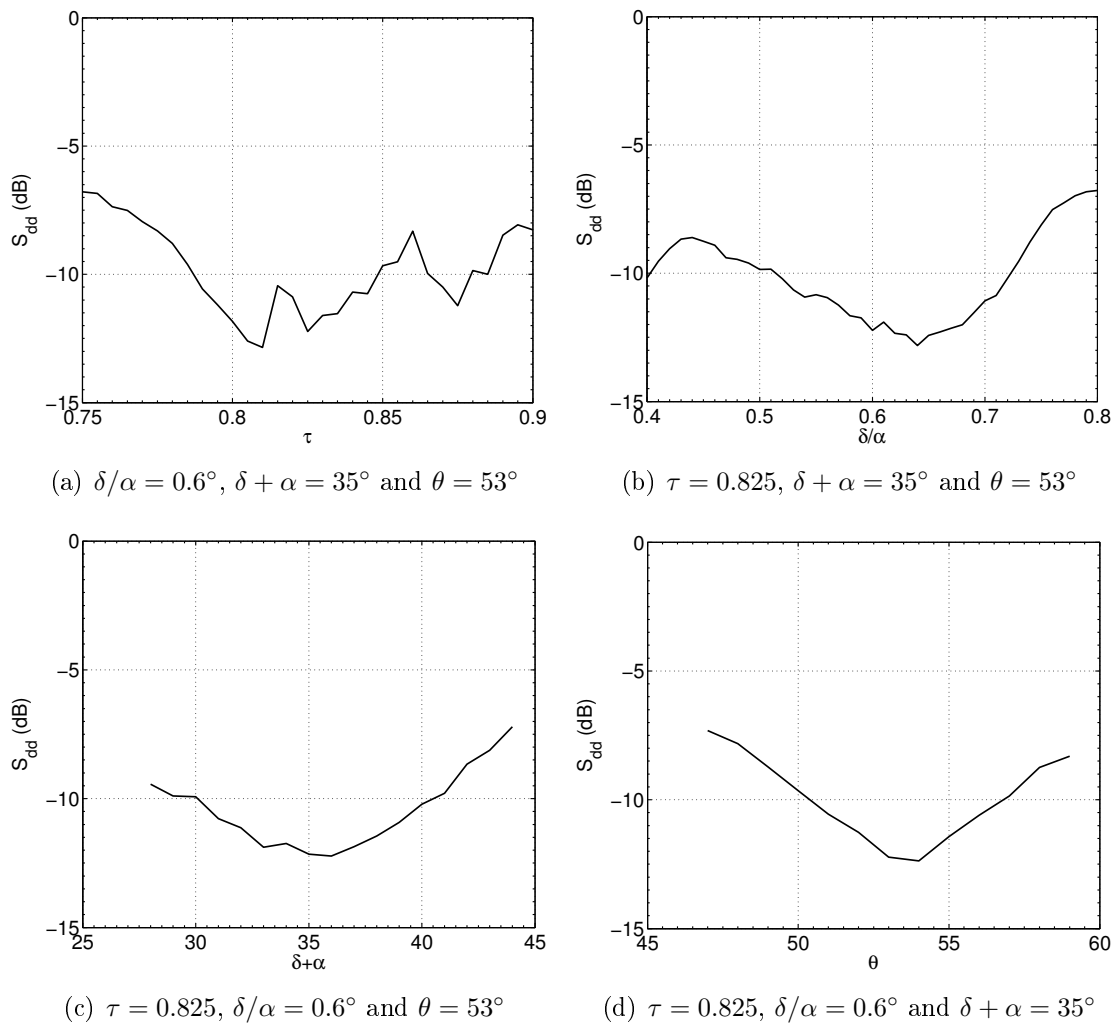(d) $\tau = 0.825$, $\delta/\alpha = 0.6°$ and $\delta + \alpha = 35°$

Figure 6.2: Variation over centre of the parameter space for the differential reflection coefficient

The three specific cases searched for in the parameter space include:

- Best differential reflection coefficient

- Best sensitivity

- Best sensitivity with best differential reflection coefficient less than -10 dB

While the first two items on the list showcases the best performance one can expect from the antenna for a single metric, the last one's design could potentially be used for the SKA. All the performance results are shown in Fig. 6.3 and discussed next. For interest's sake, the aperture efficiency for each case is also shown.

Best Differential Reflection Coefficient

The necessary geometry of the antenna to achieve the best differential reflection coefficient possible is given in Table 6.2. Black lines in Fig. 6.3 shows this antenna's performance. As can be seen in Fig. 6.3(a), the pyramidal sinuous antenna is capable of achieving a maximum differential reflection coefficient of -14 dB at 400 MHz. In Fig. 6.3(b) it can be the minimum aperture efficiency is 41 % just under 400 MHz. The corresponding sensitivity is shown in Fig. 6.3(c) with a mean value of 3.76 m^2/K above 650 MHz.

Table 6.2: Parameter values for best differential reflection coefficient

Parameter	Number of points
τ	0.825
δ/α	0.7°
$\delta + \alpha$	32°
θ	53°

Best Sensitivity

When looking for the best potential sensitivity of the antenna, the geometry given in Table 6.3 is applicable. Its performance can be seen as the red lines in Fig. 6.3. For a maximum differential reflection coefficient of -5 dB, a minimum aperture efficiency of 76 % is achievable. This relates to a mean sensitivity of 4.94 m^2/K above 650 MHz.

Table 6.3: Parameter values for best sensitivity

| Parameter	Number of points
τ	0.875
δ/α	0.55°
$\delta + \alpha$	44°
θ	59°

Table 6.4: Parameter values for best sensitivity with best differential reflection coefficient

Parameter	Number of points
τ	0.825
δ/α	0.65°
$\delta + \alpha$	36°
θ	57°

Best Sensitivity with Best Differential Reflection Coefficient

Lastly, if interested in an antenna with the best sensitivity possible while still maintaining a differential reflection coefficient less than -10 dB, the geometry given in Table 6.4 is required. The green lines in Fig. 6.3 indicate its performance. In this case the minimum aperture efficiency is 61 % while the mean sensitivity is 4.6 m^2/K above 650 MHz.

When looking at the performance results of the three cases, the trade-off between the sensitivity of the antenna and its differential reflection coefficient is clear to be seen. Searching for the best results for one metric does indeed come at the cost of the other one. Fortunately, good performance for both is also attainable in the chosen parameter space.
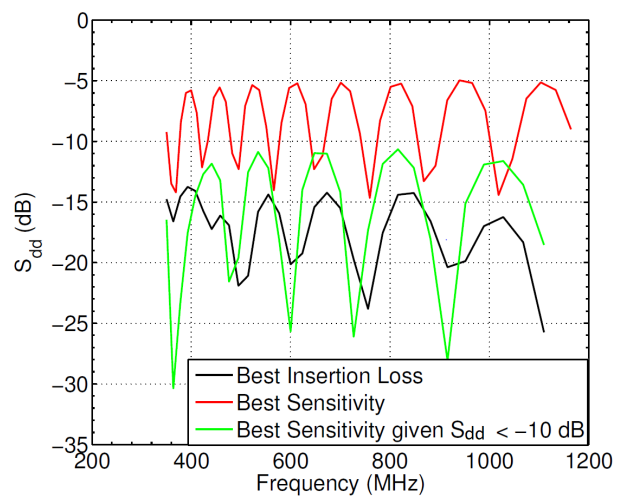
(a) Differential reflection coefficent
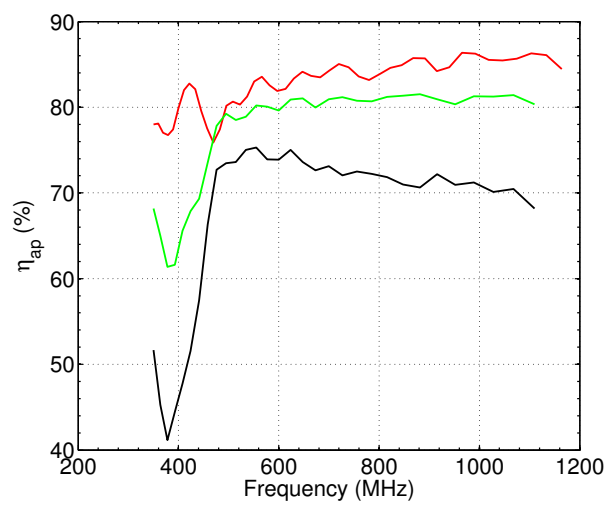
(b) Aperture efficiency with $\theta_0 = 48°$
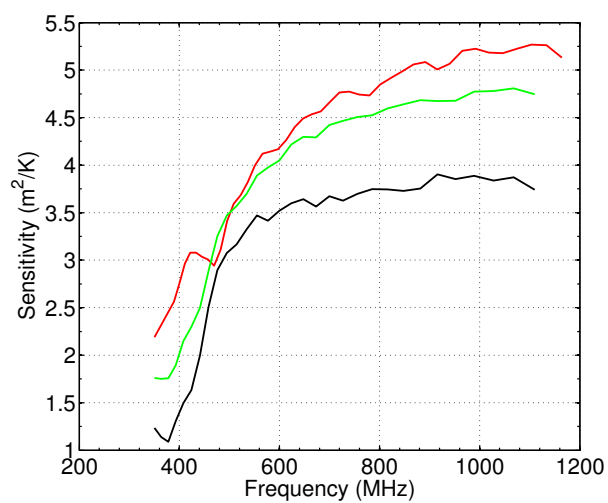
(c) Sensitivity

Figure 6.3: Performance of feed on an SKA reflector dish

Chapter 7

Conclusion

7.1   Summary of Results

A pyramidal sinuous antenna has been investigated. The details regarding its modelling process have been described – from the initial mesh considerations to the matching network applied. For the ultra wideband version a faster modelling process, at the expense of information in the centre of the bandwidth, was also explained.

   With its flat petals, the pyramidal sinuous antenna proved to be more reliable to manufacture than its conical counterpart and its curved petals. Though it is a feasible design, the construction process still leaves room for improvement. The measured results for the pyramidal $2-6$ GHz version's differential reflection coefficient mostly remained below -10 dB, while the conical version hovered around -5 dB. In terms of aperture efficiency, the manufactured pyramidal sinuous antenna was above 60 %.

   For the ultra wideband version, the feeding scheme caused significant degradation in the simulated performance. The measured results also did not comply with the degraded simulated results. As explained, this is likely due to not taking the dielectric substrate into account in the simulations. Despite this, the manufactured antenna's differential reflection coefficient mostly remained below -10 dB and its aperture efficiency above 52 % over a 5:1 bandwidth.

   A parameter study was also conducted on the antenna, with the intention of it serving as a feed for an SKA dish. Three specific cases were searched for in the parameter space. It was seen the pyramidal sinuous antenna's best capabilities are a maximum differential reflection coefficient of -14 dB or a mean sensitivity of 4.94 m^2/K. The best sensitivity obtainable while keeping the maximum differential reflection coefficient below -10 dB is 4.6 m^2/K.

7.2   Further Research Recommendations

In each of the different areas, there is room for further investigation. Regarding the faster modelling process, it is necessary to explain it in a more structured and thorough manner. Combining the method with an interpolation function to fill in the missing middle could potentially save on simulation time while still providing accurate results. In addition, the modelling process could potentially also be applied on other logarithmic antennas.

   Though only mentioned for the planar sinuous antenna, applying other feeding schemes for the pyramidal sinuous antenna could be hugely beneficial. If a suitable alternative can

67

be found, it could make the construction process of the antenna easier and / or improve the performance of the simulated ultra wideband version.

Regarding the ultra wideband version, how to improve the performance results and bring it in alignment to its measured results still has to be determined. A 10:1 bandwidth version still seems doable and worthwhile to investigate. How well it can perform should also be determined. The effect of dielectric substrates for the petals should be taken into account. Alongside this, applying a scaling factor on the active regions in order to counteract the effect of a fixed dielectric substrate thickness has to be investigated.

Bibliography

[1] P.E. Dewdney, W. Turner, R. Millenaar, R. McCool, J. Lazio and T. J. Cornwell: SKA1 System Baseline Design. March 2013.
Available at: http://www.skatelescope.org

[2] J. L. Jonas: MeerKAT. In: *General Assembly and Scientific Symposium (URSI GASS), 2014 XXXIth URSI*, pp. 1–1. Aug 2014.

[3] G. Cortes-Medellin: Novel non planar ultra wide band quasi self-complementary antenna. In: *2007 IEEE Antennas and Propagation Society International Symposium*, pp. 5733–5736. June 2007. ISSN 1522-3965.

[4] G. Engargiola: Non-planar log-periodic antenna feed for integration with a cryogenic microwave amplifier. In: *Antennas and Propagation Society International Symposium, 2002. IEEE*, vol. 4, pp. 140–143 vol.4. 2002.

[5] A.H. Akgiray: *New technologies driving decade-bandwidth radio astronomy : quad-ridged flared horn and compound-semiconductor LNAs*. Ph.D. thesis, California Institute of Technology, 2013.

[6] R. Olsson, P. S. Kildal and S. Weinreb: The eleven antenna: a compact low-profile decade bandwidth dual polarized feed for reflector antennas. *IEEE Transactions on Antennas and Propagation*, vol. 54, no. 2, pp. 368–375, Feb 2006. ISSN 0018-926X.

[7] R. Gawande and R. Bradley: Towards an ultra wideband low noise active sinuous feed for next generation radio telescopes. *IEEE Transactions on Antennas and Propagation*, vol. 59, no. 6, pp. 1945–1953, June 2011. ISSN 0018-926X.

[8] G. Cortes-Medellin: Non-Planar Quasi-Self-Complementary Ultra-Wideband Feed Antenna. *IEEE Transactions on Antennas and Propagation*, vol. 59, no. 6, pp. 1935–1944, June 2011. ISSN 0018-926X.

[9] J. Yang, M. Pantaleev, P. S. Kildal, B. Klein, Y. Karandikar, L. Helldner, N. Wadefalk and C. Beaudoin: Cryogenic 2-13 GHz Eleven Feed for Reflector Antennas in Future Wideband Radio Telescopes. *IEEE Transactions on Antennas and Propagation*, vol. 59, no. 6, pp. 1918–1934, June 2011. ISSN 0018-926X.

[10] R.S. Gawande: *Ambient and Cryogenic, Decade Bandwidth, Low Noise Receiving System for Radio Astronomy Using Sinuous Antenna*. PhD, University of Virginia, 2011.

[11] N. Mutonkole: *Study of a Wideband Sinuous Feed for Reflector Antenna Applications*. Master's Thesis, University of Stellenbosch, Stellenbosch, South Africa, December 2013.

[12] C.A. Balanis: *Antenna Theory: Analysis and Design*. 3rd edn. John Wiley & Sons, Inc., New Jersey, 2005.

[13] P. Hannan: Microwave antennas derived from the cassegrain telescope. *IRE Transactions on Antennas and Propagation*, vol. 9, no. 2, pp. 140–153, March 1961. ISSN 0096-1973.

[14] Y. Mizugutch, M. Akagawa and H. Yokoi: Offset dual reflector antenna. In: *1976 Antennas and Propagation Society International Symposium*, vol. 14, pp. 2–5. Oct 1976.

[15] C. Granet: Designing classical offset Cassegrain or Gregorian dual-reflector antennas from combinations of prescribed geometric parameters. *IEEE Antennas and Propagation Magazine*, vol. 44, no. 3, pp. 114–123, Jun 2002. ISSN 1045-9243.

[16] W.V.T. Rusch, A. Prata, Y. Rahmat-Samii and R. A. Shore: Derivation and application of the equivalent paraboloid for classical offset Cassegrain and Gregorian antennas. *IEEE Transactions on Antennas and Propagation*, vol. 38, no. 8, pp. 1141–1149, Aug 1990. ISSN 0018-926X.

[17] R. Lehmensiek, I.P. Theron and D. I. L. De Villiers: Deriving an Optimum Mapping Function for the SKA-Shaped Offset Gregorian Reflectors. *IEEE Transactions on Antennas and Propagation*, vol. 63, no. 11, pp. 4658–4666, Nov 2015. ISSN 0018-926X.

[18] P. S. Kildal: Factorization of the feed efficiency of paraboloids and Cassegrain antennas. *IEEE Transactions on Antennas and Propagation*, vol. 33, no. 8, pp. 903–908, Aug 1985. ISSN 0018-926X.

[19] P. S. Kildal and Z. Sipus: Classification of Rotationally Symmetric Antennas as Types BOR0 and BOR1. *IEEE Antennas and Propagation Magazine*, vol. 37, no. 6, pp. 114–, Dec 1995. ISSN 1045-9243.

[20] P. S. Kildal: *Foundations of Antenna Engineering: A Unified Approach for Line-of-Sight and Multipath*. Kildal Antenn AB, 2015.

[21] J. Yang, S. Pivnenko and P. S. Kildal: Comparison of two decade-bandwidth feeds for reflector antennas: The Eleven Antenna and quadridge horn. In: *Proceedings of the Fourth European Conference on Antennas and Propagation*, pp. 1–5. April 2010. ISSN 2164-3342.

[22] A. C. Ludwig: The definition of cross polarization. *IEEE Transactions on Antennas and Propagation*, vol. 21, no. 1, pp. 116–119, Jan 1973. ISSN 0018-926X.

[23] D. I. L. de Villiers: Offset Dual-Reflector Antenna System Efficiency Predictions Including Subreflector Diffraction. *IEEE Antennas and Wireless Propagation Letters*, vol. 10, pp. 947–950, 2011. ISSN 1536-1225.

[24] R. H. DuHamel: *Dual Polarized Sinuous Antenna*. 4658262. US Patent Office, 1987.

[25] J. H. Cloete and T. Sickel: The planar dual-polarized cavity backed sinuous antenna - a design summary. In: *Antennas and Propagation in Wireless Communications (APWC), 2012 IEEE-APS Topical Conference on*, pp. 1169–1172. Sept 2012.

[26] G. Deschamps: Impedance properties of complementary multiterminal planar structures. *IRE Transactions on Antennas and Propagation*, vol. 7, no. 5, pp. 371–378, December 1959. ISSN 0096-1973.

[27] A. Jafargholi and M. Kamyab: A new approach for feeding sinuous antenna. *{AEU} - International Journal of Electronics and Communications*, vol. 65, no. 4, pp. 312 – 319, 2011. ISSN 1434-8411.

[28] P.H. Gonnet, A. Sharaiha, C. Terret and A. Skrivervik: Feeding networks for sinuous antennas. *Microwave and Optical Technology Letters*, vol. 20, no. 3, pp. 195–200, 1999. ISSN 1098-2760.

[29] R.A. Chipman: *Theory and Problems of Transmission Lines.* McGraw-Hill Book Company, 1968.

[30] W. Fan, A. Lu, L. L. Wai and B. K. Lok: Mixed-mode S-parameter characterization of differential structures. In: *Electronics Packaging Technology, 2003 5th Conference (EPTC 2003)*, pp. 533–537. Dec 2003.

[31] D. E. Bockelman and W. R. Eisenstadt: Combined differential and common-mode scattering parameters: theory and simulation. *IEEE Transactions on Microwave Theory and Techniques*, vol. 43, no. 7, pp. 1530–1539, Jul 1995. ISSN 0018-9480.

[32] HyperWorks FEKO 14.0.
Available at: `http://www.altairhyperworks.com/product/FEKO`

[33] D.M. Pozar: *Microwave Engineering.* 3rd edn. Wiley, 2004. ISBN 9780471448785.

[34] AWR Microwave Office.
Available at: `http://www.awrcorp.com/products/ni-awr-design-environment/microwave-office`

[35] NSI: Broadband Ridged Guide Probe. .
Available at: `http://ww2.nearfield.com/sales/datasheets/NSI-RF-RGP-10.htm`

[36] NSI: Open ended waveguide probe. .
Available at: `http://ww2.nearfield.com/Sales/datasheets/pdfs/OEWG_Probes.pdf`

[37] D. S. Prinsloo, P. Meyer, R. Maaskant and M. Ivashina: Design of an active dual-mode antenna with near hemispherical Field of View coverage. In: *Electromagnetics in Advanced Applications (ICEAA), 2013 International Conference on*, pp. 1064–1067. Sept 2013.

[38] S. B. Cohn: Optimum Design of Stepped Transmission-Line Transformers. *IRE Transactions on Microwave Theory and Techniques*, vol. 3, no. 3, pp. 16–20, April 1955. ISSN 0097-2002.

[39] J. Yin and J. Yang and M. Panteleev and L. Helldner: A circular Eleven feed with significantly improved aperture efficiency over 1.3 - 14 GHz. In: *2012 6th European Conference on Antennas and Propagation (EUCAP)*, pp. 2353–2356. March 2012. ISSN 2164-3342.

[40] D.M. Pozar: *Microwave and RF Design of Wireless Systems.* John Wiley & Sons, Inc., 2001.

[41] D. I. L. De Villiers and R. Lehmensiek: Rapid Calculation of Antenna Noise Temperature in Offset Gregorian Reflector Systems. *IEEE Transactions on Antennas and Propagation*, vol. 63, no. 4, pp. 1564–1571, April 2015. ISSN 0018-926X.

[42] G. C. Medellin: Antenna noise temperature calculations. In: *SKA Memo 95.* 2007.

[43] University of Stellenbosch: HPC1 (Rhasatsha).
Available at: `http://www.sun.ac.za/hpc`